

COMBINED EFFECT OF STRONTIUM CONTENT AND ELECTRODE TYPE ON ELECTRICAL PROPERTIES OF  $\text{Ba}_x\text{Sr}_{1-x}\text{TiO}_3$  THIN-FILMS

by

OMID MOHAMMAD MORADI

Submitted to the Graduate School of Engineering and Natural Sciences

in partial fulfillment of the requirements for the degree of

Master of Science

Sabanci University

January 2017

COMBINED EFFECT OF STRONTIUM CONTENT AND ELECTRODE TYPE ON ELECTRICAL  
PROPERTIES OF  $Ba_xSr_{1-x}TiO_3$  THIN-FILMS

APPROVED BY:

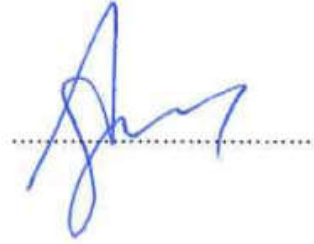
Assoc. Prof. Dr. İ. Burç MISIRLIOĞLU  
(Thesis Supervisor)



Asst. Prof. Dr. Fevzi Çakmak CEBECİ



Asst. Prof. Dr. Ali Fuat ERGENÇ



DATE OF APPROVAL: 06.01.2017

© Omid Mohammad Moradi 2017

All Rights Reserved

# COMBINED EFFECT OF STRONTIUM CONTENT AND ELECTRODE TYPE ON ELECTRICAL PROPERTIES OF $\text{Ba}_x\text{Sr}_{1-x}\text{TiO}_3$ THIN-FILMS

Omid MOHAMMAD MORADI

Materials Science and Nano Engineering, Master of Science, 2017

Thesis Supervisor: Assoc. Prof. Dr. İ. Burç MISIRLIOĞLU

Keywords: Ferroelectric, barium strontium titanate, sol-gel method, resistive switching

## ABSTRACT

Ferroelectric thin films have been on agenda of many research groups and the semiconductor industry for applications ranging from non-volatile data storage to tunable capacitors and antennas. In much of these works, the fact that ferroelectrics can be sensitive to the electrical boundary conditions, namely the type of the electrodes employed, is often taken for granted without an in-depth analysis. In this thesis work, we focus on  $\text{Ba}_x\text{Sr}_{1-x}\text{TiO}_3$  compositions, a well-known system, grown via a sol-gel method on conducting Nb:SrTiO<sub>3</sub> bottom electrodes to explore the effect of the Sr content and the top/bottom electrode asymmetry on the electrical characteristics of these systems. Following structural and morphological characterization for quality check of the films, we extensively focus on a process called “resistive switching”, which we repeatedly observed in our samples. Resistive switching phenomena is a topic of interest as the direction of the ferroelectric polarization determines whether there will be carrier depletion or accumulation in the semiconducting electrode (the conducting oxide bottom electrode in this thesis), upon which various novel device and transistor designs have been recently proposed by a number of groups. In this work, we focus on the experimental evidence for resistive switching in the light of thermodynamic theory of these systems and discuss the effect of Sr content on current-voltage characteristics of our samples.

# STRANSİYUM İÇERİĞİ VE ELEKTROD TİPİNİN $Ba_xSr_{1-x}TiO_3$ İNCE FİLMLEİN ELEKTRİKSEL ÖZELLİKLERİ ÜZERİNE TÜMLEŞİK ETKİSİ

Omid MOHAMMAD MORADI

Malzeme Bilimi ve Nano Mühendislik, Yüksek Lisans Tezi, 2017

Tez Danışmanı: Yard. Doç. Dr. İ. Burç MISIRLIOĞLU

Anahtar kelimeler: Ferroelektrik, baryum stransiyum titanat, sol-jel yöntemi, dirençli anahtarlama.

## ÖZET

Ferroelektrik ince filmler, uçucu olmayan veri depolamadan ayarlanabilir kapasitörler ve antenlere kadar birçok araştırma grubunun ve yarı iletken endüstrisinin gündemindedir. Bu çalışmaların çoğunda, ferroelektriklerin elektrik sınır koşullarına, yani kullanılan elektrodların türüne hassas olabileceği, sıklıkla derinlemesine bir analiz yapılmadan ele alınır. Bu tez çalışmasında, Sr içeriğinin ve üst / alt elektrot asimetrisinin elektriksel karakteristikler üzerindeki etkisini araştırmak için Nb:SrTiO<sub>3</sub>iletken alt elektrotları üzerinde bir sol-jel yöntemi ile geliştirilmiş iyi bilinen bir sistem olan  $Ba_xSr_{1-x}TiO_3$  bileşimlerine odaklanıyoruz. Filmlerin kalite kontrolü için yapısal ve morfolojik karakterizasyonlarını takiben, "dirençli anahtarlama" adı verilen ve örneklerimizde tekrar tekrar gözlemlediğimiz bir sürece yoğunlaşıyoruz. Dirençli anahtarlama olgusu, ferroelektrik kutuplaşma yönünün yarıiletken elektrotta (bu tezdeki iletken oksit alt elektrotunda) taşıyıcıazalmasına veya birikmesine neden olup olmadığını belirlediği için ilgi çekici bir konudur ve bu konuda birçok grup tarafından çeşitli yeni cihaz ve transistör tasarımları önerilmiştir. Bu çalışmada, bu sistemlerin termodinamik teorileri ışığında dirençli geçiş için deneysel kanıta odaklanıyoruz ve örneklerin akım-voltaj karakteristikleri üzerindeki Sr içeriğinin etkisini tartışıyoruz.

## ACKNOWLEDGEMENTS

I would like to express my sincere gratitude to my advisor Assoc. Prof. Dr. İ. Burç MISIRLIOĞLU for his continuous support of my MSc study and related research, for his patience, motivation, and immense knowledge. His guidance helped me in all the time of research and writing of this thesis.

Besides my advisor, I would like to thank my colleague and friend Mr. Canhan ŞEN. I learned so many useful things from him and he supported me as a true friend. Without him I definitely would have difficult times progressing in my studies.

I have to deliver my regards to our lab specialist Mr. Turgay GÖNÜL whose advices and kind supervision have always been with us in characterization labs. Without him we wouldn't be able to gain experience in characterization instruments in Sabanci University.

Ms. Sibel PÜRÇÜKLÜ is the most supportive and kind person I could meet in our university. She helped us more than anyone in spite of obstacles. I sincerely appreciate her support.

A special thanks to Prof. Dr. Lucian PINTILIE, director of the National Institute of Materials Physics, Magurele-Romania who granted his support and spared some precious time of his laboratory to our research. Also, I am grateful to the administration and lab specialists of this institute to help us use their equipment.

I have to thank Assoc. Prof. Dr. Cleva OW-YANG and Prof. Dr. Mehmet Ali GÜLGÜN who kindly let me borrow their instruments and use to get result for this thesis.

I also thank to Prof. Dr. Ayhan BOZKURT whose consult on completing the electrical measurements setup in Sabanci University was beneficial.

Thanks to Dr. Tuğçe AKKAŞ for proof-reading my thesis. She is an expert in this field and her dedication improved my thesis draft quality.

Thanks to all my friends in MAT grads and BIO grads. Believe me, life without them would be gloomy in Sabanci University.

I would like to thank my thesis jury committee members, Assist. Prof. Dr. Fevzi Çakmak CEBECI and Prof. Dr. Ali Fuat ERGENÇ for their time and guidance to review my thesis and comment which would help me on a better draft of my thesis.

This thesis is supported by a TUBITAK COST project fund (113M972) and I acknowledge the funding for supporting me during my studies.

Last but not least, I have to thank my father and my mother whose are my heroes in life.

## TABLE OF CONTENTS

|  |      |
|--|------|
| ABSTRACT .....   | iii  |
| ÖZET .....   | iv   |
| ACKNOWLEDGEMENTS.....  | v    |
| TABLE OF CONTENTS .....  | vi   |
| LIST OF FIGURES .....  | viii |
| LIST OF TABLES .....   | xi   |
| LIST OF SYMBOLS AND ABBREVIATIONS.....   | xii  |
| Chapter 1: INTRODUCTION .....  | 1    |
| 1.1 Definitions and Properties.....  | 3    |
| 1.2 Structure of Barium Titanate.....  | 5    |
| 1.3 Structure of Barium Strontium Titanate.....                                    | 7    |
| 1.4 Electrical Properties.....   | 11   |
| 1.4.1 Polarization-Electric Field (P-E) Loops.....                                 | 11   |
| 1.4.2 A Simple Metal-Semiconductor Interface.....                                  | 14   |
| 1.4.3 A model for Metal-Ferroelectric-Metal Interface .....                        | 19   |
| 1.4.4 Theory and Methodology for Computational Study .....                         | 21   |
| 1.4.5 Capacitance-Voltage Characteristics.....                                     | 28   |
| 1.4.6 Resistive Switching .....  | 29   |
| Chapter 2: SAMPLE FABRICATION METHOD AND PROCEDURE.....                            | 36   |
| 2.1 Solution Preparation Method .....  | 36   |
| 2.1.1 Barium Strontium Titanate ( $Ba_xSr_{1-x}TiO_3$ ) Solution Preparation ..... | 36   |
| 2.1.2 Thin-film Deposition Method .....  | 38   |
| 2.1.3 Thermal Treatment of Thin-films .....  | 40   |

|   |    |
|---|----|
| Chapter 3: RESULTS AND DISCUSSION .....                         | 41 |
| 3.1 Structural Characterization .....                           | 41 |
| 3.1.1 X-ray Diffraction Results (XRD) .....                     | 41 |
| 3.1.2 Scanning Electron Microscopy (SEM) Results.....           | 43 |
| 3.2 Electrical characterizations .....                          | 48 |
| 3.2.1 Current-Voltage (I-V) Characteristics .....               | 51 |
| 3.2.2 Capacitance – Voltage characteristics .....               | 55 |
| 3.2.3 Polarization – Electric field (P-E) Hysteresis Loop ..... | 57 |
| 3.2.4 Computational Modeling Results .....                      | 60 |
| 3.2.5 Resistive Switching .....                                 | 64 |
| Chapter 4: CONCLUSION .....                                     | 69 |
| REFERENCES .....  | 71 |

## LIST OF FIGURES

|  |    |
|--|----|
| Figure 1-1: Cross section of a ferroelectric memory designed by Texas Instruments (TI).....  | 2  |
| Figure 1-2: Energy state of lattice cell due to displacement of Ti atom in BaTiO <sub>3</sub> structure [19]. .....  | 3  |
| Figure 1-3: An illustration of ferroelectric domains in a crystal cross section.....   | 4  |
| Figure 1-4: Change with temperature of the dielectric permittivity of a BaTiO <sub>3</sub> single crystal. The schematics of Ti displacement in the oxygen octahedron of the perovskite structure are also shown [25].....   | 5  |
| Figure 1-5: Distortion in BaTiO <sub>3</sub> upon cooling from cubic phase. ....   | 6  |
| Figure 1-6: Ferroelectric transition temperature as a function of Ba/Sr ratio in bulk BST [34].....  | 8  |
| Figure 1-7: Crystal structure of BST composition as a function of Ba/Sr ratio [34].....  | 9  |
| Figure 1-8: Temperature dependence of dielectric constant for BST ceramics with different Ba/Sr ratio [34].....  | 10 |
| Figure 1-9: Schematic charge voltage response (in arbitrary units) of a) linear capacitor, b) resistor, c) lossy capacitor and d) ferroelectric[38]. .....   | 12 |
| Figure 1-10: A perfect hysteretic behavior of the ferroelectric polarization in an applied external electric field [35]. ....  | 12 |
| Figure 1-11: An illustration of metal-dielectric interface in an MDM configuration.....  | 13 |
| Figure 1-12: Band bending before and after metal-semiconductor contact. a) High work-function metal and n-type semiconductor, b) low work-function metal and n-type semiconductor, c) high work-function metal and p-type semiconductor, and d) low work-function metal and p-type semiconductor [45]. .....   | 15 |
| Figure 1-13: (a) Charge density, (b) electric field, (c) potential and (d) energy as obtained with the full depletion analysis. ....   | 17 |
| Figure 1-14: Schematic of the band diagram for a metal-ferroelectric-metal structure [46]. ....  | 20 |
| Figure 1-15: An illustration of considered profile for computational study. ....   | 21 |
| Figure 1-16: C–V characteristics at 1 kHz measured after poling the film with 6 V for one minute [59]. ....  | 28 |
| Figure 1-17: I–V curves for (a) unipolar (nonpolar) switching in a Pt–NiO–Pt cell and (b) bipolar switching in a Ti–La <sub>2</sub> CuO <sub>4</sub> –La <sub>1.65</sub> Sr <sub>0.35</sub> CuO <sub>4</sub> cell. Proposed models for resistive switching which classified according to either (c) a filamentary conducting path, or (d) an interface-type conducting path [68]. .... | 30 |
| Figure 1-18: The polarization-induced variation of the tunnel barrier height in FTJs and the potential profile across the metal 1 (M1)/ferroelectric(FE)/metal 2 (M2) heterostructure for two orientations (right and left) of the ferroelectric polarization (P) [74]. ....   | 31 |
| Figure 1-19: Simultaneous measurements of current and piezoelectric response of a MFM cell with a 6 nm thick PZT film [81]. ....   | 32 |
| Figure 1-20: (a) Schematic of the device. (b) I–V characteristics for all samples. The blue and orange lines fit to equation (1) for the, respectively, in each case. (c) Extracted barrier heights $\phi_B$ and ideality factors $n$ . (d) Forward bias I–V for samples A and D. reprinted from [82]. ....  | 34 |
| Figure 1-21: An illustration of low resistive state (LRS) and high resistive state (HRS) depending on the polarization direction.....  | 35 |

|  |    |
|--|----|
| Figure 2-1: Four stages of spin coating process. ....  | 38 |
| Figure 2-2: Flow chart of solution preparation, deposition thin films and post heat treatment steps.....   | 40 |
| Figure 3-1: XRD pattern of BT thin-film on Nb(0.07%):STO(100) compared to Barium Titanate tetragonal structure. (JCPDS:081-2203)<br>.....  | 41 |
| Figure 3-2: XRD spectrum of a) $\text{BaTiO}_3$ b) $\text{Ba}_{0.5}\text{Sr}_{0.5}\text{TiO}_3$ c) $\text{Ba}_{0.7}\text{Sr}_{0.3}\text{TiO}_3$ films grown on Nb(0.07%):STO (100) substrate. ....               | 42 |
| Figure 3-3: SEM image of thin-film deposited from 1M solution in different magnification a) 10kX b) 30kX.....  | 43 |
| Figure 3-4: SEM results show a) surface morphology of thin film b) vertical cross section of the film.....   | 44 |
| Figure 3-5: Thickness of a dense thin film in a) 50kX magnification, b) 150kX magnification after optimizing the spin coat parameters, heating rate, sintering temperature and atmosphere.....                   | 44 |
| Figure 3-6:a) deposited Au electrodes on BT b) Surface morphology of Au Electrode on BTO c) Schematic illustration of the Au Electrode and film structure in presence of the a very thin Cr adhesive layer ..... | 45 |
| Figure 3-7: Surface of $\text{BaTiO}_3$ film in two magnifications. a)10kX b)50kX.....   | 46 |
| Figure 3-8: Surface of $\text{Ba}_{0.7}\text{Sr}_{0.3}\text{TiO}_3$ film in two magnifications. a)10kX b)50kX. ....  | 46 |
| Figure 3-9: Surface of $\text{Ba}_{0.5}\text{Sr}_{0.5}\text{TiO}_3$ film in two magnifications. a)10Kx b)50Kx. ....  | 47 |
| Figure 3-10: Platinum Electrode surface quality a) Diameter of each electrode is $100\mu\text{m}$ b) SE2 and Inlens images of the electrode surface. ....  | 47 |
| Figure 3-11:Electrical measurement setup in Sabanci University.....  | 48 |
| Figure 3-12: Electrical measurement setup in NIMP. Magurele-Romania. ....  | 49 |
| Figure 3-13: Two different configurations for probes to measure the I-V and C-V characteristics. ....  | 50 |
| Figure 3-14: Samples assembled on the standard stage in form of configuration 1. ....  | 50 |
| Figure 3-15: I-V measurements data of BT with a) Pt as the top electrode and b)Cu as the top electrode compared in configurations 1 and 2. ....  | 52 |
| Figure 3-16: I-V measurements data of BST70 with a) Pt as the top electrode and b) Cu as the top electrode compared in configurations 1 and 2. ....  | 52 |
| Figure 3-17: I-V measurements data of BST50 with a) Ptas the top electrode and b) Cu as the top electrode compared in configurations 1 and 2. ....   | 53 |
| Figure 3-18: Measured I-V characteristics of all compositions in configuration 1 for both a)Pt as the top electrode b)Cu as the top electrode. ....  | 53 |
| Figure 3-19: Measured I-V characteristics of all compositions in configuration 2 for both a)Pt as the top electrode b)Cu as the top electrode. ....  | 54 |

|   |    |
|---|----|
| Figure 3-20: C-V measurement of the samples in room temperature (Configuration 2). Comparing the Cu and Pt electrode type on a) BaTiO <sub>3</sub> (BT) b) Ba <sub>0.7</sub> Sr <sub>0.3</sub> TiO <sub>3</sub> (BST70) c)Ba <sub>0.5</sub> Sr <sub>0.5</sub> TiO <sub>3</sub> (BST50).....   | 55 |
| Figure 3-21: C-V measurement of the samples in room temperature (Configuration 2). Comparing the effect of: a) Cu as the top electrode b) Pt as top the electrode on all compositions. c) Comparing all C-V measurements result. ....   | 56 |
| Figure 3-22: P-E hysteresis loop for Pt top electrode of a)BT b)BST70 c)BST50. ....   | 57 |
| Figure 3-23: Time dependent P-E hysteresis loop for Pt top electrode of a)BT b)BST70 c)BST50.....   | 57 |
| Figure 3-24: Hysteresis loops for SRO-PZT-Ta structures with 100 nm thickness of the PZT layer [94]. ....   | 58 |
| Figure 3-25: Remnant polarization indication in Pt deposited electrode on a) BT b) BST70 c)BST50. ....  | 59 |
| Figure 3-26: I-V curve corresponding to Pt-Ba <sub>x</sub> S <sub>1-x</sub> T-Nb:STO heterostructure indicating the direction of the polarization and resistive states.....   | 64 |
| Figure 3-27: Regular I-V curve corresponding to Pt-Ba <sub>x</sub> S <sub>1-x</sub> T-Nb:STO heterostructure measured in configuration 1. ....  | 65 |
| Figure 3-28: Schematic charge distribution and (c), (d) corresponding energy-band diagrams at LRS and HRS, respectively. In the BTO layer, the red arrows denote the polarization directions and the large 'plus' and 'minus' symbols represent positive and negative ferroelectric bound charges, respectively. The 'plus' and 'dot' symbols in the Pt and NSTO represent holes and electrons, respectively. The 'circled plus' symbols represent ionized donors [103]. .... | 66 |
| Figure 3-29: Result of the computational study in applying +1V bias to the top electrode BT a) Polarization along Z axis b)carriers (Electron) map c) Ionized donor distribution map d) energy band diagram in the midsection of the film along the thickness.....  | 67 |
| Figure 3-30: Result of the computational study in applying -1V bias to the top electrode a) Polarization along Z axis b)carriers (Electron) map c) Ionized donor distribution map d) energy band diagram in the midsection of the film along the thickness.. ....   | 67 |

## LIST OF TABLES

|   |    |
|---|----|
| Table 1: Material parameters and thermodynamic coefficients for BTO and STO used in the calculations [53],[54]..... | 25 |
| Table 2-1: Summarized list of different alkoxides in reported studies. ....   | 36 |
| Table 2-2: Starting substances and information. ....  | 37 |
| Table 2-3: Chemical substance mixing ratio. ....  | 37 |
| Table 4: Computational simulation results for BT in three different bias applied in top electrode.....              | 61 |
| Table 5: Computational simulation results for BST50 in three different bias applied in top electrode.....           | 62 |

## LIST OF SYMBOLS AND ABBREVIATIONS

|                |                               |
|----------------|-------------------------------|
| BCs            | Boundary Conditions           |
| BST            | Barium Strontium Titanate     |
| CAFM           | Conductive Atomic Microscopy  |
| C-V            | Capacitance-Voltage           |
| DRAM           | Dynamic RAMs                  |
| FE             | Ferroelectric                 |
| FeRAM          | Ferroelectric RAMs            |
| FTJ            | Ferroelectric Tunnel Junction |
| HRS            | High Resistive State          |
| I-V            | Current-Voltage               |
| LGD            | Landau-Ginzburg-Devonshire    |
| LRS            | Low Resistive State           |
| LSMO           | lanthanum strontium manganite |
| MDM            | Metal-Dielectric-Metal        |
| MFM            | Metal-Ferroelectric-Metal     |
| M-S            | Metal-Semiconductor           |
| P-E            | Polarization-Electric field   |
| PTO            | PbTiO <sub>3</sub>            |
| PZT            | Lead Zirconate Titanate       |
| RS             | Resistive Switching           |
| SBH            | Schottky Barrier Height       |
| T <sub>c</sub> | Transition Temperature        |

## Chapter 1: INTRODUCTION

Ferroelectrics are promising materials for a wide range of applications. These materials, unlike regular dielectrics, possess a remnant polarization in the absence of an external electric field in analogy with magnets where a remnant magnetization exists in the absence of an external magnetic field. Unlike magnetism, the ferroelectric polarization is due to asymmetric displacements of some of the ions in the unit cell when the material is cooled below a critical temperature. The polarization dependence of properties of ferroelectric materials have attracted much attention due to the possibility of application to various electronic devices such as memory cell capacitors [1]. As they present non-linear variation of dielectric constant with the electric field, high dielectric constant and moderate loss in microwave domain, ferroelectric materials present also a high potential for microwave applications [2], [3]. In microwaves, the ferroelectric materials exhibit lower dielectric loss in the paraelectric phase than in the ferroelectric phase. Therefore, most of the electrically controlled devices such as phase-shifters, tunable filters or ferroelectric varactors employ the ferroelectric materials in the paraelectric phase [4]. Barium Strontium Titanate ( $\text{Ba}_x\text{Sr}_{1-x}\text{TiO}_3$ ) ( $x=0, 0.5, 0.7$ ) is one of the most researched ferroelectric materials for tunable applications at high frequencies since it demonstrates a superior tradeoff between loss and tunability [5]–[7].

In information technology, ferroelectrics are sometimes used as active components in high-density random access memories ferroelectric RAMs (FeRAM) and Dynamic RAMs (DRAMs) memories [8], [9]. In FeRAM a ferroelectric layer is used instead of a typical dielectric to achieve non-volatility via the presence of the polarization. FeRAM has many advantages over flash memories include: low power consumption, fast write process, longer read/write cycle ( $10^{10}$ - $10^{14}$  cycles) and etc. In 2002 Texas instrument introduced a new design of FeRAM to commercialize the product (Figure 1-1). However, like all prototypes, FeRAM has its own disadvantages include: it has lower storage densities comparing flash devices, limitation of storage capacity, production cost is higher cost. Also, FeRAM suffer an unusual technical disadvantage of a destructive read process, which requires a write-after-read architecture. Hence, the FeRAM improvement requires more investigations to modify the key characteristics of the ferroelectrics materials.

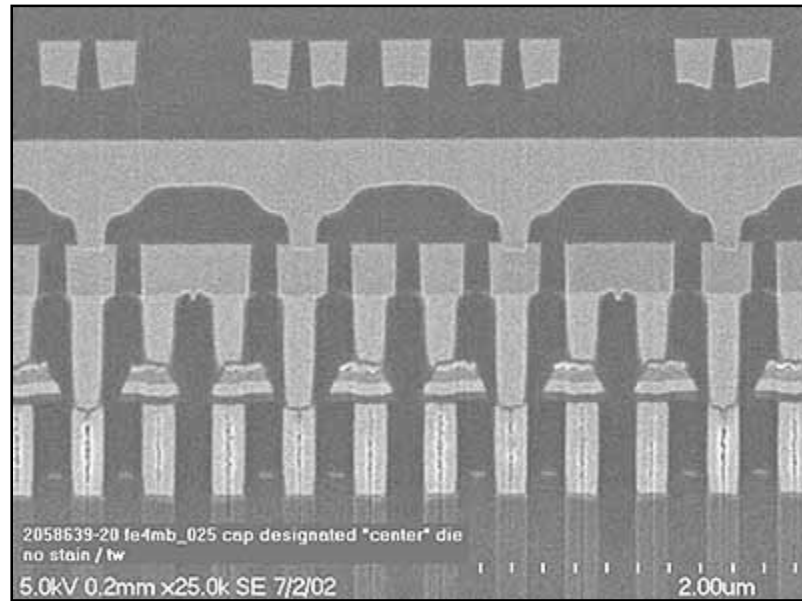


Figure 1-1: Cross section of a ferroelectric memory designed by Texas Instruments (TI).

Vast amount of the studies aimed to investigate the tunability of Barium Strontium Titanate structure via addition of Strontium. Even commercial powder in high purity is available in fair price which can be used as reliable precursor in a scientific investigation [10]–[14]. In the previous studies, the whole structural modification, dielectric change and electrical characteristics of such films regarding to the application needs are investigated thoroughly [2], [4]–[8]. The dielectric properties of BST films have often been interpreted without the electrode effects or the electronic nature of the interfaces (Schottky junction, Ohmic junction and etc.). Quite a number of studies including papers from our group have revealed that the presence of ferroelectric polarization has a strong impact on the nature of the electronic structure of the interfaces and that this becomes, in fact, a design parameter in such systems. Thus, the main concern in this thesis is to investigate the electrical properties such as the capacitance-voltage (C-V) and current-voltage (I-V) behavior of  $\text{Ba}_x\text{Sr}_{1-x}\text{TiO}_3$  films in relation to the electrode/ferroelectric film interface [15]–[17]. As the strength of the ferroelectric polarization determines the extent of the aim was to change the compositional structure combined with changing electrode type to magnify the plausible mechanism governs the electrical responses.

## 1.1 Definitions and Properties

Ferroelectricity is a property of materials that possess spontaneous electric polarization. It is due to presence of electric dipoles and applying external electric field changes the polarization. Ferroelectricity can be determined in two ways. First, ferroelectric structure has to be non-centrosymmetric. In a structure with centre of symmetry, any dipole moment generated in specific direction would be canceled by structure symmetry to zero. Second, there must also be a spontaneous local dipole moment (cause of macroscopic polarization), and central atom must be in a non-equilibrium position [18]. In a typical ferroelectric material, such as the pseudo-cubic perovskite oxide ( $\text{BaTiO}_3$ , for instance), ferroelectricity arises from the spontaneous displacement of the positively charged Barium (Ba) and titanium (Ti) cations against the negatively charged oxygen anions. Ferroelectric distortion originates from the bonding preferences of the Ti ion, which is slightly “too small” for its coordination cage inside the oxygen octahedra. Placing slightly off-center, the Ti ion can be in a better distribution of bond distances, hence the lowering of the Coulomb interactions, lowering the energy of the material. In

Figure 1-2, the Ti ion can equivalently move towards the “top” or the “bottom” of the cage, thereby leading to the “up” and “down” states, either of which has a lower energy than the undistorted configuration. (This picture is an oversimplification; in actuality, all of the atoms move and many forces contribute) Ferroelectric materials, such as  $\text{BaTiO}_3$ , acquire an electric polarization because the crystal lowers its energy (blue curve) when positively charged ions (green and blue) displace relative to negatively charged ions (red). (Displacement of Ba ions not shown, for clarity) In most materials this energy gain is overwhelmed by the energy cost to the crystal (yellow curve) in the presence of the depolarization field—the internal electric field that comes from the displaced ions.

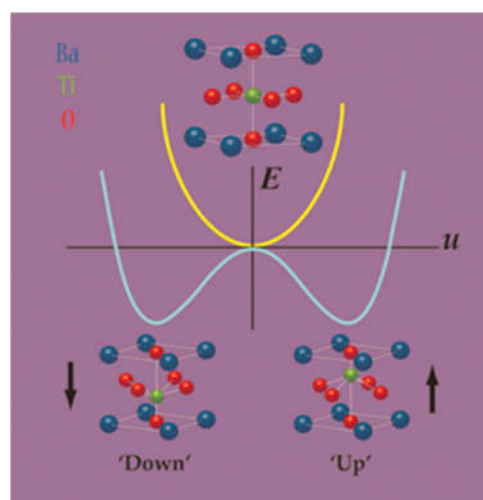


Figure 1-2: Energy state of lattice cell due to displacement of Ti atom in  $\text{BaTiO}_3$  structure [19].

Many ferroelectrics can't spontaneously polarize in vacuum, or often, in air. The reason is that if all of the positive cations move in the same direction, then positive charge will accumulate on one surface and negative charge on the other. Gauss's law tells us that these charges will produce a strong electric field that counteracts the displacement of the cations, essentially pushing them back into their positions in the non-ferroelectric structure. The depolarization field has a large and positive electrostatic cost, which can overwhelm the energy gained through the ferroelectric distortion. In ferroelectric materials less than about 10 nanometers in thickness, even a small residual depolarization field can completely suppress ferroelectricity [20], [21]. Non-electroded films can develop stripe domain structures where the polarization sign alternates along the sample plane at a given period [22]. Such a "domain" formation is favorable as the alternating sign of polarization charges at the surfaces can minimize the depolarizing fields and allow the stable ferroelectric state to exist. One other way to suppress the depolarization field is to sandwich the ferroelectric between short-circuited metallic electrodes, so that the free charges at the electrode surfaces exactly neutralize the polarization charges. Device applications of ferroelectrics almost always require the ferroelectric to be in contact with an electrode at least on one side, providing some degree of screening of polarization charges in proportion to the "ideality" of the electrode (whether electric field can penetrate into the electrode strongly or not). In real devices, however, this screening can never be perfect and a residual depolarization field remains. In fact, the energetic cost of the depolarization field is so high that most known materials (with some exceptions [23], [24]) lose their single-domain ferroelectric properties unless the surface charges are perfectly screened, a requirement that is very difficult to satisfy in practice. A multi-domain ferroelectric state can exist but is usually not preferred in device applications where the attractive properties of a single domain state are of interest. Ferroelectric domains can coexist along a specific crystallographic direction, in which certain atoms e.g. (Ti atoms in case of BaTiO<sub>3</sub>) displaced along given axis, leading to a dipole moment in that direction. Depending on the crystal system, there may be few or many possible axes. In ferroelectric domains, dipole moments of the unit cells in one region lie one of the six directions with respect to another region, usually in an antiparallel configuration and a cross section through such crystal illustrated in Figure 1-3.

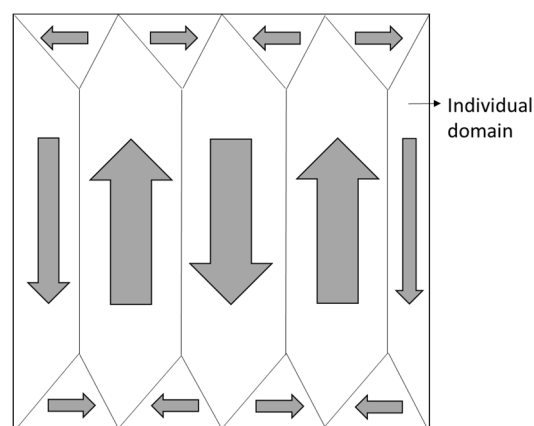


Figure 1-3: An illustration of ferroelectric domains in a crystal cross section.

## 1.2 Structure of Barium Titanate

Barium titanate ( $\text{BaTiO}_3$ ) has different crystal structures (unit cells) at different temperatures. Going from a high temperature to lower temperatures phases are cubic, tetragonal, orthorhombic, and rhombohedral crystal structure. All except the cubic structure is ferroelectric where the polarization direction corresponds to one of the crystallographic directions as depicted in Figure 1-4.

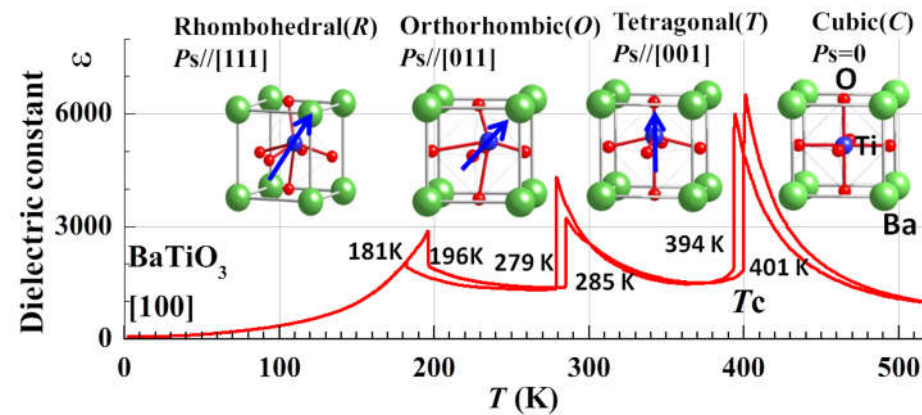


Figure 1-4: Change with temperature of the dielectric permittivity of a  $\text{BaTiO}_3$  single crystal. The schematics of Ti displacement in the oxygen octahedron of the perovskite structure are also shown [25].

All of the phases have the ferroelectric effect except the cubic phase. The high temperature cubic phase is easier to demonstrate the location of the atoms. It consists of octahedral  $\text{TiO}_6$  centers that define a cube with Ti vertices and Ti-O-Ti edges. In the cubic phase,  $\text{Ba}^{2+}$  is located at the center of the cube, with a coordination number of 12.

Above  $120^\circ\text{C}$ , cubic form of  $\text{BaTiO}_3$  has regular octahedrons of  $\text{O}^{2-}$  ions around  $\text{Ti}^{4+}$  ion and has a center of symmetry. As a result, the six Ti-O dipole moments along  $\pm x$ ,  $\pm y$ ,  $\pm z$  cancel each other and the material in such a state is called paraelectric. Below  $120^\circ\text{C}$ , cubic phase of  $\text{BaTiO}_3$  transforms to a tetragonal (noncentrosymmetric phase) which one of the axis becoming longer, usually referred as z-axis or [001]-direction. Unilateral displacement of the positively charged  $\text{Ti}^{4+}$  ions against surrounding  $\text{O}^{2-}$  ions occurs to give rise to net permanent dipole moment. Coupling of such displacements and the associated dipole moment is a necessity for ferroelectricity. This transformation forces Ti ions go to lower energy off center positions, giving rise to permanent dipoles (Figure 1-5).

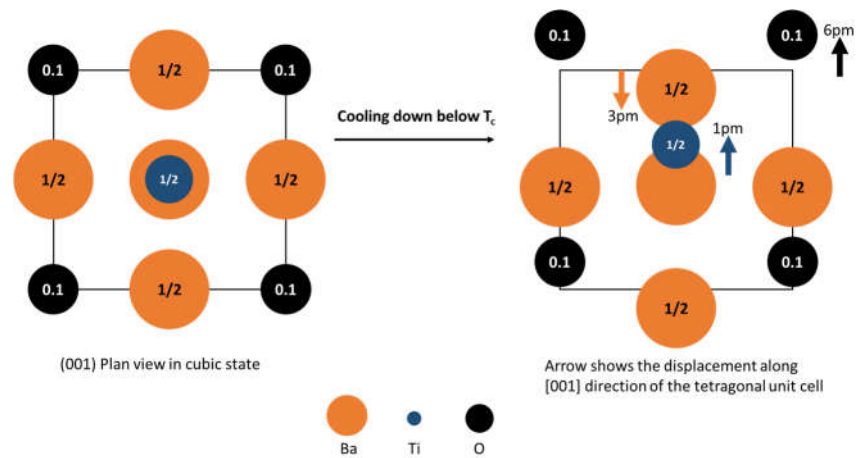


Figure 1-5: Distortion in BaTiO<sub>3</sub> upon cooling from cubic phase.

Since the distorted octahedra are coupled together in ferroelectric phase, there exists a noticeable spontaneous polarization,  $\sim 25 \mu\text{C}/\text{cm}^2$ , leading to a large dielectric constant,  $\sim 160$ , and large temperature dependence of dielectric constant.

BaTiO<sub>3</sub> shows two other structural transitions while cooled down below 120°C. First transition is orthorhombic structure at  $\sim 5^\circ\text{C}$  and then to a rhombohedral structure at  $\sim -90^\circ\text{C}$ . As a result of alteration in the symmetry, the polarization vector also changes from [001] in tetragonal to [110] in orthorhombic and [111] in rhombohedral structure.

### 1.3 Structure of Barium Strontium Titanate

The most important and common feature of the ferroelectric perovskite oxides is that they have metal-oxygen bond in form of octahedron in the unit cell which reported to be source of ferroelectric characteristic in such materials. Passing Curie point to the lower temperatures causes a small displacement of cations with respect to the position of the anions [26]. As a result of such displacement, a net dipole moment between the mass centers of the ions occurs. Here, the long range Coulomb forces are reported to be the source of ferroelectricity [27]. In a simplified definition, ferroelectricity in perovskite oxides is correlated to the tetragonality of the lattice. Tetragonality can be expressed as the ratio of the lattice parameter along the direction of applied electric field over the lattice parameter along the direction perpendicular to the applied electric field. Doping and changing the composition are one of the effective ways to change the tetragonality of bulk perovskite oxide materials and hence alter the ferroelectricity [28], [29]. On the other hand, in the thin film deposition, effect of the substrate and size effect have also very significant importance [30]. Thus, composition and the substrate effects (through the misfit) exhibit an interplay that do impact the electrical properties of these systems, the Curie point in particular.

Barium Strontium Titanate (BST) in different composition ( $\text{Ba}_x\text{Sr}_{1-x}\text{TiO}_3$ ) is a solid solution of Barium Titanate ( $\text{BaTiO}_3$ ) and Strontium Titanate ( $\text{SrTiO}_3$ ) which can be formed in entire range of  $x$  ( $x=0,0.3,0.5$ ). Although both  $\text{BaTiO}_3$  and  $\text{SrTiO}_3$  possess the Perovskite structure, the BST structure is considered as a complex perovskite structure due to the presence of the  $\text{Sr}^{2+}$  and  $\text{Ba}^{2+}$  in A-site of the lattice structure. In perovskite structures, the lattice constant is always assumed near  $4\text{\AA}$  due to the oxygen ionic radius of the  $1.35\text{\AA}$ .

The structure and property relationship in bulk state of BST has been well reviewed in the studies [31]–[33]. The ferroelectric transition temperature is nearly a linear function of Ba/Sr ratio (Figure 1-6). The shaded region in Figure 1-6 is considered as the region of interest in this thesis. Adding Sr into BTO structure causes the paraelectric to ferroelectric transition temperature  $T_c$  decrease linearly and 30% of STO, the transition happens near the room temperatures.

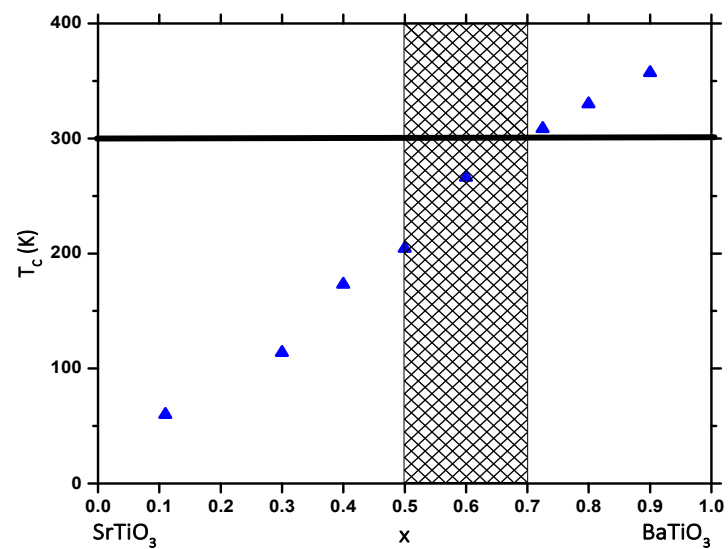


Figure 1-6: Ferroelectric transition temperature as a function of Ba/Sr ratio in bulk BST [34].

Figure 1-7 represents the crystal structure of BST composition as a function of Ba/Sr ratio. At the Ba-rich side, the structure has a tetragonal unit cell and at the Sr-rich side, the structure has a cubic unit cell. The separation edge between tetragonal and cubic symmetry is around  $x=0.3$  which consist with the reported results.

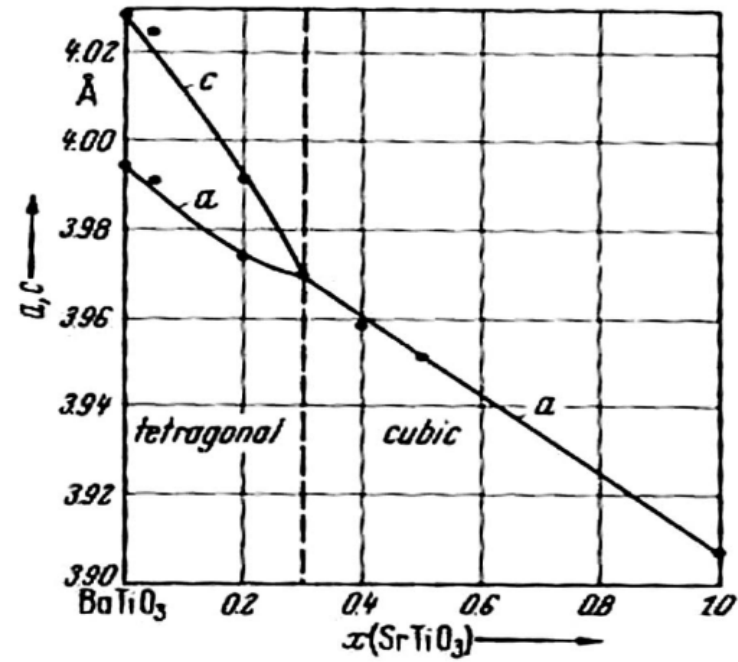


Figure 1-7: Crystal structure of BST composition as a function of Ba/Sr ratio [34].

The dielectric constant of BST composition is significantly large, especially near the Curie temperature. For BST with  $x = 0.60$ , for example, the maximum dielectric constant is  $\sim 15,000$  at room temperature (RT) as this is the composition that happens to have a Curie point close to RT. High dielectric constant of BST composition makes it a promising material for capacitors applications. Figure 1-8 represents the detailed information about temperature dependence of dielectric constant of BST composition.

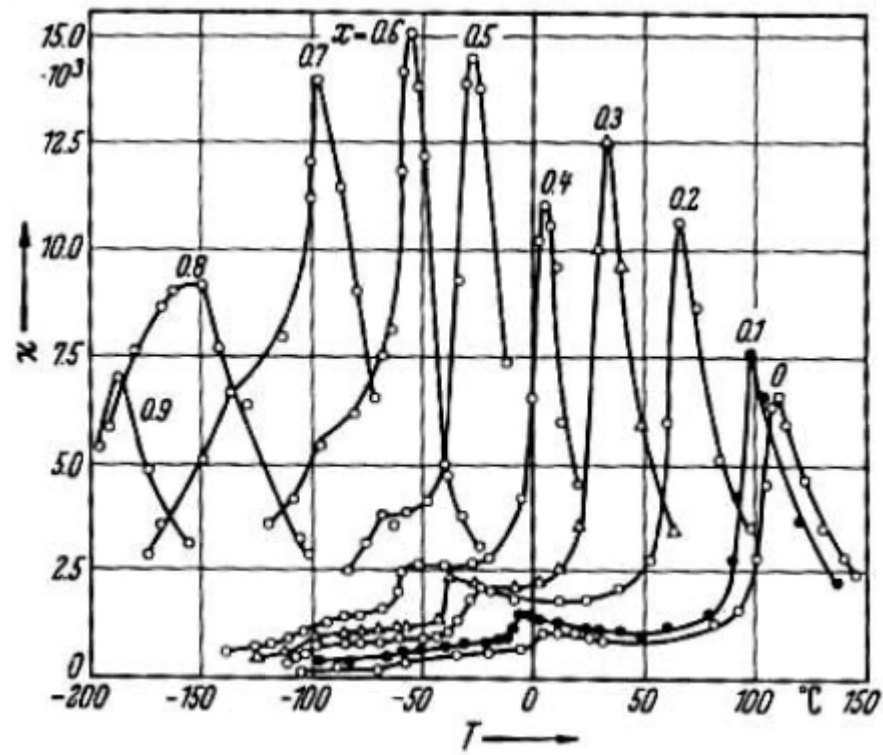


Figure 1-8: Temperature dependence of dielectric constant for BST ceramics with different Ba/Sr ratio [34].

## 1.4 Electrical Properties

### 1.4.1 Polarization-Electric Field (P-E) Loops

Domains' ability to switch from one state to another under external electric field can be observed by a measurement of the polarization as a function of an magnitude of electric field, in which it takes the form of a hysteresis loop [35]. Hysteresis (P-E) loops are obtained from measurements of charge flowing through a sample as a result of a time-dependent voltage applied across it. Charge–voltage schematics for some common circuit are shown in Figure 1-9. For an ideal linear capacitor the charge is proportional to the electric field voltage so the loop is a straight line whose gradient is equal the capacitance of the material and is proportional to the permittivity (Figure 1-9-a).

According to Ohm's Law, the current is proportional to the voltage for an ideal resistor. Therefore, depending on time, there is an amount of charge that flows and a phase difference between the charge and the electric field for a cyclical voltage. Because of this the loop is a circle with the centre at the origin. In this case the measured charge relates to the current rather than the polarization (Figure 1-9-b). The loop in Figure 1-9-c belongs to a lossy capacitor, where the area within the loop is proportional to the loss tangent of the device, and the slope proportional to the capacitance. Loss can be due to dielectric hysteresis or leakage current or both. Figure 1-9-d shows the loop for a true ferroelectric. These loops are usually centered on zero and for both the lossy capacitor and the ferroelectric they cross the y axis at a non-zero value. In the ferroelectric case this crossing point provided a measure of the remanent polarization. For the lossy capacitor the non-zero crossing point does not indicate any remanence. Caution must be exercised in interpreting the crossing point on the charge (polarization) axis as ferroelectric remanence, particularly where there may be leakage currents or the ferroelectric behavior is not clearly established. There are many examples where lossy dielectric loops have been incorrectly presented as evidence of ferroelectric behavior [17], [36], [37].

Information, about tuning driving components like piezoelectric, can be provided by the P-E loop, on the capacitance and loss of a device at high fields and at different frequencies. In applications, such as thin film ferroelectric memories, the crucial parameters can be defined and the long and short term performance of the devices can be investigated by the help of the hysteresis of the material and measurement of the P-E loop.

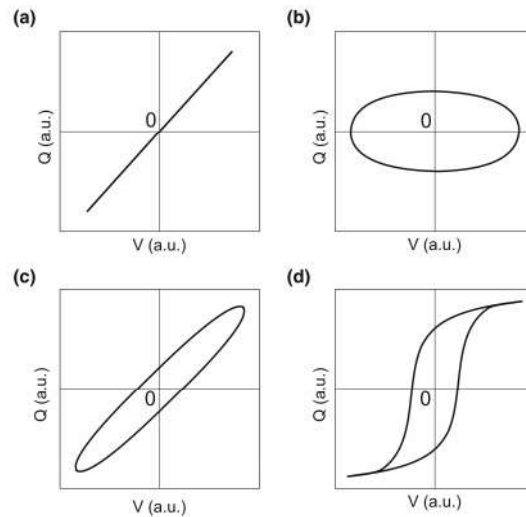


Figure 1-9: Schematic charge voltage response (in arbitrary units) of a) linear capacitor, b) resistor, c) lossy capacitor and d) ferroelectric[38].

Since polarization is a function of external applied electric field, hysteresis loop diagram interpretation is based on Polarization (P) and external electric field (E). In Figure 1-10, in the origin  $P = 0$  and  $E = 0$ . Ramping up the field (Path 1), the polarization gradually increases towards a saturation point (Path 2) in which electric field coherently orients all unit cells. By further increase in the field, dielectric charging enhances the polarization (Path 3). In the point that field is decreased to zero, the polarization decreases, however a little of polarization remains fixed. In this point  $E=0$  and polarization value is called the remnant polarization ( $+P_r$ ). By increasing the field in the opposite direction, in a specific field intensity called the coercive field  $E_c$ , an abrupt switch occurs in polarization. By further increasing the field, the polarization saturates and a dielectric response is reached again to an extreme point (Path 6). In a repeated reverse cycling result of P-E characterization is symmetric, and  $\pm E_c$  are mark points.

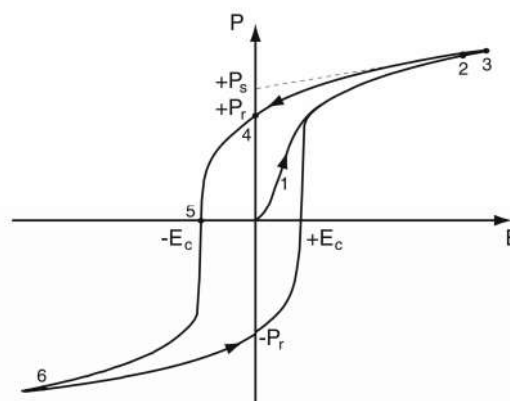
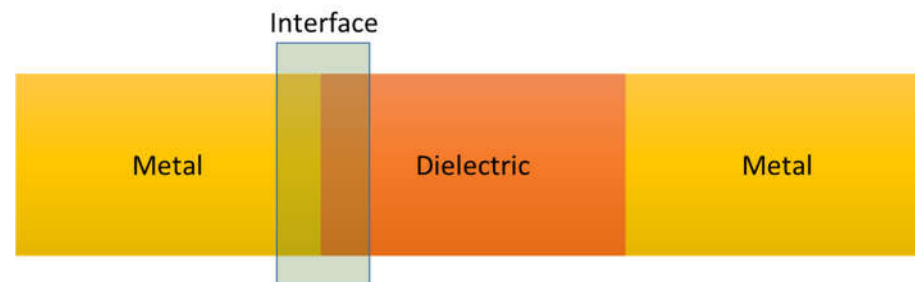


Figure 1-10: A perfect hysteric behavior of the ferroelectric polarization in an applied external electric field [35].

The most classical way to study the characteristic of the metal-film interface is place a dielectric between two metallic electrodes in a form of metal-dielectric-metal (MDM) (see Figure 1-11).



**Figure 1-11: An illustration of metal-dielectric interface in an MDM configuration.**

Here the discussion will be based on the ferroelectric materials which can be considered a wide band gap semiconductor [39]. Hence, at first a simple metal-semiconductor interface with no polarization induced effect will be discussed. Then a well-known model for study the effect of polarization will be presented. In section 1.4.4, a model based on thermodynamic approaches coupled with electrostatics and semiconductor equations for a given FE-electrode couple will be presented based on the previous studies [40], [41]. Although the importance of electrical and polarization boundary conditions (BCs) on properties of FE films is very well anticipated, only a handful of relatively recent studies have seriously tried to address their impact on the properties [41]–[44].

## 1.4.2 A Simple Metal-Semiconductor Interface

When a metal and a semiconductor are joined, they form a junction which may have two possible junction types as the result. Depending on the characteristics of metal and semiconductor used, they may form rectifying contact (Schottky barrier contact), which allows current to pass in one direction, or it could be Ohmic contact, in which case current can pass in either direction. Here, we focus on Schottky junction and consider the contact of a metal and semiconductor (n-type or p-type) and interface characteristics of it. When a metal and semiconductor are brought together, the Fermi energies of the metal and the semiconductor reaches a common equilibrium value. This is only possible via electron transfer from one to the other. In case of a metal/n-type junction as an example, electrons in the *n*-type semiconductor can lower their energy by traversing the junction. As the electrons leave the semiconductor, due to the ionized donor atoms a positive charge will be left behind. A negative field is created by this charge and the band edges of the semiconductor are lowered. Electrons flow into the metal until equilibrium is reached between the diffusion of electrons from the semiconductor into the metal and the drift of electrons caused by the field created by the ionized impurity atoms. A constant Fermi energy throughout the structure characterizes this equilibrium. In a similar manner, contacting the metal with different work function compare to semiconductor type forms various profiles of band bending in the interface (Figure 1-12).

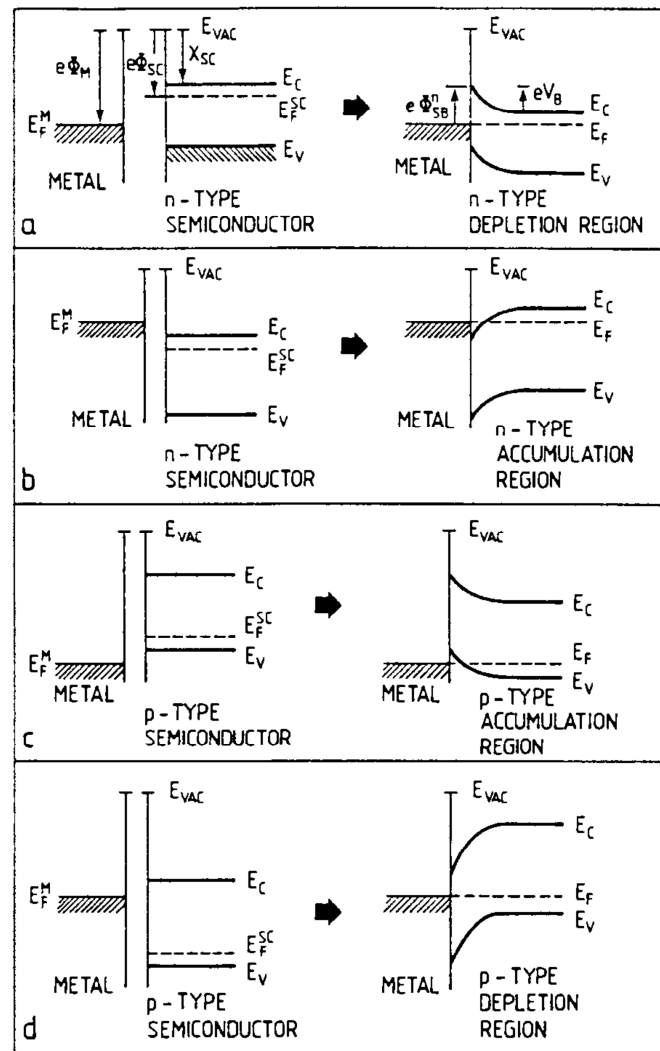


Figure 1-12: Band bending before and after metal-semiconductor contact. a) High work-function metal and n-type semiconductor, b) low work-function metal and n-type semiconductor, c) high work-function metal and p-type semiconductor, and d) low work-function metal and p-type semiconductor [45].

Since the electrostatic analysis of a metal-semiconductor junction provides knowledge about the charge and field in the depletion region, it is worth looking into. The capacitance-voltage characteristics of the diode should also be obtained. The simple analytic model of the metal-semiconductor junction is based on the full depletion approximation which is obtained by assuming that the semiconductor is fully depleted over a given distance, called the depletion region. While an accurate charge distribution is not provided by this assumption, very reasonable approximate expressions for the electric field and potential throughout the semiconductor are provided.

The full depletion approximation is now applied to an M-S junction containing an *n*-type semiconductor. The depletion region is defined to be between the metal-semiconductor interface ( $x = 0$ ) and the edge of the depletion region ( $x = x_d$ ). The depletion layer width,  $x_d$ , is unknown at this point but will later be expressed as a function of the applied voltage.

The charge density in the semiconductor is the starting point to find the depletion layer width, followed by the calculation of the electric field and the potential across the semiconductor as a function of the depletion layer width. Afterwards, the depletion layer width will be solved by requiring the potential across the semiconductor to equal the difference between the built-in potential and the applied voltage,  $\phi_i - V_a$ .

As the semiconductor is depleted of mobile carriers within the depletion region, the charge density in that region is due to the ionized donors. Outside the depletion region, the semiconductor is assumed neutral. This yields the following expressions for the charge density  $\rho$  :

$$\begin{aligned} \rho(x) &= qN_d & 0 < x < x_d \\ \rho(x) &= 0 & x_d < x \end{aligned} \tag{1-1}$$

where full ionization is assumed so that the ionized donor density equals the donor density,  $N_d$ . This charge density is shown in Figure 1-13(a). The charge in the semiconductor is exactly balanced by the charge in the metal,  $Q_M$ , so that no electric field exists except around the metal-semiconductor interface.

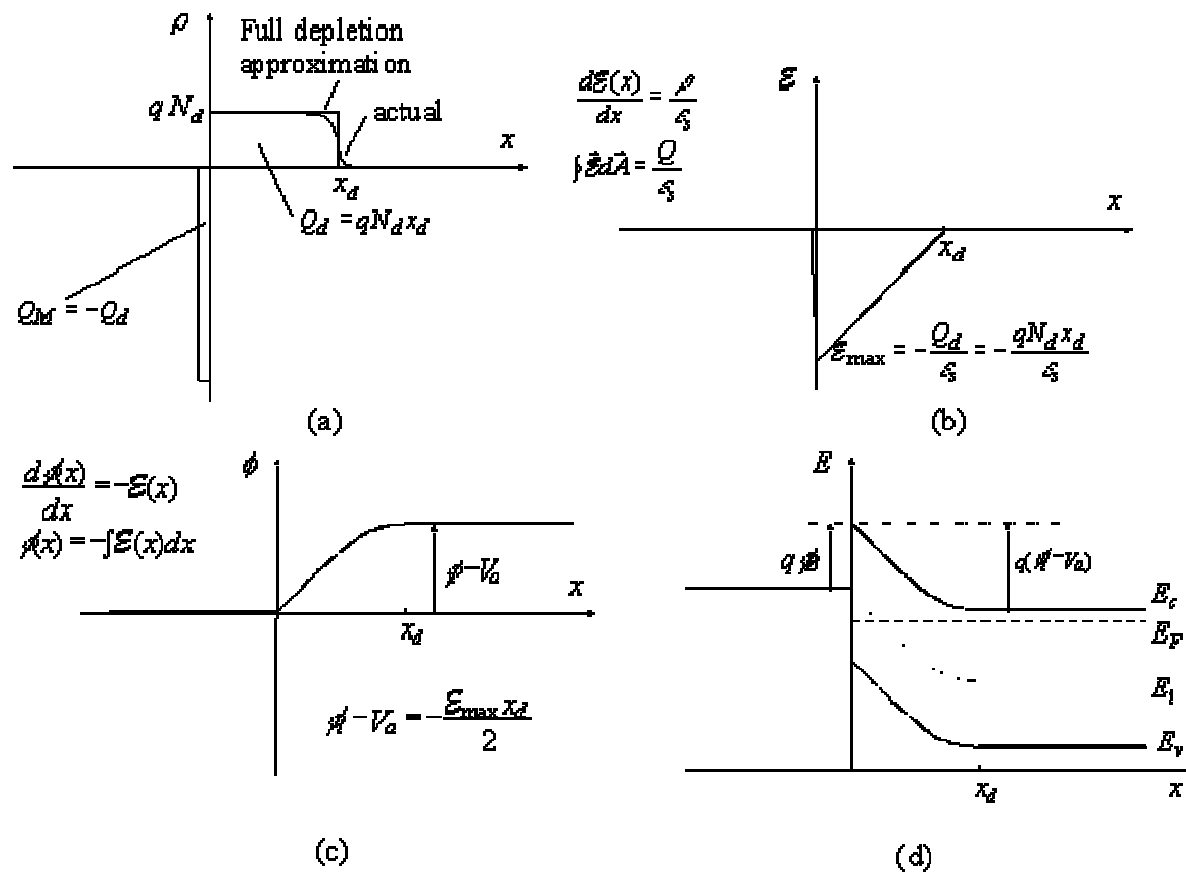


Figure 1-13: (a) Charge density, (b) electric field, (c) potential and (d) energy as obtained with the full depletion analysis.

Using Gauss's law, the electric field is obtained as a function of position, also shown in Figure 1-13(b).

$$\epsilon(x) = -\frac{qN_d}{\epsilon_s}(x_d - x) \quad 0 < x < x_d \quad (1-2)$$

$$\epsilon(x) = 0 \quad x_d \leq x \quad (1-3)$$

where  $\epsilon_s$  is the dielectric constant of the semiconductor. It is also assumed that the electric field is zero outside the depletion region, since a non-zero field would cause the mobile carriers to redistribute until there is no field. The depletion region does not contain mobile carriers so that there can be an electric field. The largest (absolute) value of the electric field is obtained at the interface and is given by

$$\epsilon(x=0) = -\frac{qN_d x_d}{\epsilon_s} = -\frac{Q_d}{\epsilon_s} \quad (1-4)$$

where the electric field is also related to the total charge (per unit area),  $Q_d$ , in the depletion layer. Since the electric field is minus the gradient of the potential, the potential is obtained by integrating the expression for the electric field, yielding:

$$\begin{aligned}
\phi(x) &= 0 & x \leq 0 \\
\phi(x) &= \frac{qN_d}{2\epsilon_s} [x_d^2 - (x_c - x)^2] & 0 < x < x_d \\
\phi(x) &= \frac{qN_d x_d^2}{2\epsilon_s} & x_d \leq x
\end{aligned} \tag{1-5}$$

It is now assumed that the potential across the metal can be neglected. The thickness of the charge layer in the metal is very thin because the density of free carriers is very high in a metal. Although the total amount of charge is the same in both regions, the potential across the metal is several orders of magnitude smaller than that across the semiconductor. The built-in potential,  $\phi_i$  in thermal equilibrium is equaled by the total potential difference across the semiconductor and is further reduced/increased by the applied voltage when a positive/negative voltage is applied to the metal. This boundary condition provides the following relation between the semiconductor potential at the surface, the applied voltage and the depletion layer width:

$$\phi_i - V_a = -\phi(x=0) = \frac{qN_d x_d^2}{2\epsilon_s} \tag{1-6}$$

Solving this expression for the depletion layer width,  $x_d$ , yields:

$$x_d = \sqrt{\frac{2\epsilon_s(\phi_i - V_a)}{qN_d}} \tag{1-7}$$

This model effectively explains a simple metal-semiconductor junction charge depletion and accumulation state without considering the effect of the ferroelectricity. However, the main concern in this thesis is to focus on a metal-ferroelectric-metal interface which will be discussed in the following section.

### 1.4.3 A model for Metal-Ferroelectric-Metal Interface

The Metal-Ferroelectric-Metal (MFM) heterostructure is a basic assembly to investigate the electrical characterization of target ferroelectric. In this prototype, metal electrodes deposited in such way that ferroelectric polarization is perpendicular on metal electrodes. Considering the ferroelectricity in such materials, electric dipoles should be oriented in head-to-tail shape inside the ferroelectric. Therefore, near one electrode there will be negative charge, and positive charge on the other interface. As a result of that, polarization state affects the classical quantities regards to metal-semiconductor Schottky contacts. Pintilie *et al.* [46] discuss a model based on metal-semiconductor interface which considers charges associated to ferroelectric polarization are present near the electrode interfaces. These charges will affect the quantities specific to classic metal-semiconductor Schottky contacts. This model was developed to take into consideration the effect of polarization charges on the interface properties [47].

According to the mentioned model, electrostatic properties of Schottky contacts are explained in the following equations:

$$V_{bi}^i = V_{bi} \pm \frac{P}{\epsilon_0 \epsilon_{st}} \delta \quad (1-8)$$

Here  $V_{bi}^i$  is built in potential;  $V_{bi}$  is built in potential in absence of polarization;  $P$  is ferroelectric polarization and  $\delta$  is distance of charge sheet in metal-ferroelectric physical interface.  $\epsilon_0$  is permittivity of the vacuum and  $\epsilon_{st}$  is static dielectric constant.

$$E_m = \sqrt{\frac{2qN_{eff}(V + V_{bi}^i)}{\epsilon_0 \epsilon_{st}}} \pm \frac{P}{\epsilon_0 \epsilon_{st}} \quad (1-9)$$

Here  $E_m$  is maximum field at the interface where  $q$  is the electron charge;  $N_{eff}$  is the effective density of space charge in the depleted region which not only consider the capacitors and ionized donors, but also consider the trapping centers carrying a net charge after capturing a charge barrier.

$$\omega = \sqrt{\frac{2\epsilon_0 \epsilon_{st}(V + V_{bi}^i)}{qN_{eff}}} \quad (1-10)$$

Here  $\omega$  is the width of the depletion region. Presence of polarization charges term affects the specific quantities earlier. The effect of polarization is not symmetric at the both interface due to the opposite signs of polarization charges. It causes a symmetrical system with the same metal electrode type on both sides which shows asymmetrical characteristics. The interface with positive charge imposes a considerable band bending since positive charges reject the hole from the interface. This rejections cause larger built-in potential comparing to polarization absence. At the other interface, smaller band bending is observable due to the attraction of holes by negative charges. Figure 1-14 is a band diagram schematic of such structure. In this diagram  $V_{bi}$  is the built-in voltage in the absence of the

ferroelectric polarization;  $V_{bi}'$  is the built-in voltage with polarization and  $\Phi_{bi}^0$  is the potential barrier in the absence of the ferroelectric polarization

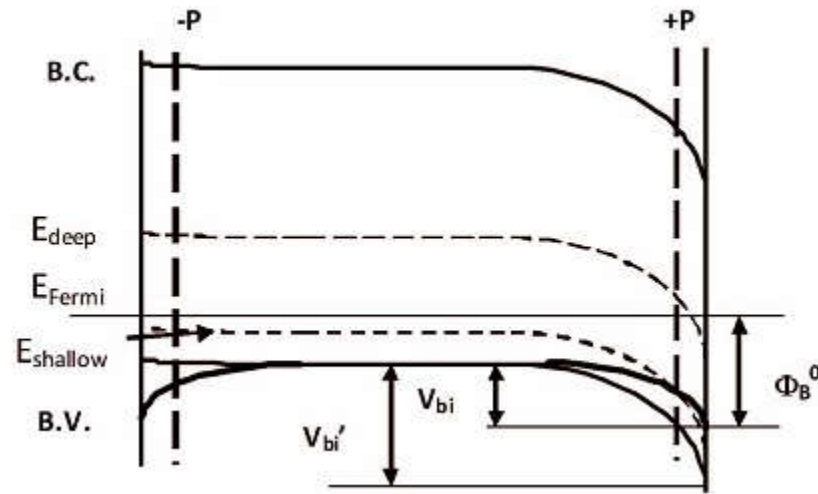


Figure 1-14: Schematic of the band diagram for a metal-ferroelectric-metal structure [46].

The model presented in this section very well explains a metal-ferroelectric-metal junction behavior before and after applying an external bias. However, this model based on the apriori assumptions was not satisfactory for our approach towards explaining the ferroelectric-metal interface characteristics under the external applied bias. Hence, in the following section we propose a computational study based on a thermodynamic model coupled with the universal equations of electrostatics and equations of semiconductors which allow us to obtain results without any prior assumption.

#### 1.4.4 Theory and Methodology for Computational Study

Here, we develop the thermodynamic theory for a given  $\text{Ba}_{1-x}\text{Sr}_x\text{TiO}_3$  composition using the phenomenological coefficients of  $\text{BaTiO}_3$  and  $\text{SrTiO}_3$ . The schematic of the  $\text{Ba}_{1-x}\text{Sr}_x\text{TiO}_3$  heterostructures analyzed here are provided in Figure 1-15.

$$S^f = (1-f) \cdot S^{PT} + f \cdot S^{ST} \quad (1-11)$$

Where  $s^f$  is any material parameter, such as the band gap, thermodynamic stiffness coefficients, unit cell lattice parameter, of a layer corresponding to a particular fraction,  $f$ , of Sr replacing Ba ions in the lattice,  $s^{PT}$  and  $s^{ST}$  are any given material parameter for pure BT and ST, respectively.  $f$  varies in this model from 0 to 0.7, corresponding to a range of Curie temperatures from that of pure BT in bulk ( $\sim 765\text{K}$ ) all the way to  $\sim 200\text{K}$  for  $f=0.7$ . Averaging of material properties, both thermodynamic, structural and electronic, is an approximation to serve as a means to provide us with the results that can be used to interpret certain electrical behavior observed in these structures. In such systems, we have computationally designed, the overall PE-FE phase transformation temperature ( $T_C$ ) will depend on the elastic and electrostatic BCs. As the experiment shows that all compositions considered in this thesis, namely  $\text{BaTiO}_3$ ,  $\text{Ba}_{0.7}\text{Sr}_{0.3}\text{TiO}_3$  and  $\text{Ba}_{0.5}\text{Sr}_{0.5}\text{TiO}_3$  are all ferroelectric and we shall choose a misfit strain with the substrate accordingly to be compatible with the experimental observations (Please see the C-V measurement data in section 3.2.2, Figure 3-20). In Figure 1-15 the total thickness of the films are approximately 100 nm. The material parameters of a given composition of  $\text{Ba}_{1-x}\text{Sr}_x\text{TiO}_3$  are assumed to be weighted linear average of the constituents, namely BT and ST in the following manner:

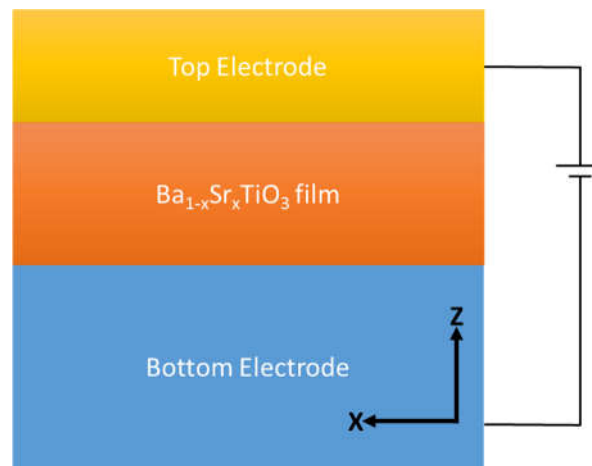


Figure 1-15: An illustration of considered profile for computational study.

We assign a small compressive misfit of -1% to each structure allowing us to treat all compositions in their respective ferroelectric regimes. We start our thermodynamic treatment by writing the total energy density of a FE heterostructure on a substrate, which is essentially the sum of the free energies of various origins (polarization, electrostatic energy, electromechanical energy and etc.):

$$F_S = \int_V F_{FE}^f dV \quad (1-12)$$

Where the integration is over the volumetric free energy of the FE film layer and  $F_{FE}^f$  is the Landau-Ginzburg-Devonshire (LGD) energy of a given composition expressed as:

$$\begin{aligned} F_{FE}^f = & \alpha_1 (P_1^2 + P_2^2 + P_3^2) + \alpha_{11} (P_1^4 + P_2^4 + P_3^4) + \alpha_{12} (P_1^2 P_2^2 + P_1^2 P_3^2 + P_2^2 P_3^2) \\ & + \alpha_{111} (P_1^6 + P_2^6 + P_3^6) + \alpha_{112} [P_1^4 (P_2^2 + P_3^2) + P_2^4 (P_1^2 + P_3^2) + P_3^4 (P_1^2 + P_2^2)] \\ & + \alpha_{123} P_x^2 P_y^2 P_z^2 - \frac{1}{2} S_{11} (\sigma_1^2 + \sigma_2^2 + \sigma_3^2) - S_{12} (\sigma_1 \sigma_2 + \sigma_1 \sigma_3 + \sigma_2 \sigma_3) - \frac{1}{2} S_{44} (\sigma_4^2 + \sigma_5^2 + \sigma_6^2) \\ & - Q_{11} (\sigma_1 P_1^2 + \sigma_2 P_2^2 + \sigma_3 P_3^2) - Q_{12} [\sigma_1 (P_2^2 + P_3^2) + \sigma_2 (P_1^2 + P_3^2) + \sigma_3 (P_1^2 + P_2^2)] \\ & + F_G^f \end{aligned} \quad (1-13)$$

where

$$\begin{aligned} F_G^f = & G_{33} \left( \frac{dP_3}{dz} \right)^2 + G_{31} \left( \frac{dP_3}{dx} \right)^2 + G_{13} \left( \frac{dP_1}{dz} \right)^2 + G_{11} \left( \frac{dP_1}{dx} \right)^2 + G_{23} \left( \frac{dP_2}{dz} \right)^2 + G_{21} \left( \frac{dP_2}{dx} \right)^2 \\ & + G_{32} \left( \frac{dP_3}{dy} \right)^2 + G_{22} \left( \frac{dP_2}{dy} \right)^2 + G_{12} \left( \frac{dP_1}{dy} \right)^2 \end{aligned} \quad (1-14)$$

In Eq. 1-3 and Eq.1-4,  $P_i$  ( $i=1,2,3$ ) is the polarization vector,  $\sigma_i$  ( $i=1,2,\dots,6$ ) is the (applied) stress tensor in contracted (Voigt) notation,  $S_{ij}$  and  $Q_{ij}$  are the elastic compliances (again in Voigt notation) at constant polarization and electrostrictive coefficients, respectively,  $\alpha_i$ ,  $\alpha_{ij}$ , and  $\alpha_{ijk}$  are dielectric stiffness (Landau) coefficients, and  $G_{ij}$  are gradient energy coefficients. For any given composition corresponding to an  $f$ , these parameters are determined from Eq. 1-11.

Taking into account that the top surface of the films are traction free results in some simplification since  $\sigma_3$ ,  $\sigma_4$ ,  $\sigma_5$ , and  $\sigma_6$  vanish, leaving us only with the in plane misfit stresses  $\sigma_1$  and  $\sigma_2$  that can be expressed in terms of the in-plane (polarization-free) misfit strain  $u_m$  for each layer such that  $\sigma_1 = \sigma_2 = C_{11} u_m + C_{12} (u_m + u_3)$  where  $u_3$  is the stress-free out-of-plane strain and  $C_{ij}$  are elastic constants at constant polarization. We point out that  $u_m$  can vary with composition in accordance with lattice parameters obtained via Eq. 1-11 which we denote as  $u_m^f$  but for convenience, we fix this for all layers for convenience as it suffices to reveal the trends in experiments as we shall show later on. Moreover, we assume that the gradient energy coefficients are isotropic and approximately the same for all compositions not to complicate further the analysis. In addition, variations in gradient energy due to possible anisotropy of this coefficient are negligibly small compared to electrostatic energy for the range of parameters (film thickness and etc.) considered in this thesis and by

no means change the physics of the problem. Eq.1-13 can be written in terms of elastic compliances and in any given layer,  $dF_{FE}^f / d\sigma_i = u_m^f$  ( $i = 1, 2$ ) to express the in-plane stresses  $\sigma_1$  and  $\sigma_2$  in terms of  $u_m^f$  and  $P_i$  reducing Eq. 1-13 to:

$$\begin{aligned}
F_{FE}^f = & \alpha_1^{fm}(P_1^2 + P_2^2) + \alpha_3^{fm}P_3^2 + \alpha_{11}^{fm}(P_1^4 + P_2^4) + \alpha_{33}^{fm}P_3^4 + \alpha_{13}^{fm}(P_1^2P_3^2 + P_2^2P_3^2) + \alpha_{12}^{fm}P_1^2P_2^2 \\
& + \alpha_{111}^{fm}(P_1^6 + P_2^6 + P_3^6) + \alpha_{112}^{fm}[P_1^4(P_2^2 + P_3^2) + P_2^4(P_1^2 + P_3^2) + P_3^4(P_1^2 + P_2^2)] \\
& + \alpha_{123}^{fm}P_1^2P_2^2P_3^2 + u_m^2 / (S_{11} + S_{12}) \\
& + G \left[ \left( \frac{dP_3}{dz} \right)^2 + \left( \frac{dP_3}{dx} \right)^2 + \left( \frac{dP_1}{dz} \right)^2 + \left( \frac{dP_1}{dx} \right)^2 \right]
\end{aligned} \tag{1-15}$$

where  $\alpha_{ijk}^{fm}$  are the misfit modified phenomenological coefficient of the Landau Ginsburg energy of ferroelectric film [25]. In addition, the potential in Eq.1-15 has to be minimized according to

$$\frac{dF_{FE}}{dP_i} - \sum_i \frac{d}{dx_i} \left( \frac{dF_{FE}}{dg_i} \right) = 0 \tag{1-16}$$

With  $g_i = dP_i / dx_i$  ( $i=1,2,3$ ). The problem can be reduced to two dimensions keeping in mind that these systems typically have symmetry with respect to one of the dimensions[48], [49] and are grown on [001] Nb:SrTiO<sub>3</sub> substrates, meaning a cross-section through the stack exposing one of the (100) or (010) planes with (001) being the base plane along the interface will be sufficient to study the properties of the compositions of interest in this thesis. Doing so and applying the procedure in Eq.1-16 for a given layer yields Euler-Lagrange equations of state for a given Sr content as:

$$\begin{aligned}
2\alpha_3^{fm}P_3 + 4\alpha_{13}^{fm}P_3P_1^2 + 4\alpha_{33}^{fm}P_3^3 + 6\alpha_{111}^{fm}P_3^5 \\
+ \alpha_{112}^{fm}(4P_3P_1^4 + 8P_3^3P_1^2) + 2\alpha_{123}^{fm}P_3P_1^4 - G \left( \frac{\partial^2 P_3}{\partial z^2} + \frac{\partial^2 P_3}{\partial x^2} \right) = E_3^f
\end{aligned} \tag{1-17}$$

$$\begin{aligned}
2\alpha_1^{fm}P_1 + 2(2\alpha_{11}^{fm} + \alpha_{12}^{fm})P_1^3 + 2\alpha_{13}^{fm}P_1P_3^2 + 6\alpha_{111}^{fm}P_1^5 + \\
2\alpha_{112}^{fm}[3P_1^5 + 3P_1^3P_3^2 + P_1P_3^4] + 2\alpha_{123}^{fm}P_1^3P_3^2 - G \left( \frac{\partial^2 P_1}{\partial z^2} + \frac{\partial^2 P_1}{\partial x^2} \right) = E_1^f
\end{aligned} \tag{1-18}$$

that link  $P_i$  to the components of the internal electric field vector  $E_i$  ( $i=1,2,3$ ).

Using the Poisson relation  $\nabla_j \cdot D_i = \rho$  ( $i,j=1,2,3$ ) which correlates the dielectric displacement vector  $D_i$  ( $i=1,2,3$ ) to the local free charge density  $\rho$ , one can then establish links between the local (scalar) electrostatic potential  $\phi$  and the polarization gradients such that:

$$\frac{d^2\phi^f}{dx^2} + \frac{d^2\phi^f}{dz^2} = \frac{1}{\epsilon_b\epsilon_0} \left( \frac{dP_1}{dx} + \frac{dP_3}{dz} - \rho(r) \right) \quad (1-19)$$

$$\rho(r) = q \left[ -n^-(r) + p^+(r) + N_d^+(r) \right] \quad (1-20)$$

In the above relation,  $q$  is the elementary charge,  $n^-(r)$  is the free electron density,  $p^+(r)$  is the hole density,  $N_d^+(r)$  is the ionized donor density,  $\epsilon_0$  is dielectric permittivity of vacuum (in SI units),  $\epsilon_b$  is a background dielectric constant (taken as 7 here) [50]. Each of these charge terms depend on the electronic band parameters and local electrostatic potential and are described using Fermi-Dirac distribution functions as:

$$N_d^+ = N_D \left[ 1 - \left( \exp\left( \frac{q(E_D - E_F - \phi)}{kT} \right) + 1 \right)^{-1} \right] \quad (1-21)$$

$$n^- = N_C \left( \exp\left( \frac{q(E_C - E_F - \phi)}{kT} \right) + 1 \right)^{-1} \quad (1-22)$$

$$p^+ = N_V \left[ 1 - \left( \exp\left( \frac{q(E_V - E_F - \phi)}{kT} \right) + 1 \right)^{-1} \right] \quad (1-23)$$

where  $N_C$  is the effective density of states at the bottom of the conduction band,  $N_V$  is the effective density of states at the top of the valence band,  $E_C$  is the energy of an electron at the bottom of the conduction band,  $E_V$  is the energy of an electron at the top of the valence band,  $E_F$  is the Fermi level, and  $E_D$  is the ionization energy of the donor site that is taken with respect to the bottom of the conduction band. Note that band edges here shift only due to the internal electrostatic potential and are considered to be free from variations in the dispersion relation due to the presence of impurities (including vacancies), which, according to Tingting *et al.*, can shrink the band gap energy by almost 0.5 eV[51], [52]. The thermodynamic coefficients and other material parameters used in the computations are provided in Table 1.[39].

Table 1: Material parameters and thermodynamic coefficients for BTO and STO used in the calculations [53],[54]

| Parameters  | SrTiO <sub>3</sub>                  | BaTiO <sub>3</sub>                  |
|---|-------------------------------------|-------------------------------------|
| Lattice parameter (nm)                                  | 0.3904                              | 0.4004                              |
| T <sub>c</sub> (°C)                                     | -250                                | 130                                 |
| C (10 <sup>5</sup> °C)                                  | 8×10 <sup>5</sup>                   | 1.5×10 <sup>5</sup>                 |
| α <sub>11</sub> (N m <sup>6</sup> /C <sup>4</sup> )     | 6.8×10 <sup>9</sup>                 | 3.6×(T-175) ×10 <sup>8</sup>        |
| α <sub>12</sub> (N m <sup>6</sup> /C <sup>4</sup> )     | 2.74×10 <sup>9</sup>                | -0.0345×10 <sup>8</sup>             |
| α <sub>111</sub> (N m <sup>10</sup> /C <sup>6</sup> )   | 0                                   | 6.6×10 <sup>9</sup>                 |
| α <sub>112</sub> (N m <sup>10</sup> /C <sup>6</sup> )   | 0                                   | 18.14×10 <sup>8</sup>               |
| α <sub>123</sub> (N m <sup>10</sup> /C <sup>6</sup> )   | 0                                   | -7.45×10 <sup>9</sup>               |
| S <sub>11</sub> (10 <sup>-12</sup> N/m <sup>2</sup> )   | 5.546                               | 8.3                                 |
| S <sub>12</sub> (10 <sup>-12</sup> N/m <sup>2</sup> )   | -1.562                              | -2.7                                |
| S <sub>44</sub> (10 <sup>-12</sup> N/m <sup>2</sup> )   | 9.24                                | 9.24                                |
| Q <sub>11</sub> (m <sup>4</sup> /C <sup>2</sup> )       | 0.0457                              | 0.11                                |
| Q <sub>12</sub> (m <sup>4</sup> /C <sup>2</sup> )       | -0.0135                             | -0.043                              |
| Q <sub>44</sub> (m <sup>4</sup> /C <sup>2</sup> )       | 0.00975                             | 5.165×10 <sup>-2</sup>              |
| g (10 <sup>-10</sup> J m <sup>3</sup> /C <sup>2</sup> ) | 6                                   | 6                                   |
| N <sub>v</sub> , N <sub>c</sub>                         | 10 <sup>25</sup> , 10 <sup>25</sup> | 10 <sup>25</sup> , 10 <sup>25</sup> |
| E <sub>v</sub> , E <sub>c</sub> , E <sub>d</sub> (eV)   | -7.1, -3.9,-4.0                     | -6.72,-4.0,-4.1                     |

One needs to simultaneously solve Eq.(1-15)-(1-23)with the top-bottom interface polarization boundary conditions (BCs) given as:

$$\lambda \frac{\partial P_1}{\partial x} - P_1 = 0 \Big|_{z=0,h} \quad (1-24)$$

And

$$\lambda \frac{\partial P_3}{\partial z} - P_3 = 0 \Big|_{z=z=0,h} \quad (1-25)$$

where  $\lambda$  is the extrapolation length determining the extent of change of polarization along the film normal at the interface and  $h$  is the total thickness of the film.  $h$  is given as the product of the number of grid points along the  $z$ -axis (thickness)  $n$  and the distance between two grid points  $d$ , taken in our computations as 0.5 nm. The BCs for electrostatic potential are specified at the  $\text{Ba}_{1-x}\text{Sr}_x\text{TiO}_3$ -electrode interfaces as 0V for short circuiting or  $\phi = \pm V_{app}$  at top electrode ( $z=100$  nm,  $n=200$ ) while the bottom electrode ( $z=0$  nm,  $n=1$ ) is kept at zero (grounded) where  $V_{app}$  is applied voltage. Periodic BCs are employed along the plane of the structures for both the electrostatic relations and the polarization. Note that the amount of charge transfer between the FE and the electrode will depend on the Fermi level differences of the stack and the electrodes as well as direction of  $P_i$  and the internal built-in fields. As such, we resort to numerical methods to analyze the electrical and dielectric properties of the compositions of interest. Ideal metal electrodes are assumed to behave as top contacts for which work function is taken as that of Pt or Cu, common electrodematerials. The Fermi level of the stack is equilibrated with that of the  $\text{Nb}:\text{SrTiO}_3$  as the substrate is very thick and is supposed to act as a reservoir of carriers due to its n-type nature. The charges due to the spontaneous polarization of the FE layer at the  $\text{Ba}_{1-x}\text{Sr}_x\text{TiO}_3$ -top electrode interfaces are assumed to be partially screened in accordance with the formation of a thin dead layer that is the case with any metallic electrode. The average of amplitude of the out-of-plane polarization  $\langle |P_3| \rangle$  is saved after each run for a given  $T$  and position in the computational grid such that:

$$\langle |P_3| \rangle = \frac{\sum |P_3(r)|}{N} \quad (1-26)$$

where  $N=200 \cdot n$  is the total number of sites. Such a resolution allows us unambiguously determine the transition temperature since the transition from a PE to a FE in case of a MD state will amount to a zero change of average polarization. The dielectric response of the gBST stacks at or far from  $T_C$  is computed via:

$$\epsilon_r^{gFE} = \frac{(100 \times 10^{-9}) [D_3^{Top} @ V_{App} + 0.001 - D_3^{Top} @ V_{App}]}{\epsilon_0 \times 0.001} \quad (1-27)$$

at the end of 5000 iterations for a given  $T$ . Here 1 mV (0.001 V in Eq.1-27) in the denominator is the small signal bias and, therefore,  $10^4$  V/m is the small signal electric field we use to probe the dielectric response of a 100 nm thick film,  $D_3^{Top}$  is the average dielectric displacement at the top gBST/electrode interface given by  $\epsilon_0 \epsilon_b E_3^{Top} + P_3^{Top}$  with superscript "Top" indicating the very top row of the computational grid that is in contact with the top electrode Eq.1-27 contains  $V_{App}$  that, when non-zero, allows us to compute the

dielectric response under bias. We employ a finite difference discretization and carry out a Gauss-Seidel iterative scheme to solve the coupled Eqs.1-11,(1-14,15) and (1-26,27) simultaneously subject to BCs discussed above. The computation grid consists of  $N=200 \cdot n=40,000$  points for all films corresponding to a total film thickness of 100 nm. We terminate the solution after 5000 iterations that yield a difference of about  $10^{-5}$  C/m<sup>2</sup> for  $P_1$  and  $P_3$  between two consecutive steps. The result of the computational study is compared to experimental results to shed the light on the obtained results in real life experiments. One should consider this is an ideal model which proposed only to clarify some facts about ferroelectric polarization state.

### 1.4.5 Capacitance-Voltage Characteristics

The C-V measurements have a butterfly-loop shape in the case of Metal-Ferroelectric-Metal heterostructure which can be interpreted as an indication of the ferroelectricity and polarization reversal. The voltage dependence of the capacitance is explained in two cases. First, in form of the net electric field dependence of the dielectric constant and second, by the voltage dependence of the depletion layers appear at the junction between the electrode and the ferroelectric interface. In the first case the ferroelectric layer is assumed as an ideal insulator. Whereas in the second case the ferroelectric layer is regarded as a semiconductor with a voltage dependent dielectric constant [55], [56]. Also, C-V measurement can be used to extract the reversible polarization, since the DC bias can set the polarization value, while a small AC voltage yields to domain walls reversible movements [57]. The origin of the capacitance peaks in the C-V characteristics attributed to various mechanisms, including the fact that peaks can occur also in Schottky contacts  $p-n$  junctions or even in non-ferroelectric structures [58]. Pintilie *et al.* [59] reported a possible link between the maxima in capacitance and the polarization reversal in detail. Their results show that the capacitance peaks and the butterfly shape directly lead to the irreversible polarization switching (

Figure 1-16). Also, capacitance peaks can be originated from trapping defects near the Schottky contact. However, this phenomena is reversible and butterfly shape should not appear.

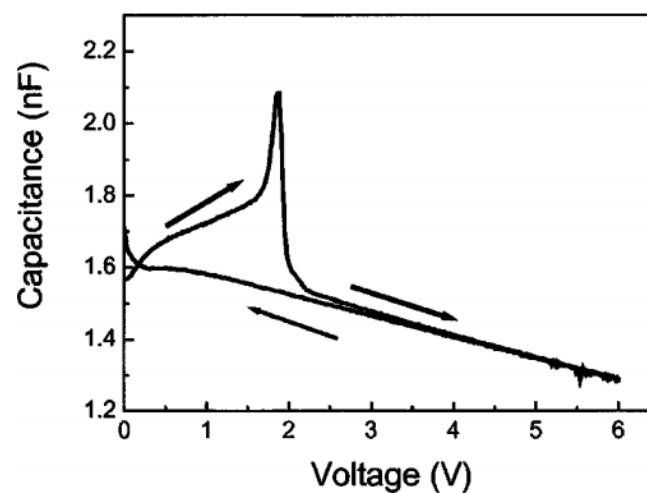


Figure 1-16: C-V characteristics at 1 kHz measured after poling the film with 6 V for one minute [59].

#### 1.4.6 Resistive Switching

Ferroelectric resistive switching (RS) or memristor effects have been observed in a number of studies and reported incessantly for several ferroelectric materials by several groups [60]–[62]. The technological applications of these materials such as resistive random access memories (RRAMs) have motivated researchers to focus on the subject. The reason is that while conventional RRAMs are functionally based on defect-mediated (ionic or electronic) process, ferroelectric RRAMs rely on the intrinsic ferroelectric domain switching instead of defects immigration[63]. Several mechanisms have been proposed to explain the resistive switching behaviors of ferroelectrics including formation/rupture of conductive filament-like structures (such as threading dislocation cores) [60], carrier- and/or defect-control of the depletion layer thickness[64] ferroelectric tunneling [65] polarization modulation of interface Schottky barrier[66]. Despite the proposed mechanism for RS in FE, the very origin of RS is still somewhat controversial, and the reported results in BTO films presenting some speculations about resistive switching [61], [67]. However, in the scientific community there is an agreement on presence of RS which can be classified into unipolar and bipolar switching according to number of degrees of freedom for an applied input. In this context, unipolar switching has only one degree of freedom: the amplitude of the applied input (either voltage or current), whereas bipolar switching involves two: the amplitude and the polarity of input. Unipolar and bipolar switching behaviors are presented by scalar and vector variable functions, respectively.

Sawa *et al.*[68] reported that the conductive filament mechanism in a Pt-Ni-Pt cell and compared the and carrier- and/or defect-control of the depletion layer thickness in a  $\text{Ti-La}_2\text{CuO}_4\text{-La}_{1.65}\text{Sr}_{0.35}\text{CuO}_4$  cell by considering the unipolar and bipolar switching respectively (Figure 1-17).

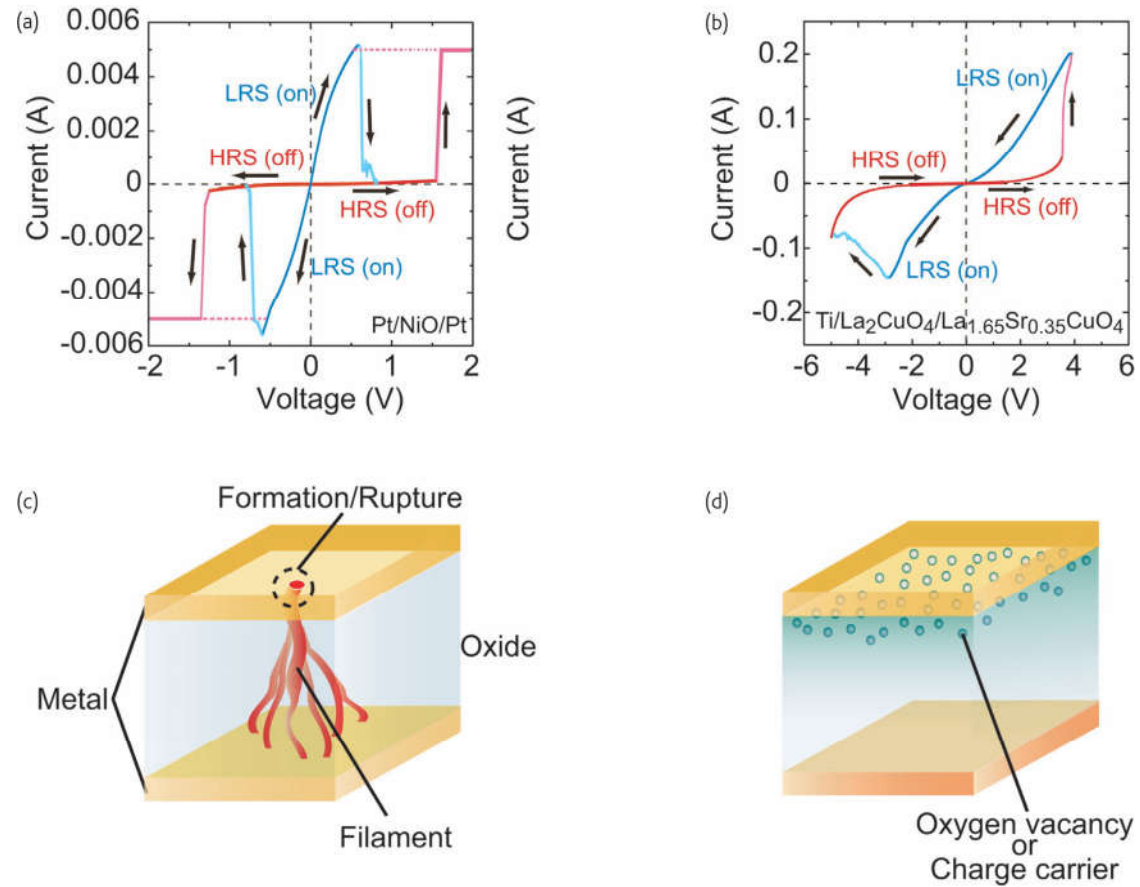
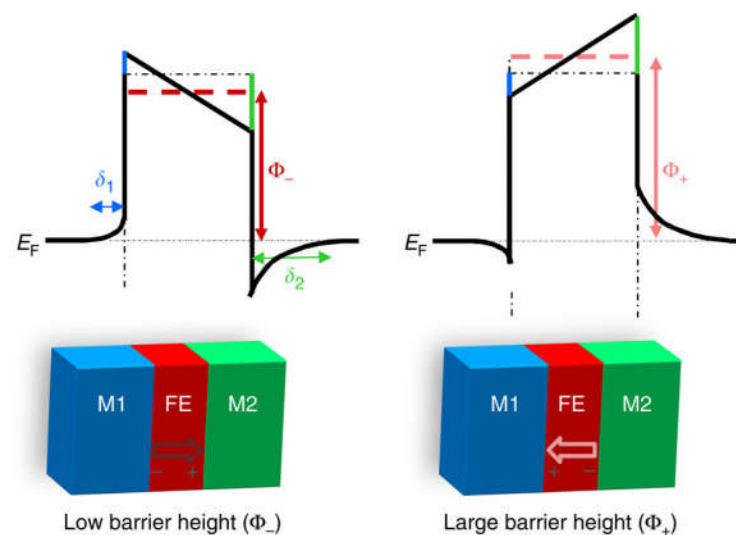


Figure 1-17: I-V curves for (a) unipolar (nonpolar) switching in a Pt-NiO-Pt cell and (b) bipolar switching in a Ti-La<sub>2</sub>CuO<sub>4</sub>-La<sub>1.65</sub>Sr<sub>0.35</sub>CuO<sub>4</sub> cell. Proposed models for resistive switching which classified according to either (c) a filamentary conducting path, or (d) an interface-type conducting path [68].

Garcia *et al.* [69] considered a metal-ferroelectric-metal interface in order to investigate the RS by tunnel junction. In their model polarization charges are usually present at the surface of a ferroelectric and depending on their sign, they attract or repel electrons. The electrons near the interface screen the polarization charges in a short distance in the electrode. This distance is beyond the distance of electron density which resumes its normal value. According to Thomas–Fermi theory, the screening length is a function of the electronic density of states at the Fermi level. In metals, the Thomas–Fermi screening length can be around couple of angstroms. In semiconductors, this length can reach 1Å while screening is imperfect. However, Stengel *et al.* [70] emphasize that the actual effective screening length differs from the one defined by Thomas–Fermi. In this case, its microscopic properties of the ferroelectric-electrode interface system strongly affect the screening length. This incomplete screening produce an additional electrostatic potential at the ferroelectric-electrode interface which indicates the direction of the polarization ( $\langle 0 \rangle$  when  $P$  points to the interface and  $\langle 0 \rangle$  when  $P$  points away from the interface). If we consider an ultrathin ferroelectric layer deposited between two different electrodes with more efficient screening on the left side than on the right side (Figure 1-18). The magnitude of the additional electrostatic potential at the electrode/ferroelectric interface is as same as the screening length over the dielectric constant of the electrode. In a simple analogy,

if we consider the initial electronic potential barrier rectangular (identical barrier heights for the left and right interfaces), we conclude that the polarization charge effects induce an asymmetric electronic potential profile [71], [72]. By reversing the polarization, the asymmetry of the electronic potential profile is reversed. Hence, the barrier height in average is higher when  $P$  points to the electrode (left) than when  $P$  points to the right side. Tunnel transmission depends exponentially on the square root of the barrier height, the junction resistive will depend on the direction of  $P$ . The asymmetry between the two different ferroelectric/electrode interfaces crucial to modulate the current transmission of the ferroelectric barrier. However, asymmetry may come from the interfaces because of different interface terminations[73]. Hence, the use of different electrode materials is not always mandatory.



**Figure 1-18:**The polarization-induced variation of the tunnel barrier height in FTJs and the potential profile across the metal 1 (M1)/ferroelectric(FE)/metal 2 (M2) heterostructure for two orientations (right and left) of the ferroelectric polarization ( $P$ ) [74].

It is known that the  $I$ - $V$  behavior of metal-Semiconductor-metal cells heavily relies on the electrode materials [62], [67], [75]. This implies the importance of property of the anode/Semiconductor (n-type) and the cathode/Semiconductor (p-type) interface for electronic carrier injection. The Schottky barrier formed at the metal/Semiconductor interface plays an important role in the electronic transport, mostly injection through the SBH. Ideally, the SBH is defined as the difference between the electron affinity of the Semiconductor and work function of the metal. The SBH is therefore supposed to be proportional to the work function of the metal. However, in reality there may be an interfacial layer between the metal and Semiconductor, which is equivalent to a thin-slab-shaped capacitor. A certain voltage drop through the layer occurs, leading to a deviation of the SBH from the ideal value as suggested by Cowley and Sze [76].

One of the first models attempting to explain ferroelectric-resistive switching reported for PTO according to the alteration of carrier-depletion width in ferroelectrics [77]. In their model, Meyer and Kohlstedt assumed a gap at the metal-ferroelectric interface, which separates the induced charge on the metal from the surface charge on the ferroelectric interface [78]. To be precise, they assumed a high depolarization field in their model. At one of the interfaces, interfacial gap is placed, i.e. asymmetric interface. Resulted asymmetry

led to polarization-dependent profiles of the ferroelectric's conduction band which induced polarization-dependent conductivity of delocalized electrons in the ferroelectric. Another model for RS is FTJ which differs from aforementioned MFM junction and rely on current transport through the ferroelectrics is quantum mechanical tunneling [79].

The charges in the FE's conduction band with respect to polarization direction leads to a change in tunneling matrix element which this leads to RS [80]. Thus, the direction of polarization determines whether quantum mechanical tunneling will occur or not for a given bias scheme on the MFM stack. According to Kohlstedt *et al.* [80], one possible way to separate RS from ferroelectric switching is the simultaneous acquisition of electric currents and ferroelectric-switching-related responses, e.g. piezoelectric response, according to the applied voltage. They have simultaneously investigated the currents and piezoelectric responses of PZT with voltage (

Figure 1-19). According to this figure, the resistive and ferroelectric switching behaviors are not coupled. In other words, the simultaneous switching of the ferroelectric polarization and resistive at the same electric field would be a precondition (but not sufficient) for ferroelectric-resistive switching. In

Figure 1-19, the ferroelectric switching appears at about  $170 \text{ kV cm}^{-1}$  ( $0.5 \text{ V}$ ) and  $-170 \text{ kV cm}^{-1}$  ( $-0.5 \text{ V}$ ) applied electric fields, while the resistive switching can be observed at about  $330 \text{ kV cm}^{-1}$  ( $0.9 \text{ V}$ ) and  $-330 \text{ kV cm}^{-1}$  ( $-0.9 \text{ V}$ ) applied electric fields [80]. In

Figure 1-19 (b) the same measurement is applied on a  $30 \text{ nm}$  thick PZT film on a LSMO electrode. This measurement was conducted using a Conductive AFM (CAFM) tip. The curves show the correlation between the piezoelectric and current responses at a tip bias of approximately  $3.3 \text{ V}$ , suggesting ferroelectric-resistive switching.

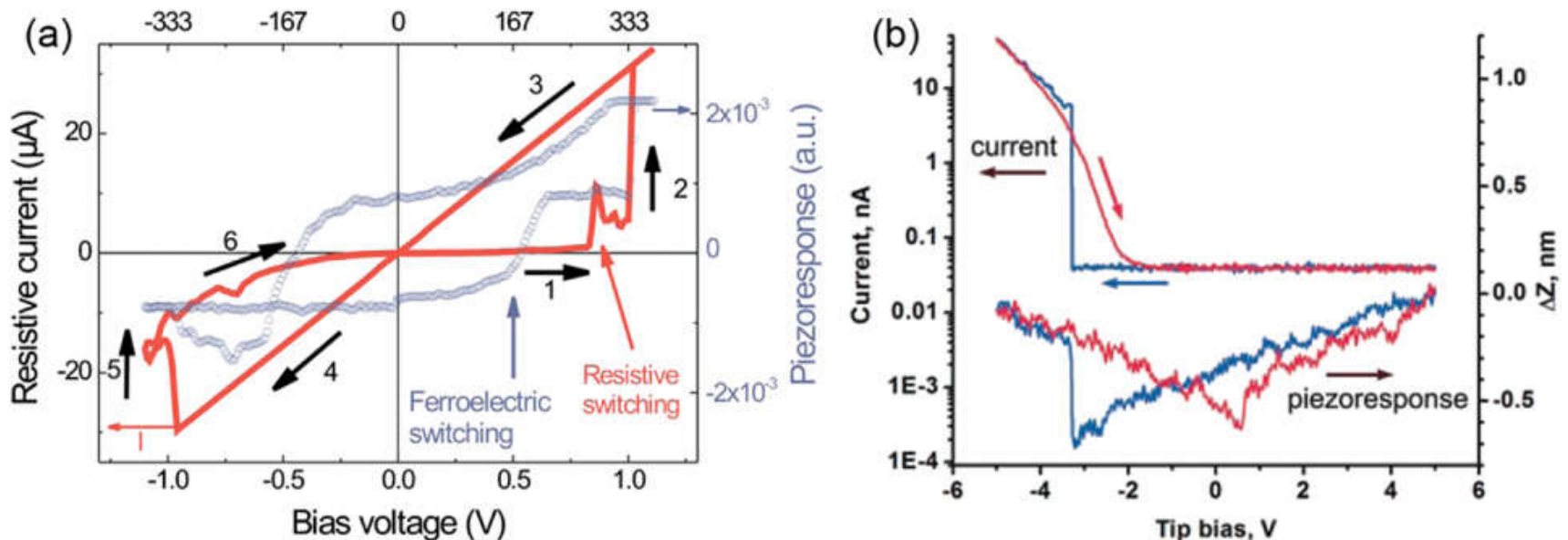


Figure 1-19: Simultaneous measurements of current and piezoelectric response of a MFM cell with a  $6 \text{ nm}$  thick PZT film [81].

Mikheev *et al.* [82] reported a systematic study of RS of Pt and Nb-doped SrTiO<sub>3</sub>. They demonstrate that RS is controlled by an interfacial layer, as shown by a parasitic interfacial capacitance, an increased ideality factor of the Schottky barrier and an extended depletion width within the SrTiO<sub>3</sub>. In their study, a charge trapping-based model can fully explain the Schottky barrier lowering that accompanies the resistive switching. The interfacial layer capacitance is an important factor in controlling the magnitude of the effect. In this study, a series of Pt-Nb:SrTiO<sub>3</sub> devices (Figure 1-20) were investigated. The interface quality was changed intentionally across this series by changing the deposition parameters. The samples are labelled A–D in which sample A (highest quality interface) consists of an all-epitaxial junction of (001)Pt grown by high-temperature sputtering. All samples were annealed in O<sub>2</sub> to eliminate any possible contributions from oxygen vacancies.

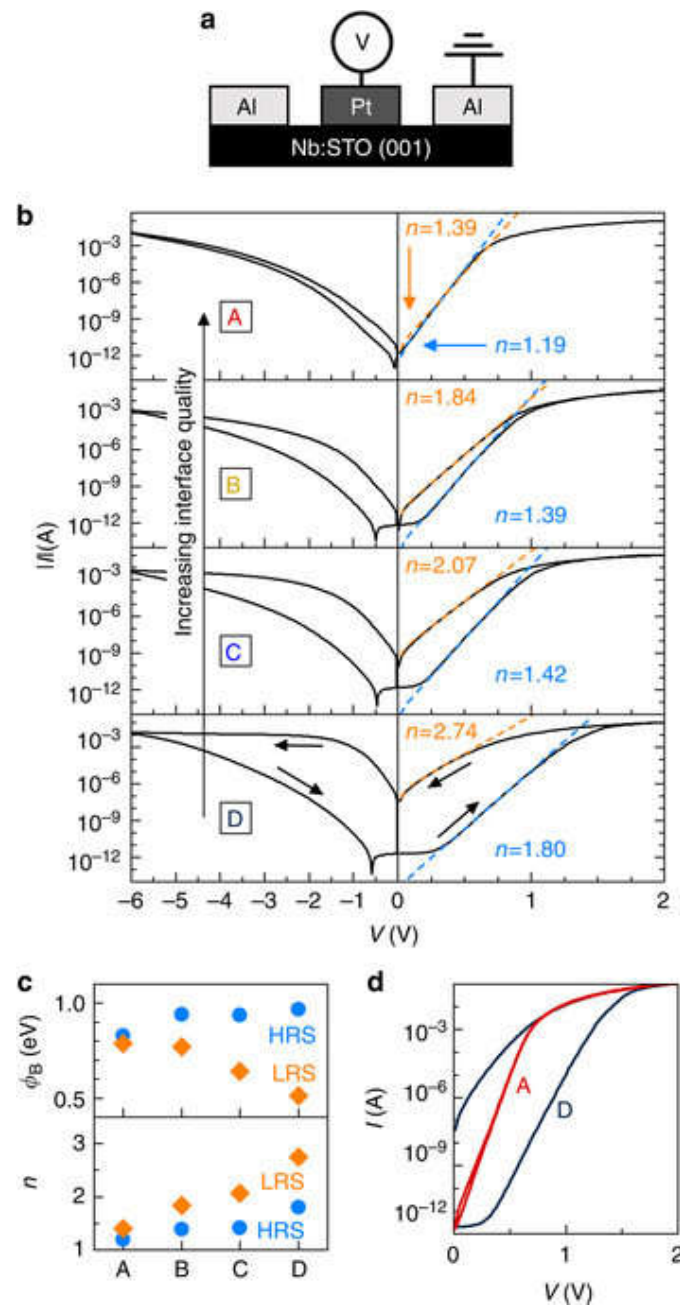


Figure 1-20: (a) Schematic of the device. (b)  $I$ - $V$  characteristics for all samples. The blue and orange lines fit to equation (1) for the, respectively, in each case. (c) Extracted barrier heights  $\phi_B$  and ideality factors  $n$ . (d) Forward bias  $I$ - $V$  for samples A and D. reprinted from [82].

Figure 1-20 (b) represents the  $I$ - $V$  characteristics of the four Pt-Nb:SrTiO<sub>3</sub> junctions. The  $I$ - $V$  hysteresis was probed by sweeping from 6V to +2V then to -6V. All samples reveal bipolar RS, with a high positive bias increasing the junction current and negative bias reversing the effect. The device RS states are referred to as low- and high-resistive states (LRS and HRS). The magnitude of the RS clearly decreases as the junction quality is improved.

To conclude, if the ferroelectric polarization points to the semiconductor, the n-type semiconductor surface will be driven by the positive bound charges in the ferroelectric-semiconductor interface into accumulation. The accumulated semiconductor can be treated as a metal and the screening is then similar to that in metal-ferroelectric-metal FTJ. The screening is generally not complete and in the ferroelectric barrier, a depolarization field opposite to the polarization develops which lowers the barrier height and generates a higher tunneling transmittance. The device is then set to a low resistive ON state (LRS) (Figure 1-21) [83].

As the polarization is reversed, pointing to the metal electrode, the semiconductor surface is depleted of electrons and the negative ferroelectric bound charges have to be screened by the immobile ionized donors. In contrast to the ON state, where majority carriers can be accumulated very close to the ferroelectric-semiconductor interface, the immobile screening charges in the depleted state spread over a space charge region defined by the doping profile. On one hand, the incomplete screening again produces a depolarization field, but this time increases the barrier height. On the other hand, the tunneling electrons have to experience an extra barrier in the depleted space charge region owing to band bending induced by ferroelectric polarization in the barrier. The tunneling transmittance can be greatly decreased by this extra barrier. The device is then set to a high resistive OFF state (HRS) (Figure 1-21)

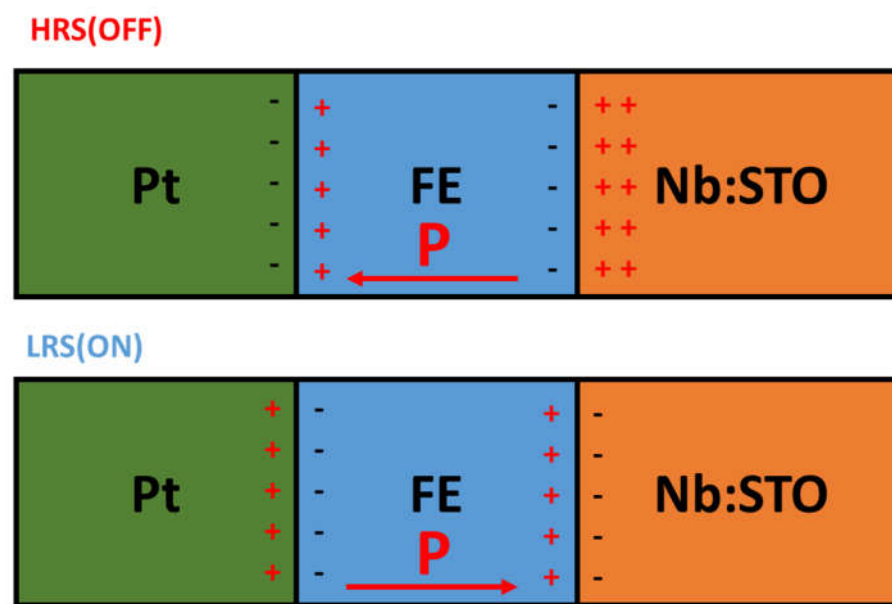


Figure 1-21: An illustration of low resistive state (LRS) and high resistive state (HRS) depending on the polarization direction.

## Chapter 2: SAMPLE FABRICATION METHOD AND PROCEDURE

### 2.1 Solution Preparation Method

In order to deposit Barium Strontium Titanate (BST) films on various substrates, spin coating technique was used. In this study, three different compositions of BST films ( $\text{BaTiO}_3$ ,  $\text{Ba}_{0.7}\text{Sr}_{0.3}\text{TiO}_3$ , and  $\text{Ba}_{0.5}\text{Sr}_{0.5}\text{TiO}_3$ ) were produced by Sol-gel method. The sol-gel method has several advantages over other deposition methods in which better stoichiometry and homogeneity control can be achieved easier. Also, in combining with spin coating deposition technique, the cost and time of sample preparation decrease considerably [84].

In overall, there are two main methods to produce thin films of oxides using Sol-gel. First one is dispersing powder of fine particles and preparing a stable solution and then depositing the film. Second one is dissolving organometallic compounds in a proper solution in which polymerization of alkoxides produces a continuous network known as gel. In this thesis, the solution preparation was based on the second method using Barium, Strontium and Titanium alkoxides.

#### 2.1.1 Barium Strontium Titanate ( $\text{Ba}_x\text{Sr}_{1-x}\text{TiO}_3$ ) Solution Preparation

For preparing the barium strontium titanate ( $\text{Ba}_x\text{Sr}_{1-x}\text{TiO}_3$ ) solution, using of the different alkoxides was proposed in literature.

Table 2-1 summarizes the list of used alkoxides reported.

**Table 2-1: Summarized list of different alkoxides in reported studies.**

| Alkoxides   | Solvent  | Reference                       |
|---|--|---------------------------------|
| Barium acetate<br>Strontium acetate<br>Titanium acetate               | Glacial acetic acid<br>Acetyl acetone  | Cheng <i>et al.</i> [85]        |
| Barium acetate<br>Strontium acetate<br>Titanium (IV) isopropoxide     | Ethylene Glycol<br>Glacial acetic acid   | Tahan D. <i>et al.</i> [86]     |
| Barium acetate<br>Strontium acetate<br>Titanium (IV) isopropoxide     | n-propanol<br>Ethylene Glycol  | E. Dien <i>et al.</i> [87]      |
| Barium carbonate<br>Strontium carbonate<br>Titanium (IV) isopropoxide | Ethylene glycol<br>Citric acid   | F. M. Pontes <i>et al.</i> [88] |
| Barium acetate<br>Strontium Acetate<br>Tetrabutyl titanate            | Methanol<br>Glacial acetic acid<br>Ethylene glycol<br>dimethyl ether<br>Acetyl acetone<br>(stabilizer) | H. Tian <i>et al.</i> [89]      |

All substances used in this thesis are used without any further purification. The information about starting substances is listed in Table 2-2.

**Table 2-2: Starting substances and information.**

| Substance name                           | Substance information          |
|--|--------------------------------|
| Barium acetate (Ba(AC) <sub>2</sub> )    | Sigma-Aldrich, CAS #: 543-80-6 |
| Strontium acetate (Sr(AC) <sub>2</sub> ) | ABCR, CAS #: 543-94-2          |
| Titanium (IV) isopropoxide (TIP)         | Sigma-Aldrich, CAS #: 546-68-9 |
| Glacial Acetic Acid (GAA)                | MERCK, CAS #: 64-19-7          |
| 2-Propanol                               | MERCK CAS #: 67-63-0           |

For preparing the solution, two separate solutions were prepared. The first solution was obtained by mixing the Ba(AC)<sub>2</sub>, Sr(AC)<sub>2</sub> with GAA. The solution was left for mixing on the stirrer for 1 hour in room temperature. The second solution was prepared by mixing the TIP and 2-propanol on the stirrer for 30 minutes in room temperature. After 1 hour, first solution was added to the second one and whole mixture was stirred for 1 hour in room temperature. The concentration of the obtained solution was 1M. In order to deposit higher quality films, 0.5M solution was prepared by diluting the 1M solution via adding GAA. The detailed information about the mixing ratio and sample coding are presented in Table 2-3.

**Table 2-3: Chemical substance mixing ratio.**

| Sample Code | Composition  | Ba(AC) <sub>2</sub> (g) | Sr(AC) <sub>2</sub> (g) | GAA (mL) | TIP (mL) | 2-Propanol (mL) |
|-------------|--|-------------------------|-------------------------|----------|----------|-----------------|
| BT          | BaTiO <sub>3</sub>                                   | 2.5542                  | 0                       | 10       | 3        | 15.5            |
| BST70       | Ba <sub>0.7</sub> Sr <sub>0.3</sub> TiO <sub>3</sub> | 1.7879                  | 0.6171                  | 10       | 3        | 15.5            |
| BST50       | Ba <sub>0.5</sub> Sr <sub>0.5</sub> TiO <sub>3</sub> | 1.2771                  | 1.0285                  | 10       | 3        | 15.5            |

### 2.1.2 Thin-film Deposition Method

Here to deposit homogenous films, the spin coating technique was used. Spin coating process can be divided into four stages: deposition, spin-up, spin off, and evaporation respectively. The spin coating process is basically illustrated below.

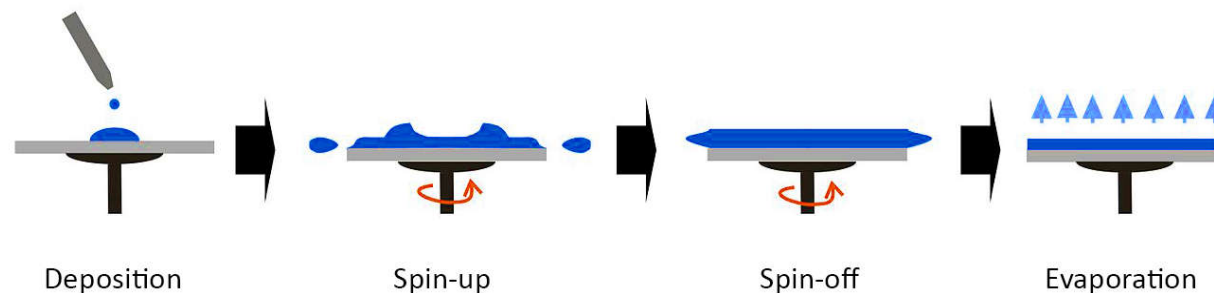


**Figure 2-1: Four stages of spin coating process.**

In the deposition stage, solution covers the substrates' surface. Homogeneity of the prepared solution has critical effect on the quality of the deposited films and it's critical that solution wets the surface. In the spin-up stage, solution entirely covers the surface. Evaporation rate and viscosity of the solution affects the dispersion in this stage while substrate is accelerated up to the desired rotation speed, in which centrifugal force moves the solution radially outward. During the spin-off stage, arrangement of the atoms is in the manner close to final desired crystalline phase. Although the evaporation rate is the final stage, during the whole process, evaporation is inevitable. However, this stage determines the final thickness of the film. In this thesis, spin coating technique parameters were considered along with several criteria for solution:

- Solvent must have proper evaporating rate: the major part of the solvent should evaporate during the spinning stage and also an excess of liquid should dispense during this stage. Any remanent liquid on the surface cause inhomogeneous film surface.
- Solvent selection is critical since viscosity and evaporating rate directly affect the quality of the film. Hence, optimizing the solvent magnitude and matching the stoichiometry are the main challenges in producing homogenous solutions.
- Solvent should wet the surface. Controlling the pH and selection of the solvent have critical effects on the quality of the films.
- Spin acceleration must be optimized since the profile of the solution flow is highly dependent on the centrifugal force. Hence, here the three step spinning is used. First step is in slow rotation in which it lets the solution disperse on the surface. Second step is the main and the fast rotation step. Speed of the third step is decreased until the spin stops. The thickness of the initial film during the spin-off can be calculated in terms of [90] :

$$h(t) = h_0 / (1 + 4\rho\omega^2 h_0^2 t / 3\mu)^{1/2} \quad (2-1)$$

Here  $h_0$  is the initial thickness,  $\omega$  is angular velocity,  $t$  is time, solution viscosity  $\mu$  and density  $\rho$  assumed as the constant values. According to the term, even if the film is not uniform in the beginning of the process, it tends to get uniform. Hence, slow spin at the beginning guarantees the homogenous dispersion of the solution on the surface, while high speed and longer spin time reduce the film thickness considerably. In this thesis, a Laurell spin coater model: WS-650-23B is used. The spin coating speed and time are optimized in forms of two steps. In the first step, spin speed is set to 500rpm for 15 seconds and next step 6000rpm for 60 seconds. In this thesis, six samples are prepared in three different compositions two of which are different metal electrodes deposited on them separately.

### 2.1.3 Thermal Treatment of Thin-films

Further heat treatment is required to crystallize the amorphous deposited films in the form of perovskite structure. It is important to optimize the heat treatment parameters such as: heating rate, pyrolysis temperature, final sintering temperature, soaking time in each temperature and medium atmosphere. Deposited films are dried in air at 200°C for 5 min on hot plate. Then they are heated up to 400°C by 5°C /min rate. All samples are kept in 400°C for 30 min. Then samples are heated up by the same rate to 800°C and kept for 150min. Whole heat treatment process includes heating up and cooling down in oxygen rich environment. The flowchart of whole sample preparation process is shown in Figure 2-2 .

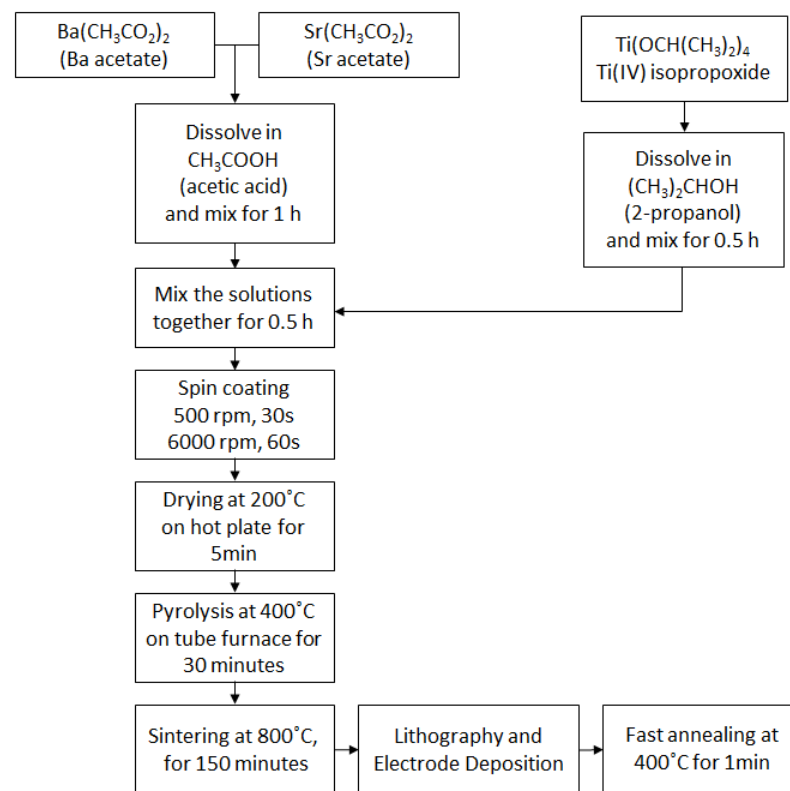


Figure 2-2: Flow chart of solution preparation, deposition thin films and post heat treatment steps.

## Chapter 3: RESULTS AND DISCUSSION

### 3.1 Structural Characterization

#### 3.1.1 X-ray Diffraction Results (XRD)

X-ray diffraction pattern of the Barium Titanate (BTO) films is measured using Bruker D8 ADVANCE X-ray ( $\text{Cu-K}\alpha$ ) diffractometer and the results are presented in Figure 3-1. The XRD pattern exhibited a set of diffraction lines attributed to a tetragonal structure with the space group  $P4mm$  confirmed from the JCPDS card number 081-2203. Besides the diffraction peaks of Nb(0.07%):STO(100) substrate, no other stray phases can be seen. The (001) and (002) peaks in XRD pattern shows a BTO film with uniformly  $c$ -axis orientation. The XRD spectrum of all compositions on Nb(0.07%):STO(100) is given in Figure 3-2.

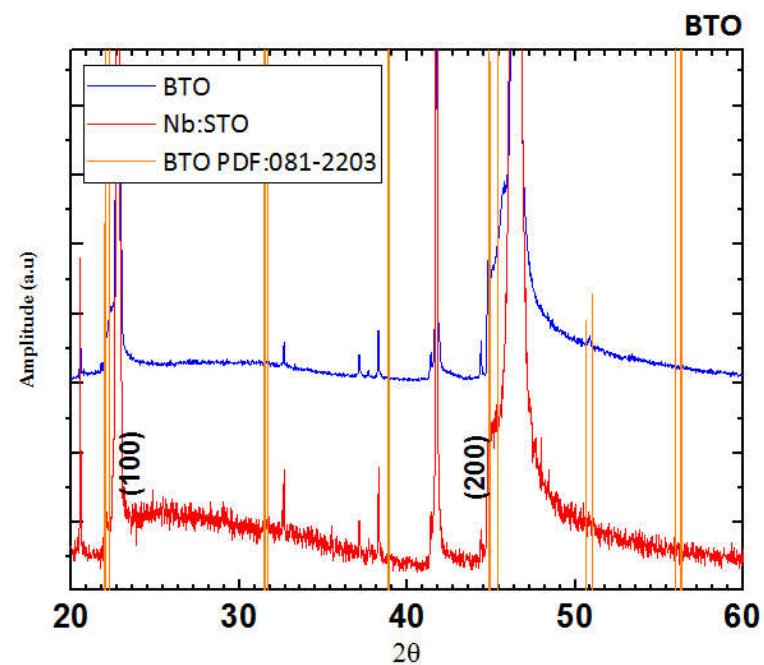


Figure 3-1: XRD pattern of BT thin-film on Nb(0.07%):STO(100) compared to Barium Titanate tetragonal structure. (JCPDS:081-2203)

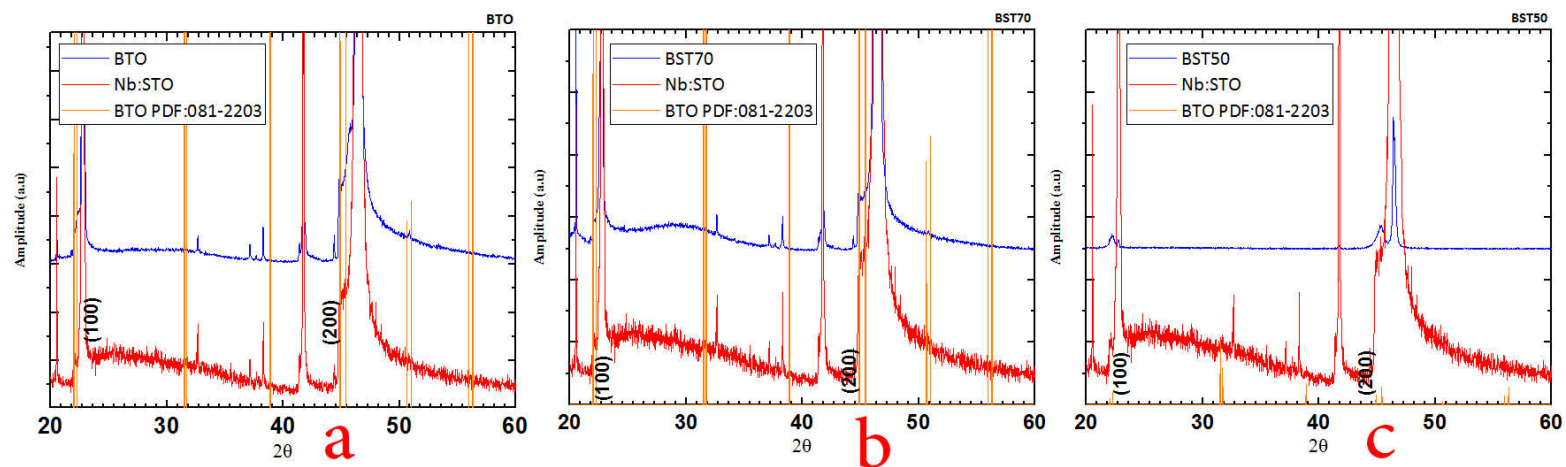


Figure 3-2: XRD spectrum of a)  $\text{BTiO}_3$  b)  $\text{Ba}_{0.5}\text{Sr}_{0.5}\text{TiO}_3$  c)  $\text{Ba}_{0.7}\text{Sr}_{0.3}\text{TiO}_3$  films grown on Nb(0.07%):STO (100) substrate.

### 3.1.2 Scanning Electron Microscopy (SEM) Results

Micrographs of the thin films surface are characterized using Leo G34 Supra 35VP. Using the scanning electron microscopy, we were able to evaluate the surface morphology of the samples. The scanning electron microscopy (SEM) is a precious tool to inspect the progress of the film deposition process. After each step of process, the thin film quality is inspected with SEM. As a result, various parameters including: the solution concentration, sintering temperature and atmosphere, electrode deposition quality and film thickness are optimized based on the obtained surface quality. In this regard, in solution concentration step, the deposited thin films were obtained from 1M solution. This solution was not stable enough and obtained films either were undesirably thick. Also, after spin coating, remnant solution crystallized on the surface of the film was not preferable (Figure 3-3). It was due to the insufficient speed rate of the spinning which couldn't spin off the solution properly. After that, the spin coating parameters were optimized in order to get homogenous films with repeatable thickness. Figure 3-4 (a) shows the surface of the film and Figure 3-4 (b) shows the vertical cross section of the film. The obtained results were repeated for all films. However, the porosity of the films was high. In order to increase the density, several heating rates and sintering atmosphere were tested. The optimum result was obtained in O<sub>2</sub> reach environment with heating rate of 1°C/min. After this process, the film qualities were desirable and electrode deposition was carried on after that.

Figure 3-5 (a) represents the thickness of the film in 50kX magnification. The thickness was measured as ~200nm (

Figure 3-5 (b)).

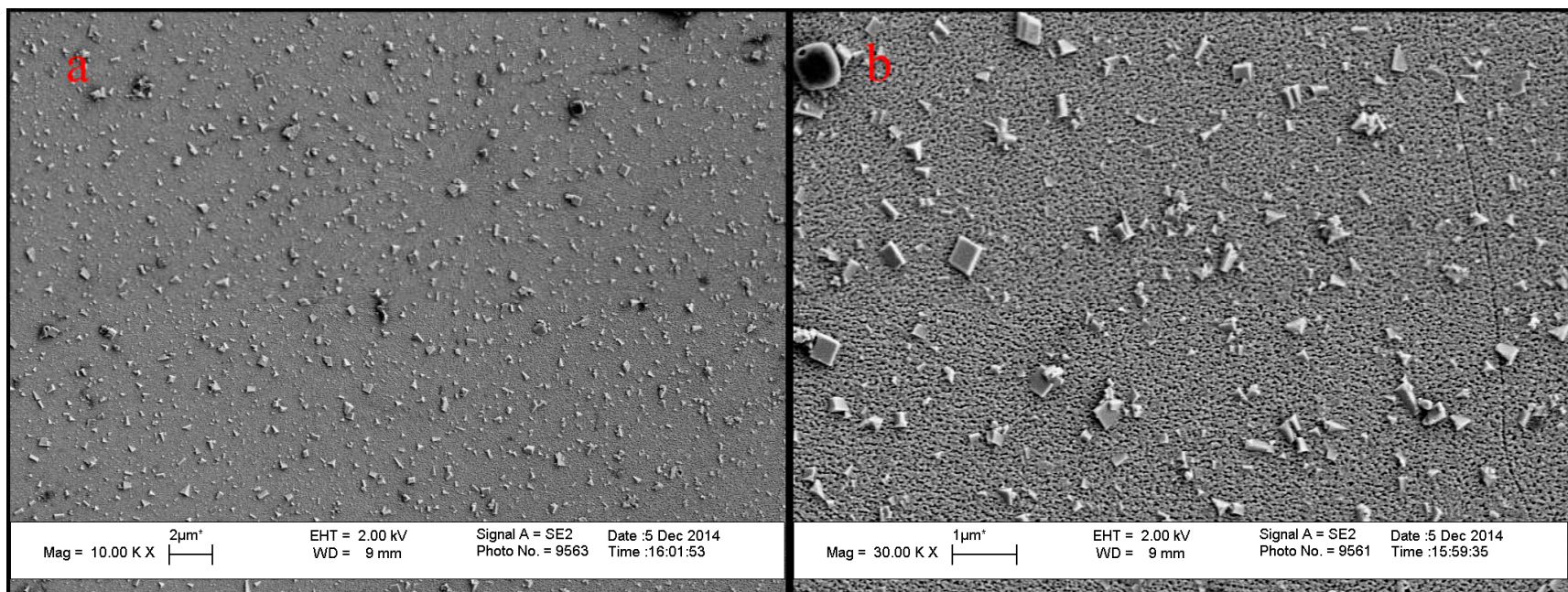


Figure 3-3: SEM image of thin-film deposited from 1M solution in different magnification a) 10kX b) 30kX.

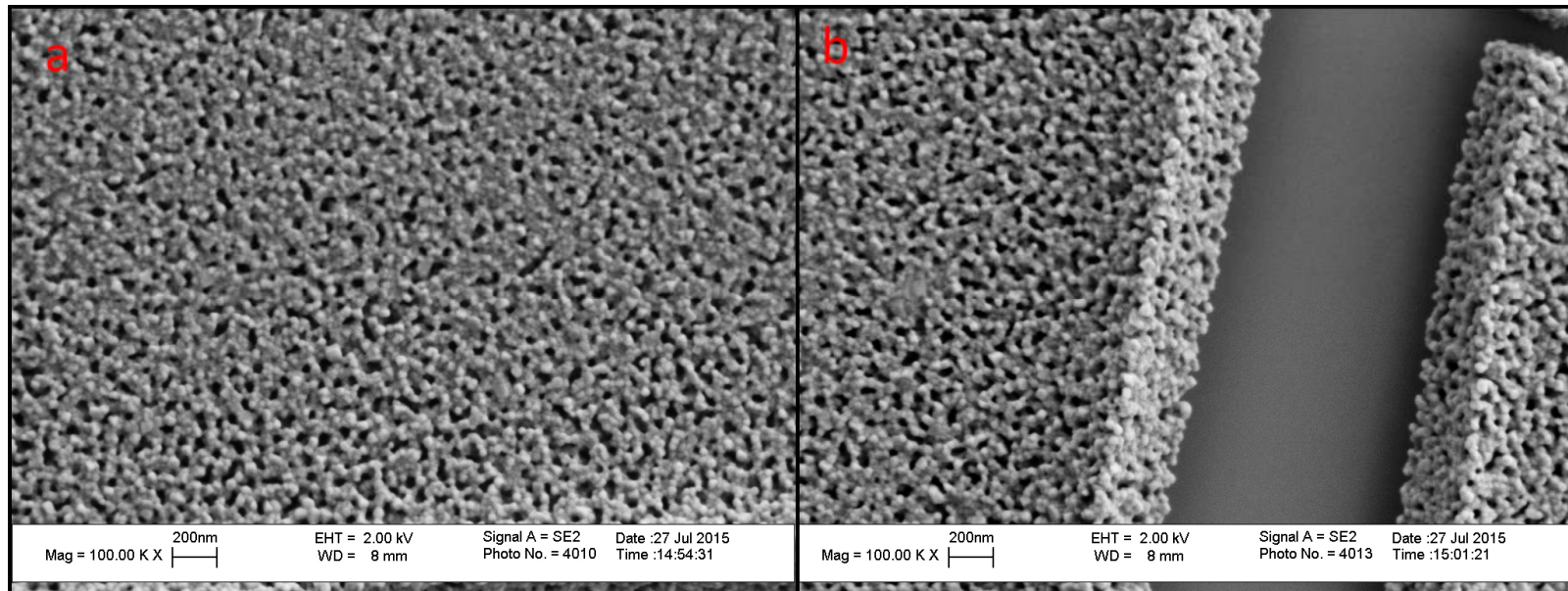


Figure 3-4: SEM results show a) surface morphology of thin film b) vertical cross section of the film.

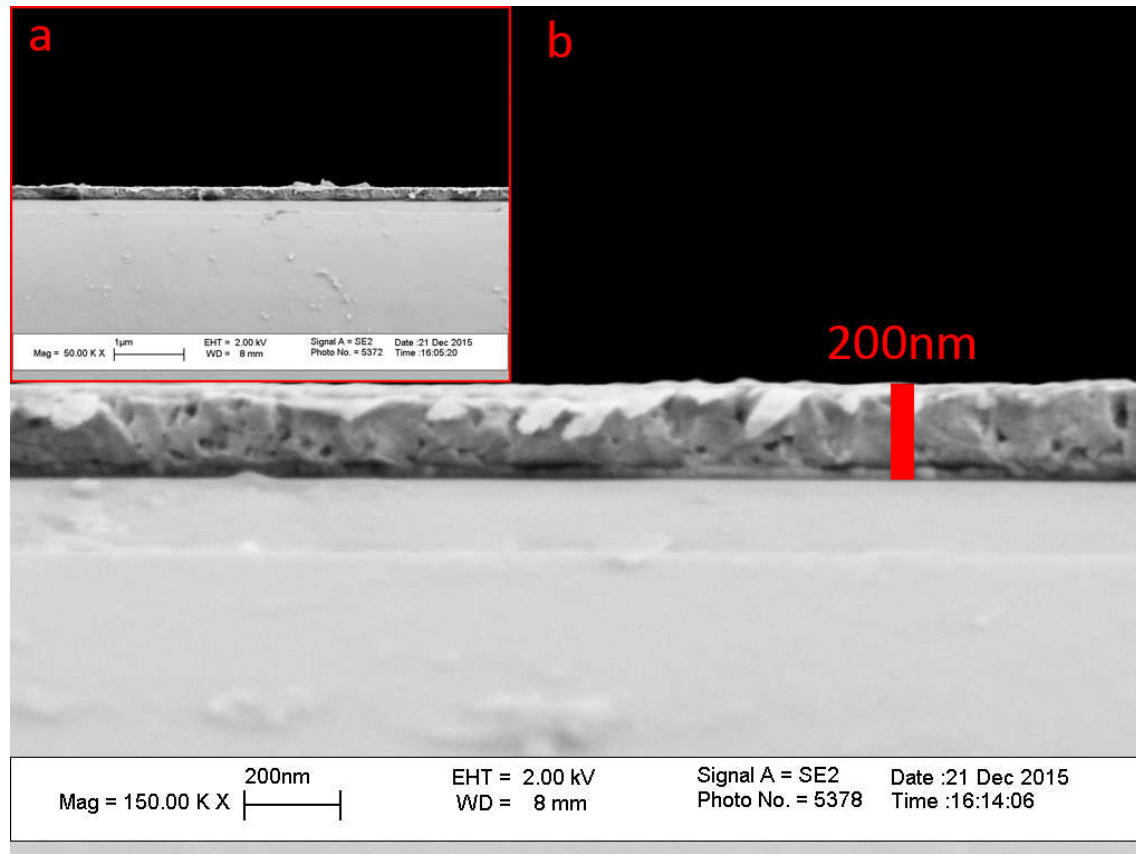


Figure 3-5: Thickness of a dense thin film in a) 50kX magnification, b) 150kX magnification after optimizing the spin coat parameters, heating rate, sintering temperature and atmosphere.

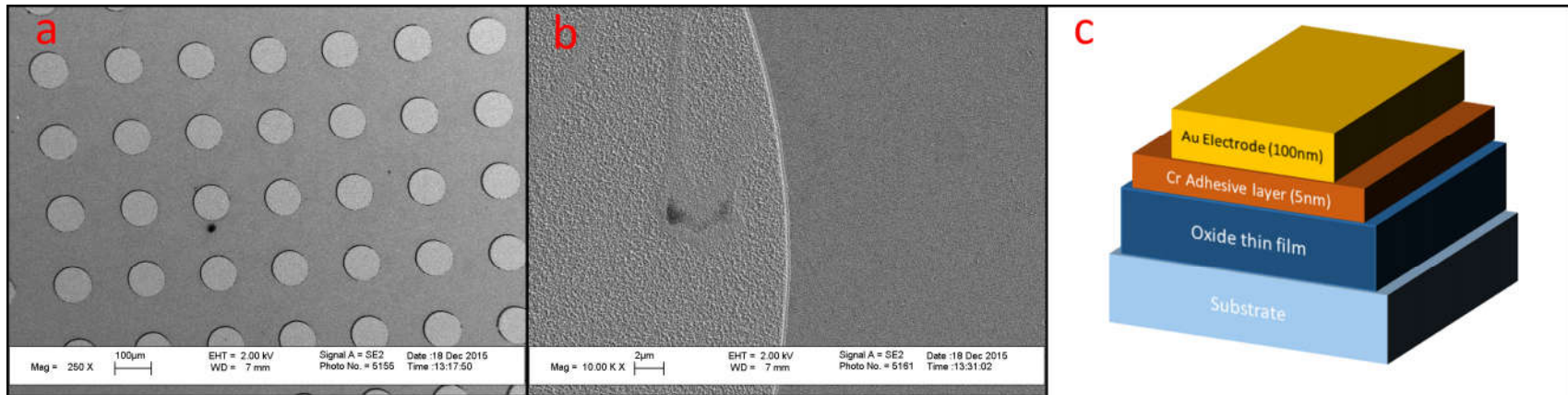


Figure 3-6:a) deposited Au electrodes on BT b) Surface morphology of Au Electrode on BTO c) Schematic illustration of the Au Electrode and film structure in presence of the a very thin Cr adhesive layer

Although the surface quality of the deposited Au electrodes was promising and no significant physical defect observed in the SEM results, the obtained I-V results for the Au electrode were not satisfying which could correlate to the presence of the Cr adhesive layer. Since the addition of the dead layer adds an extra complication to the current leakage mechanism and the first attempts to get reasonable data were not successful, in entire measurements only Pt and Cu were used as top electrode.

Figure 3-7, 3-8, 3-9 represent the surface quality of the films in two magnifications after heat treatment in O<sub>2</sub> rich environment and before depositing the electrodes. Surface of the film is nearly porous free and no extra crystallization is observed.

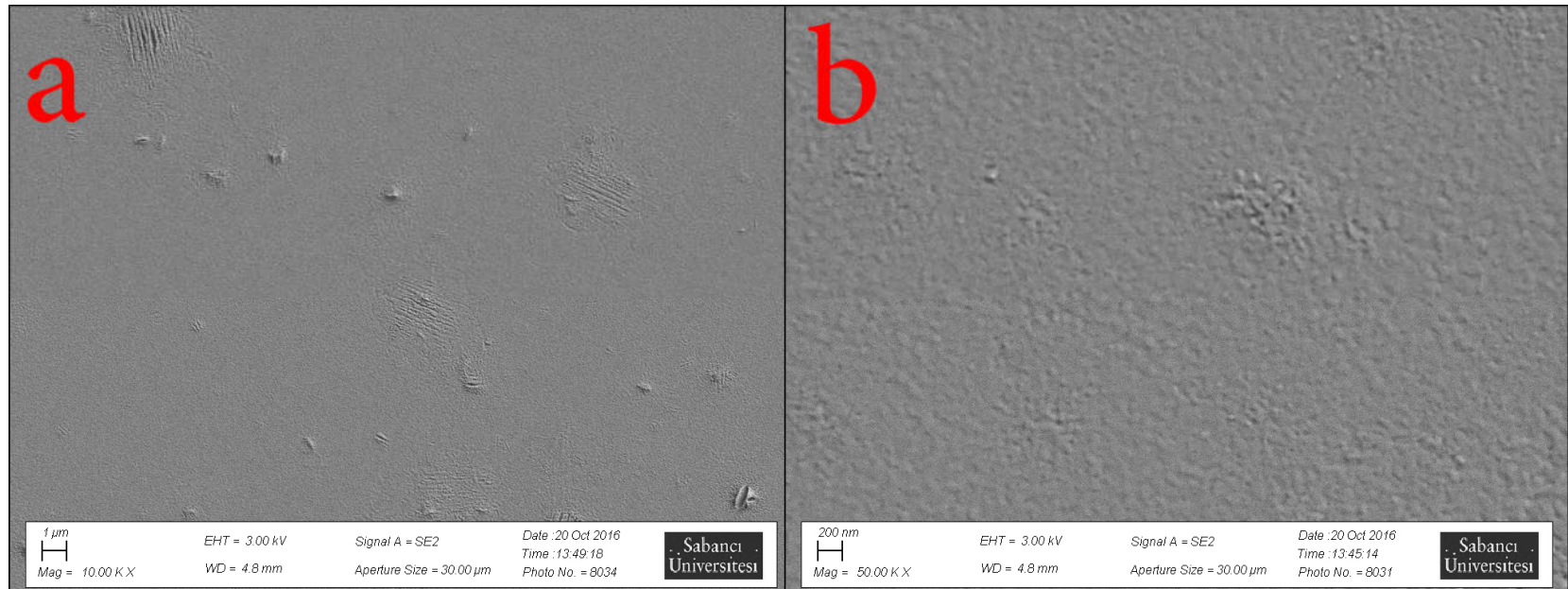


Figure 3-7: Surface of BaTiO<sub>3</sub> film in two magnifications. a)10kX b)50kX.

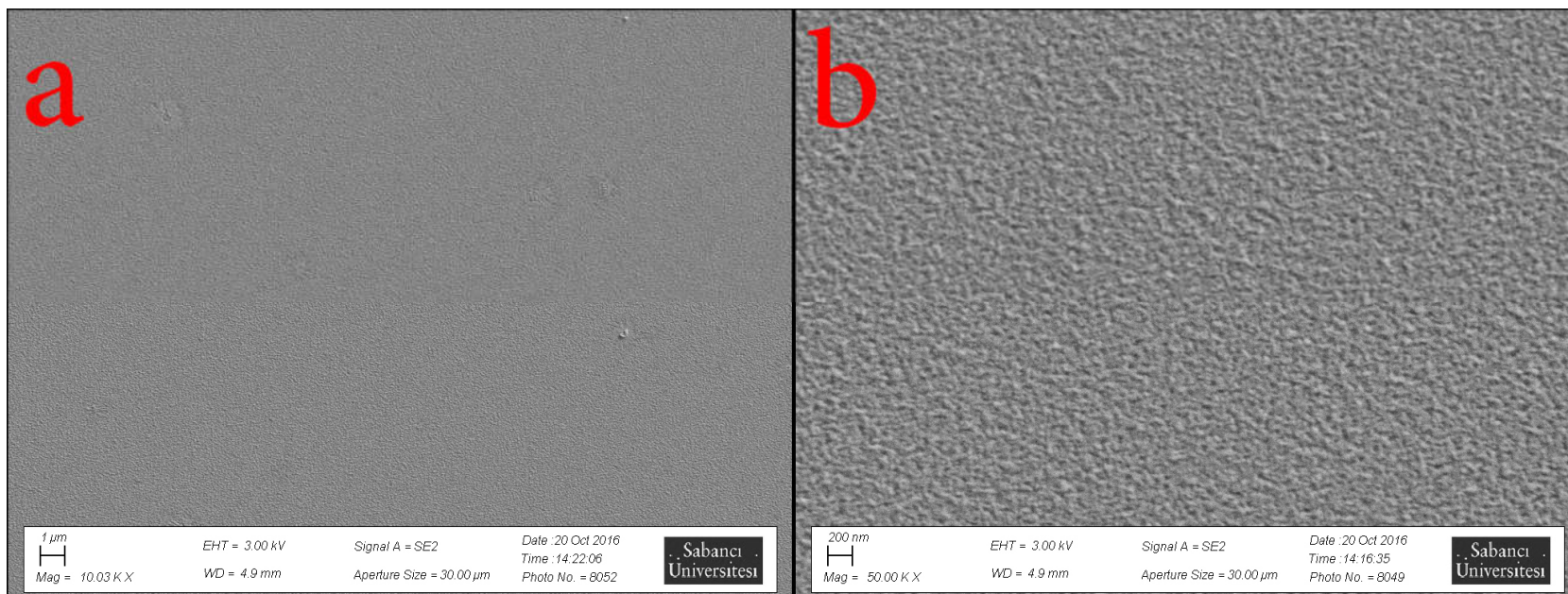


Figure 3-8: Surface of Ba<sub>0.7</sub>Sr<sub>0.3</sub>TiO<sub>3</sub> film in two magnifications. a)10kX b)50kX.

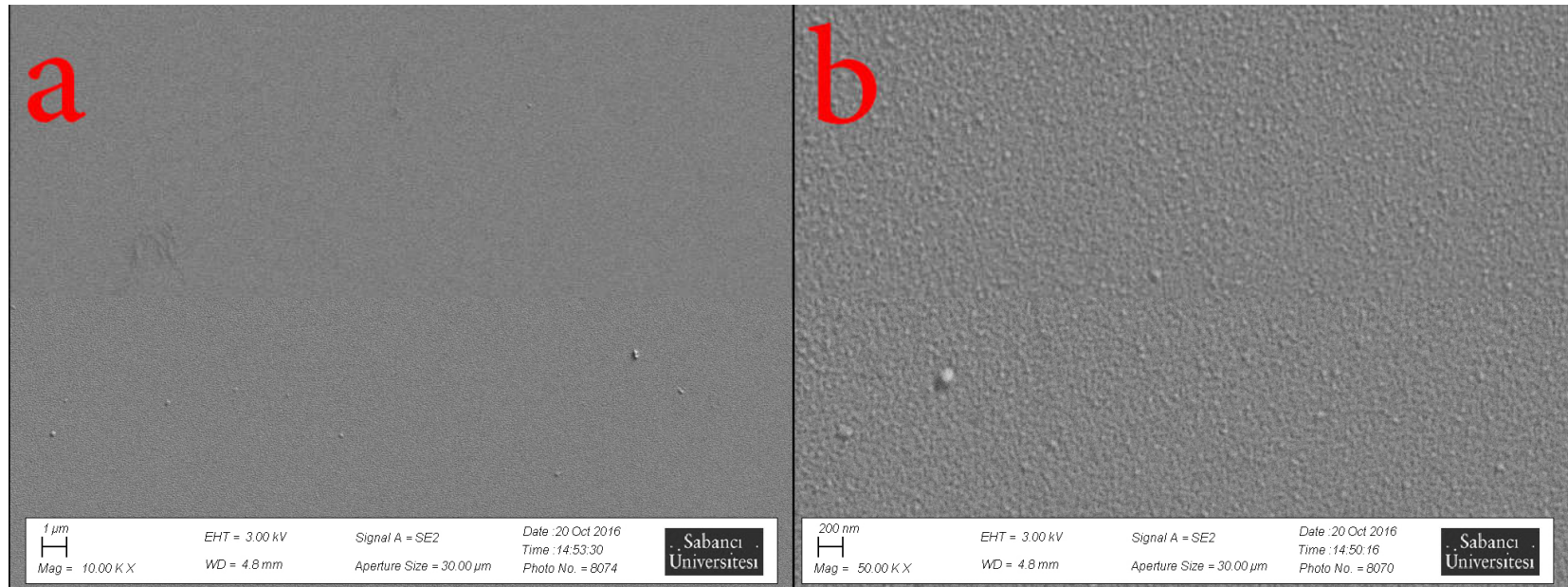


Figure 3-9: Surface of  $\text{Ba}_{0.5}\text{Sr}_{0.5}\text{TiO}_3$  film in two magnifications. a)10Kx b)50Kx.

The Platinum electrode surface quality is represented as an example in Figure 3-10. Diameter of each electrode is 100 μm and Secondary Electron mode (SE2) and InLens mode of SEM are used to inspect the deposited electrode quality. The electrodes are crack free and homogenous.

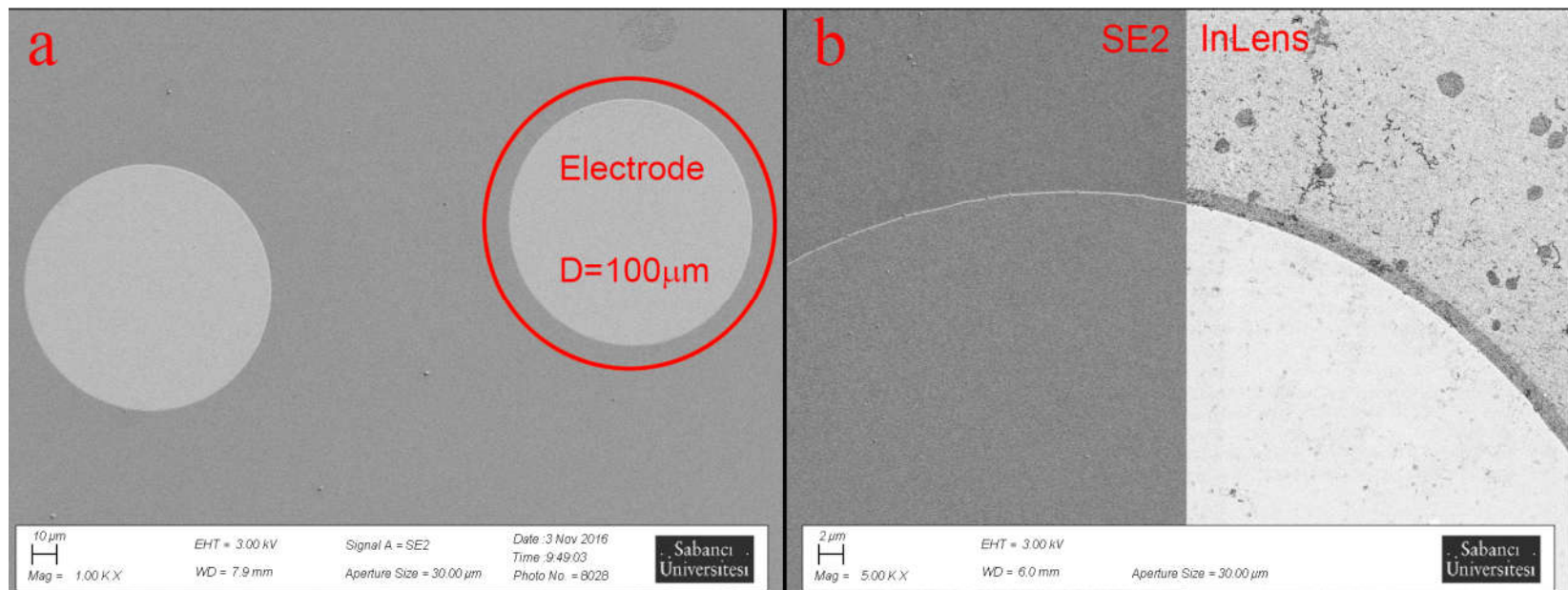


Figure 3-10: Platinum Electrode surface quality a) Diameter of each electrode is 100 μm b) SE2 and InLens images of the electrode surface.

### 3.2 Electrical characterizations

An in-house electrical measurement setup was assembled partly at Sabanci University followed by systematic measurement efforts at the National Institute of Materials Physics (NIMP) in Magurele, Romania. The equipment in Sabanci University includes a LCR meter model HIOKI IM3523, a sourcemeter model KEITHLEY 2401, a digital multimeter model Agilent 34401A and a triple output DC power supply model Agilent E3631A, a stereotyp microscope model CARL ZEISS STEMI 2000, two precise micromanipulator (Figure 3-11).

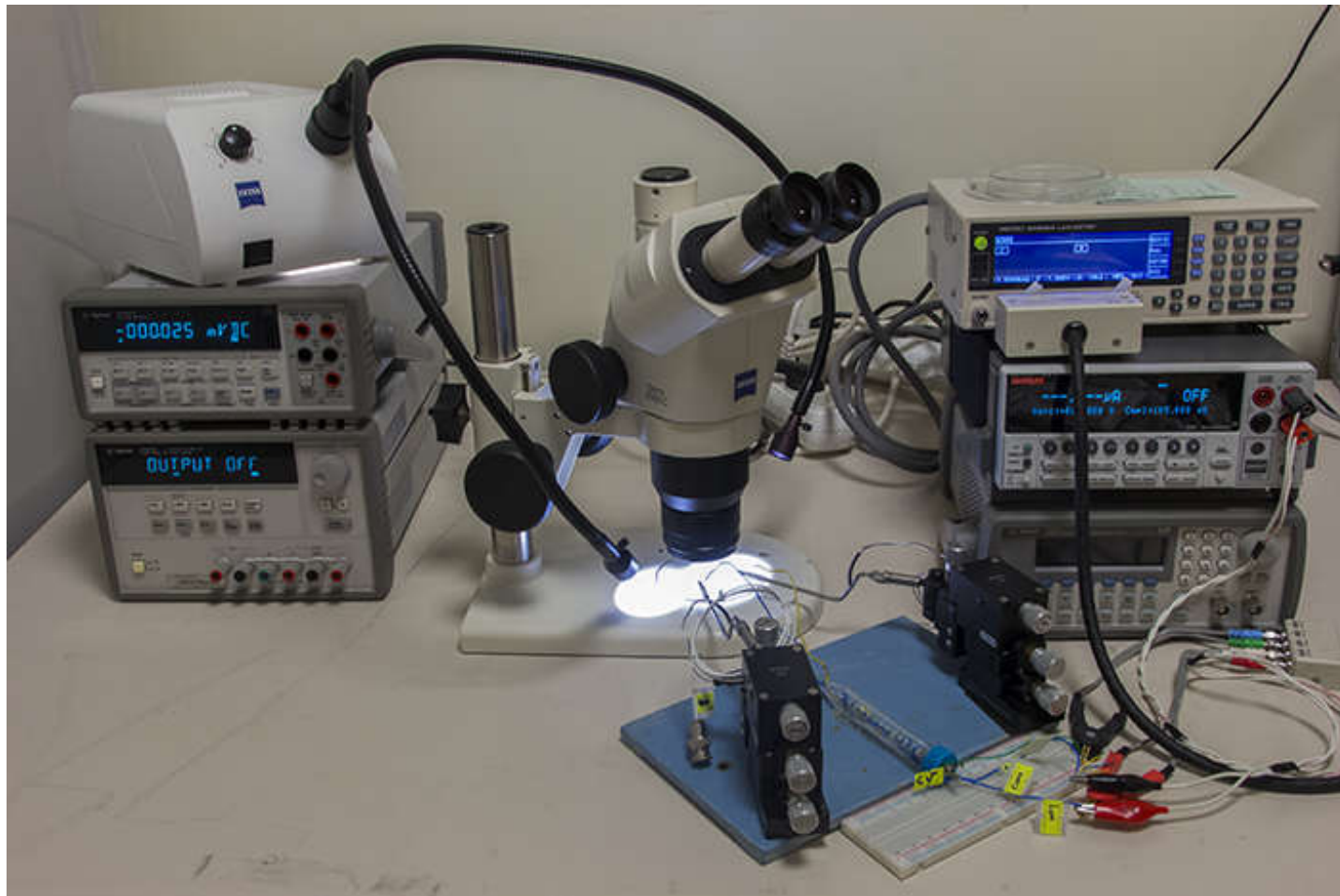


Figure 3-11:Electrical measurement setup in Sabanci University.

The equipment at NIMP includes a Lakeshore cryoprober model CPX-VF, a Keithley electrometer model 6517 (for  $I$ - $V$  characteristics), a ferroelectric tester model TF2000 from aixACCT (for hysteresis loops), and an impedance analyzer model HP 4194A for  $C$ - $V$  measurements (Figure 3-12).



Figure 3-12: Electrical measurement setup in NIMP. Magurele-Romania.

Hysteresis measurements were performed using a triangular voltage wave with 1 kHz frequency. The  $C-V$  measurements were performed using an AC small signal of 0.1 V amplitude and 100 kHz frequency.  $I-V$  measurements were performed mainly using hysteresis type measurements ( $0 \rightarrow (+V_{\max}) \rightarrow 0 \rightarrow (-V_{\max}) \rightarrow 0$ ). Sweeping down part from  $V_{\max}$  to 0 gives a reasonable estimation of the potential barriers because this part did not contain a parasitic contribution from polarization switching[91]. The electric measurements included current–voltage ( $I-V$ ) characteristics, capacitance–voltage ( $C-V$ ) and hysteresis loop ( $P-E$ ). The electrical characterization was performed in two configurations of the probes: configuration 1 and 2. In configuration 1, the DC voltage applying probe was connected to the top electrode and the substrate acted as the bottom electrode (grounded). In configuration 2, two top electrodes were connected side by side. Figure 3-13 illustrates two configurations of probes.

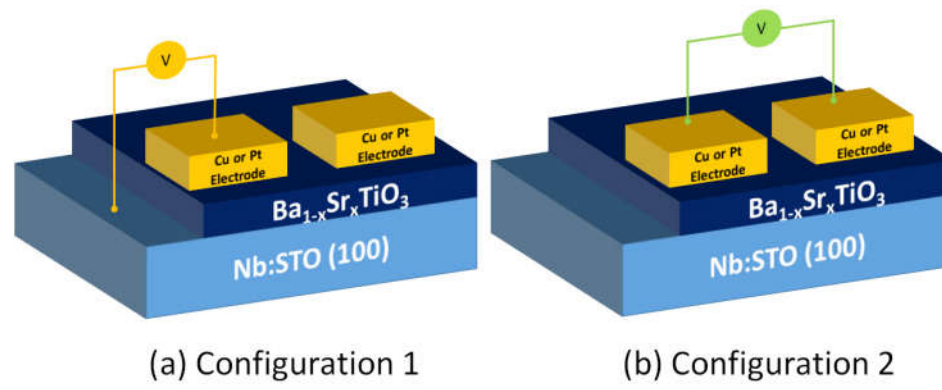


Figure 3-13: Two different configurations for probes to measure the I-V and C-V characteristics.

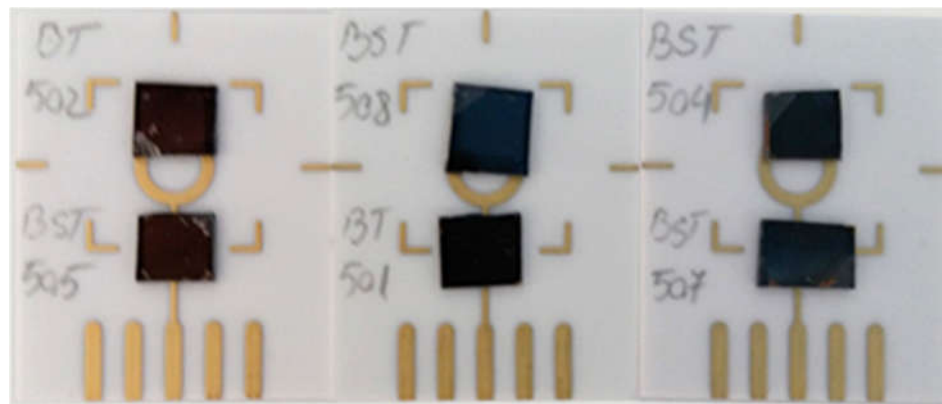


Figure 3-14: Samples assembled on the standard stage in form of configuration 1.

### 3.2.1 Current-Voltage (I-V) Characteristics

The I-V Characteristic is short for current-voltage characteristic curves of an electrical device or a component. As its name suggests, I-V characteristic curves show the relationship between the current flowing through an electronic device and the applied voltage across its terminals. According to Ohm's Law, when the voltage across the resistor increases, the current flows through it too. Constructing a graph to show the relationship between the voltage and current of the resistive elements displays a linear curve in which slope is the resistive magnitude. However, many electronic components have non-linear characteristics (I/V ratio is not constant). Semiconductor diodes can be characterized by non-linear current-voltage characteristics as the current flowing through a forward-biased. The absolute value of current in I-V measurements for three different compositions (BT, BST70, BST50) and two different probes configuration (1 and 2) in room temperature is presented in Figure 3-15, Figure 3-16, Figure 3-17, Figure 3-18 and Figure 3-19. All results show a rectifying behavior of the contacts, which indicate the diode like behavior of the Pt(Cu)-B<sub>x</sub>Sr<sub>1-x</sub>T-Nb:STO heterostructure. It means that the junction is not ohmic contact and has characteristics which can be treated as a Schottky junction. In configuration 1, bipolar resistive switching behavior in Pt-B<sub>x</sub>Sr<sub>1-x</sub>T-Nb:STO heterostructure is more obvious by hysteretic current-voltage (I-V) curve. In these graphs, for all compositions, the switching hysteresis in the positive voltage region is more notable than that in the negative region. Also, a distinguished jump is observed in positive region which can be correlated to the polarization reversal and consequent change of barrier height (BH) which will be discussed in detail in section 3.2.5. In addition, leakage current in configuration 2 for all compositions and electrode combinations are lower than that of configuration 1, because the contribution of the semiconductor bottom electrode is significantly eliminated as both electrodes are symmetrical in configuration 2. Considering the Pt electrode deposited samples (configuration 1 and 2) in Figure 3-18 (a) and Figure 3-19 (a) increasing the Sr content systematically decrease the leakage current, since Sr content decrease the polarization which leads to lower leakage current [92]. However, such noticeable trend is not observed in Cu electrode samples (configuration 1 and 2) in Figure 3-18 (b) and Figure 3-19 (b). Although the Markondeya *et al.* [93] reported that increasing the Sr content in Cu electrode samples also increases the leakage current.

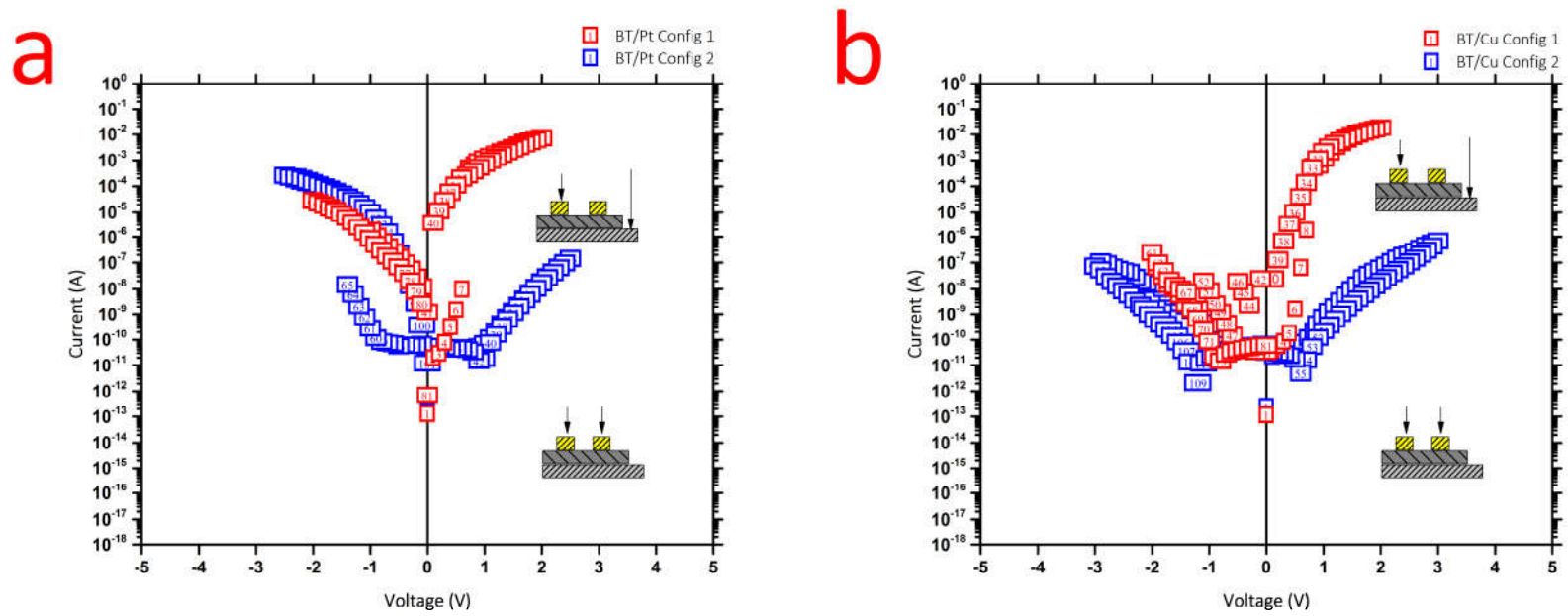


Figure 3-15: I-V measurements data of BT with a) Pt as the top electrode and b) Cu as the top electrode compared in configurations 1 and 2.

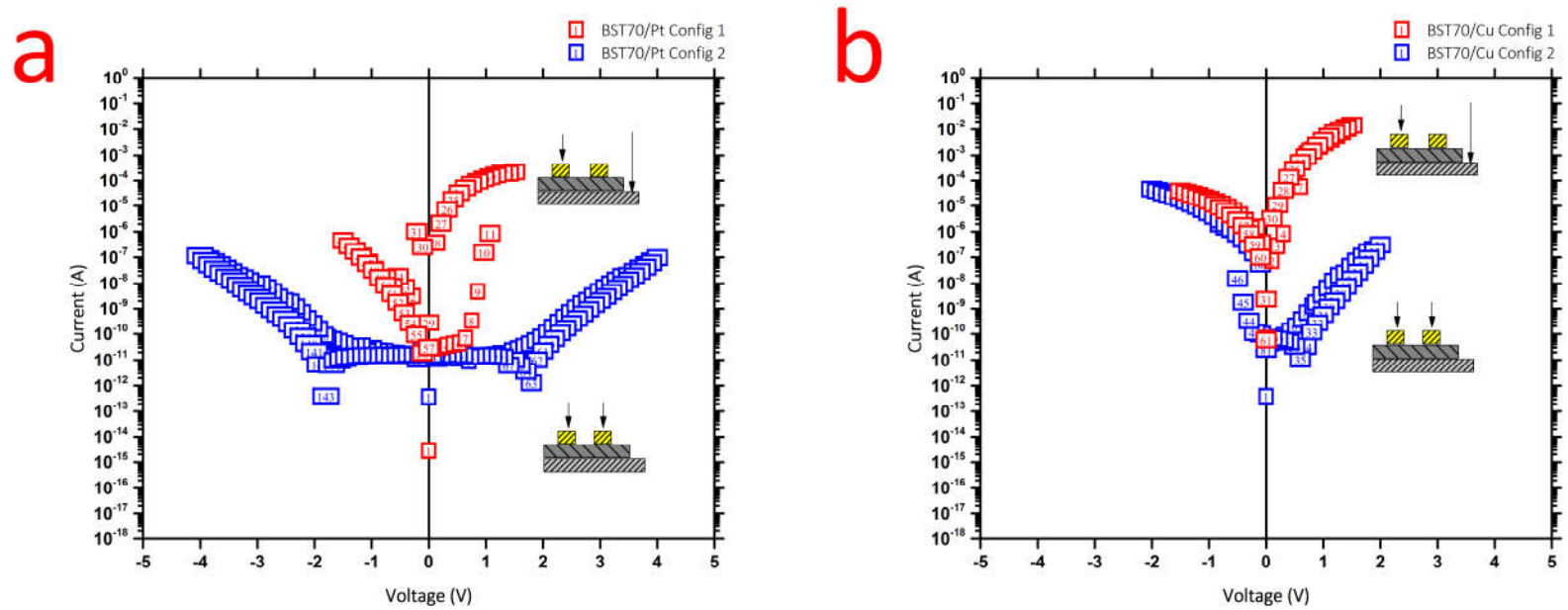


Figure 3-16: I-V measurements data of BST70 with a) Pt as the top electrode and b) Cu as the top electrode compared in configurations 1 and 2.

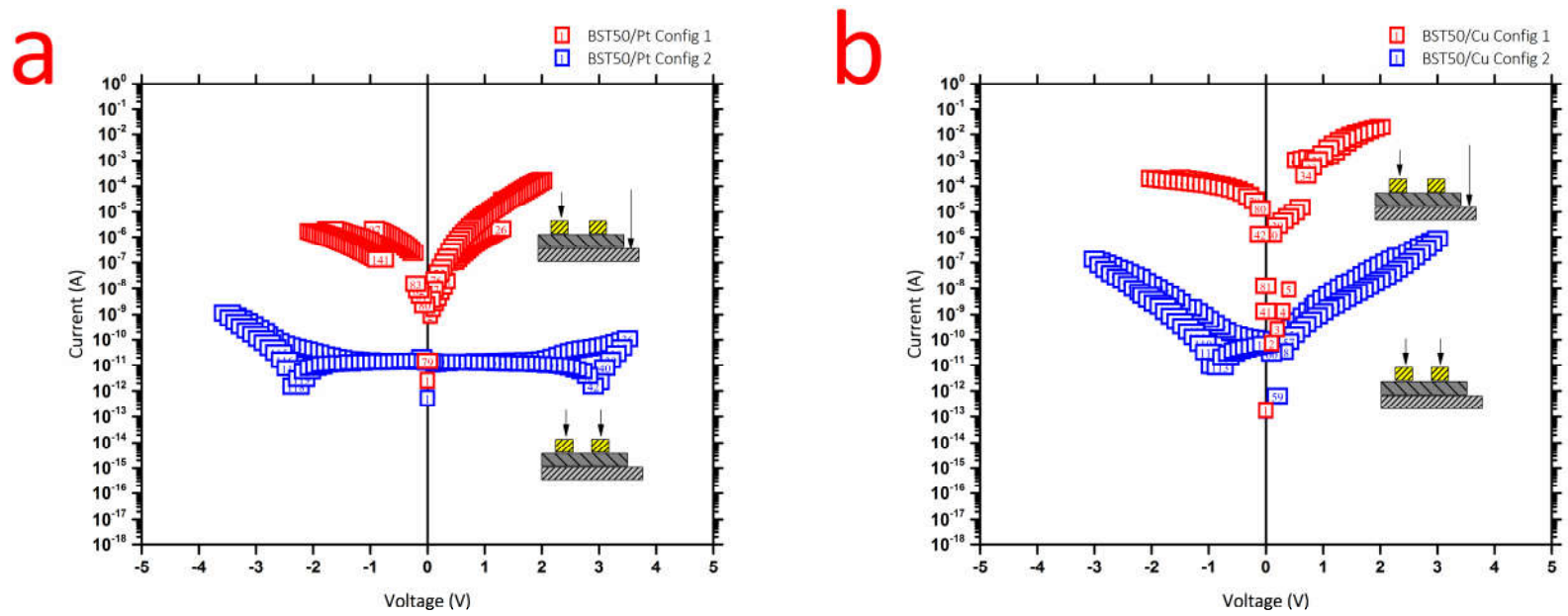


Figure 3-17: I-V measurements data of BST50 with a) Pt as the top electrode and b) Cu as the top electrode compared in configurations 1 and 2.

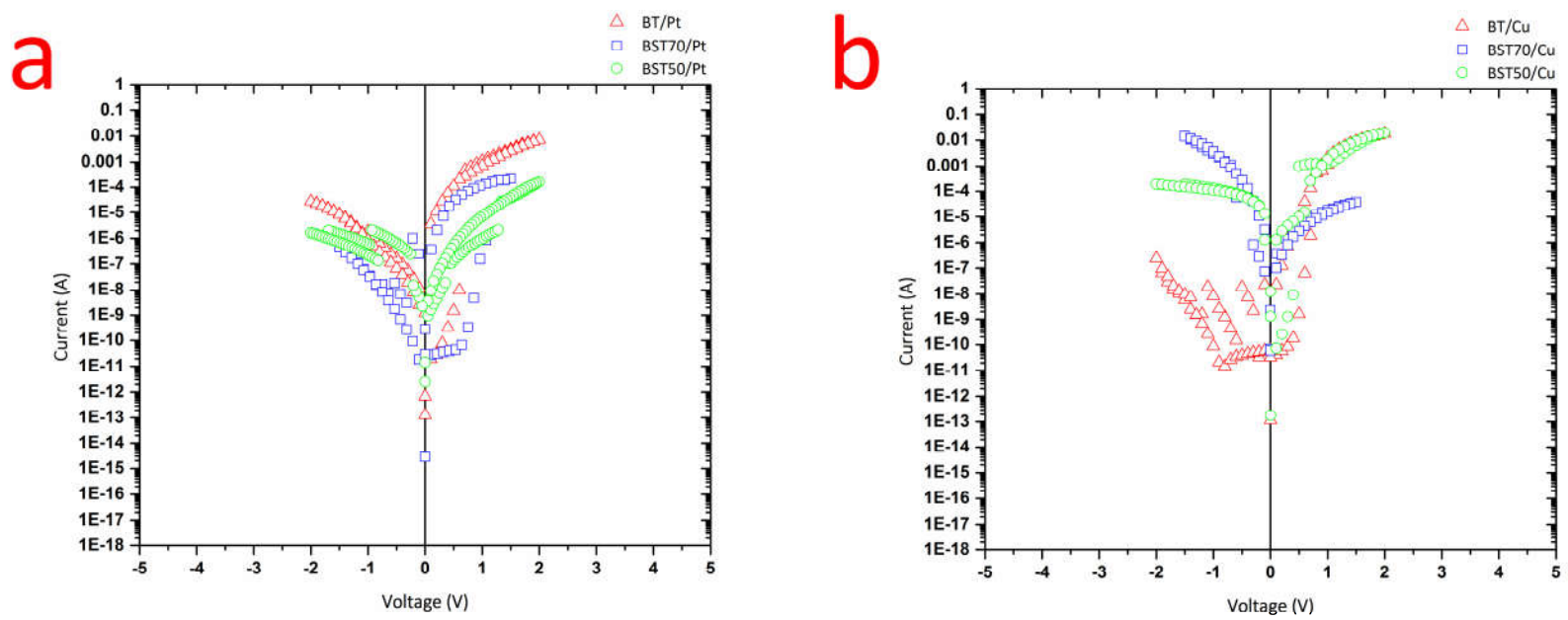


Figure 3-18: Measured I-V characteristics of all compositions in configuration 1 for both a) Pt as the top electrode b) Cu as the top electrode.

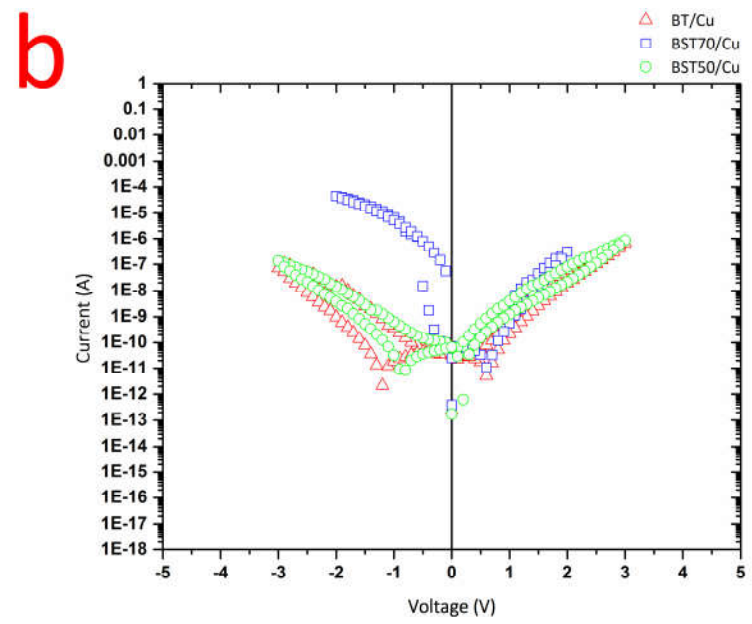
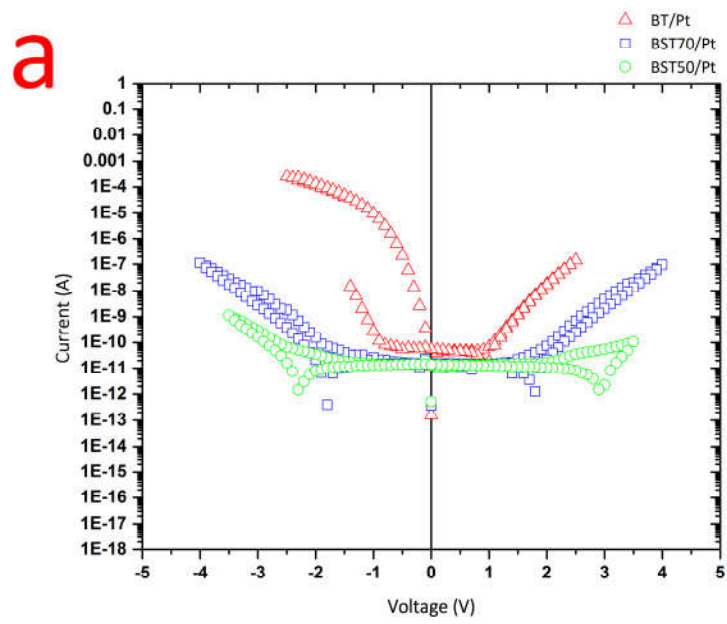


Figure 3-19: Measured I-V characteristics of all compositions in configuration 2 for both a)Pt as the top electrode b)Cu as the top electrode.

### 3.2.2 Capacitance – Voltage characteristics

To get further insight into the electrical characteristics of Pt(Cu)-Ba<sub>x</sub>Sr<sub>1-x</sub>TiNb:STO heterostructure, the capacitance–voltage (C–V) measurement carried out at frequency of 1 kHz for all samples in room temperature. In Figure 3-20, electrode configuration 2 is selected for C-V measurements of the samples in room temperature. The reason is that the I-V result for the configuration 2 revealed a lower leakage current and it means better charge storage characteristics. Also, since the aim is to get capacitance of the junction and emphasize on the polarization switching, selecting configuration 2 is rather more reasonable. Figure 3-20 and Figure 3-21 show the C–V curve with an obvious ferroelectricity behavior by negative/positive voltage. The samples with Pt as top electrode show a higher capacitance compared to Cu deposited samples. For both Pt and Cu deposited samples, BST50 shows higher capacitance compared to BT (Figure 3-20). The reason is that addition of the Sr decrease the Curie point which leads to increase in dielectric constant and capacitance. However, the effect of Sr addition and increasing capacitance cannot be correlated for BST70.

Figure 3-20: C-V measurement of the samples in room temperature (Configuration 2). Comparing the Cu and Pt electrode type on a) BaTiO<sub>3</sub> (BT) b) Ba<sub>0.7</sub>Sr<sub>0.3</sub>TiO<sub>3</sub>(BST70) c) Ba<sub>0.5</sub>Sr<sub>0.5</sub>TiO<sub>3</sub>(BST50).

Figure 3-21: C-V measurement of the samples in room temperature (Configuration 2). Comparing the effect of: a) Cu as the top electrode  
b) Pt as top the electrode on all compositions. c) Comparing all C-V measurements result.

### 3.2.3 Polarization – Electric field (P-E) Hysteresis Loop

The Polarization–Electric field hysteresis loops (P-E) and current associated with it for the BT, BST70 and BST50 samples (Pt top electrode) at room temperature (RT) are presented in Figure 3-22.

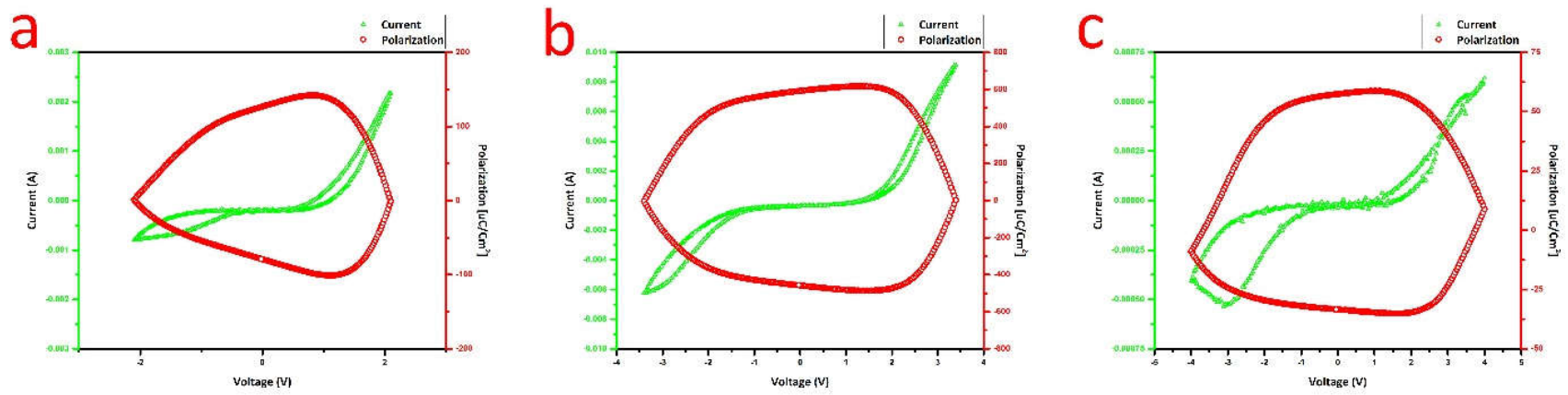


Figure 3-22: P-E hysteresis loop for Pt top electrode of a) BT b) BST70 c) BST50.

The P-E loops obtained by using a triangular voltage with a frequency of 1 kHz are presented in Figure 3-23.

Figure 3-23: Time dependent P-E hysteresis loop for Pt top electrode of a) BT b) BST70 c) BST50.

The P-E loop recorded during hysteresis measurement does not show the expected theoretical characteristics associated with polarization reversal. Before this, the trace of polarization switching is confirmed by C-V measurements. Also comparing the I-V results with computational modeling confirms the existing of the polarization switching in the samples. Hence, no further interpretation can be made from the P-E results. However, Pintilie *et al.*[94] reported an indication for the polarization switching in the hysteresis observed on the negative side of the I-V characteristic during polarization hysteresis measurement without trace of switching in positive bias.

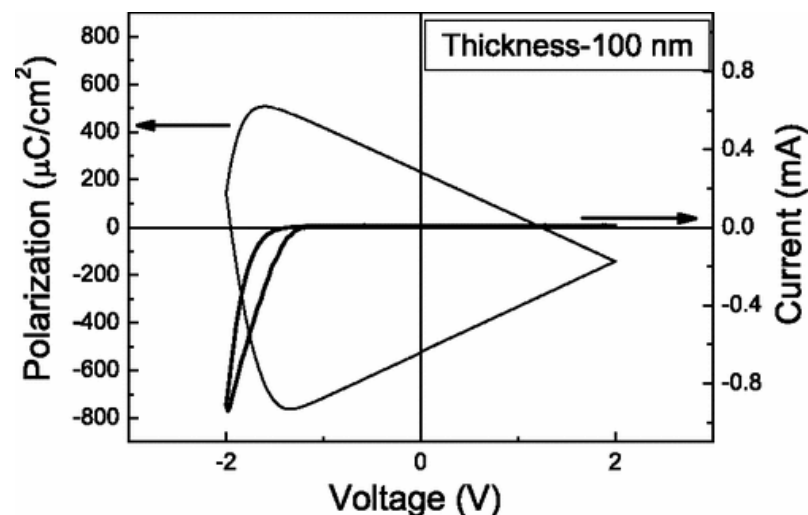


Figure 3-24: Hysteresis loops for SRO-PZT-Ta structures with 100 nm thickness of the PZT layer [94].

They claim that the switching peaks might be hidden by the large leakage current obtained for the negative bias polarity. However, I-V characteristic presents a strong rectifying behavior very similar to a Schottky diode in negative bias (Figure 3-24). In this method, by applying bias in  $0 \rightarrow -V_{\max}$  current measurement contain not only the switching of polarization contribution, but also other contributions such as leakage current and dielectric displacement. By applying a pulse of the same amplitude and same polarity after the previous one ( $0 \rightarrow -V_{\max}$ ), the second measurement contain back switched dipole contribution in addition to the leakage contribution and dielectric displacement. In consequence, the difference between the polarization measured after first pulse and second pulse will be the remnant polarization. This is a plausible method to obtain the value of real polarization at 0 electric field or saturated polarization. Hence, the same method is applied on the Pt electrode deposited samples and the results are presented in Figure 3-25. The polarization is decreased in BT and BST50 by addition of Sr which was already expected. The remnant polarization in BT and BST50 are 2 and 44  $\mu\text{C}/\text{cm}^2$  respectively. The magnitude of the polarization in BST70 is extremely high for such composition and compared to BT and BST50. This can only be the sign of high current leakage in this sample. In this thesis, the presence of polarization switching is confirmed with the C-V result and remnant polarization results obtained by mentioned method.

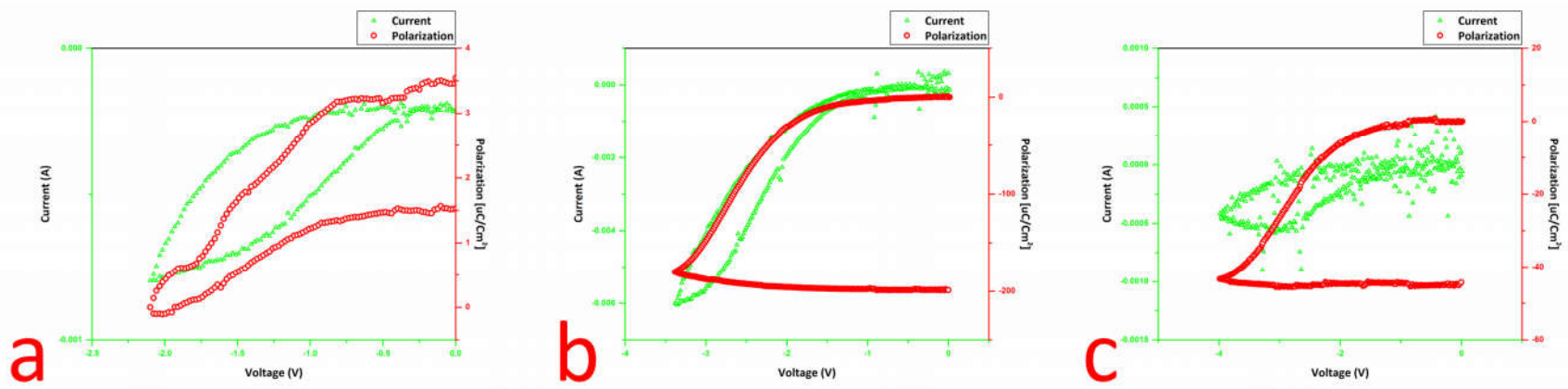


Figure 3-25: Remnant polarization indication in Pt deposited electrode on a) BT b) BST70 c)BST50.

### 3.2.4 Computational Modeling Results

The results of the numerical computation for the system of interest in this thesis are used to shed light especially on the I-V behavior of our samples where we did see indications of the RS phenomena. The schematic of the system analyzed has already been provided in Figure 1-15. The thermodynamic model coupled with the universal equations of electrostatics and equations of semiconductors allow us to obtain results without any apriori assumptions that is the case with several other works. The most important result we obtain is that the semiconductor Nb:SrTiO<sub>3</sub> electrode can take on one the two states at the FE interface depending on the direction of polarization: Either a carrier accumulated or a carrier depleted state. The two states provide different mechanisms of screening to polarization charges that is the basis of resistive switching. Here the result of the computational study presented in four graphs. In these graphs, polarization along the Z axis, carrier (electrons) distribution map, ionized donor distribution map and energy band diagram is presented. The detail information about the computational method is provided in the section 1.4.4. As it is observable from Table 4, even at zero bias interface of the BT and Nb:STO produce a junction which can be assumed as a Schottky junction. Applying +1V and -1V bias leads to the conduction, since the conduction band penetrates to the Fermi level. The result of the data is directly correlated to the RS behavior and discussed in detail in section 3.2.5.

Table 4: Computational simulation results for BT in three different bias applied in top electrode.

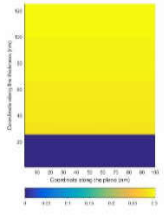
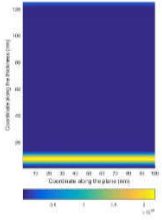
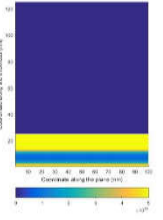
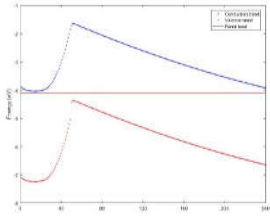
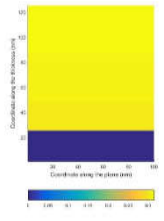
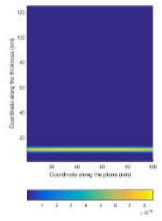
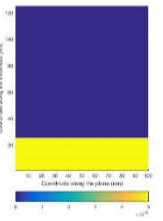
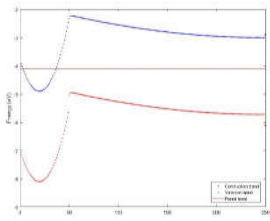
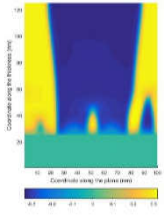
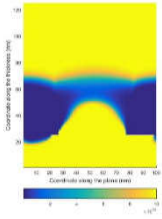
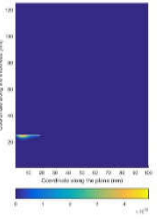
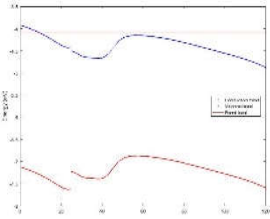
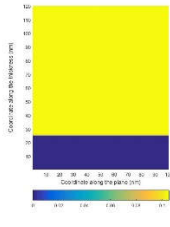
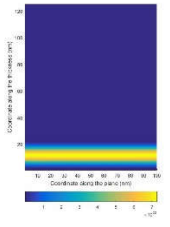
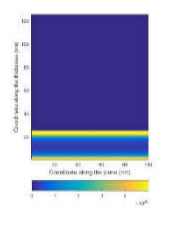
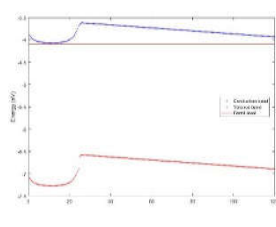
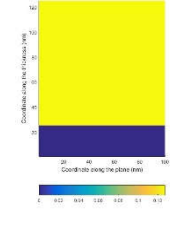
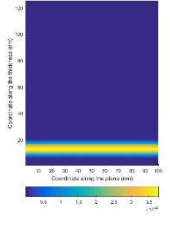
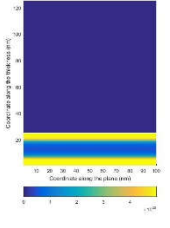
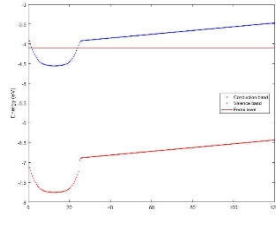
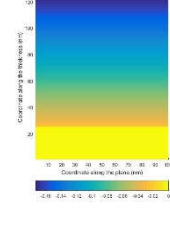
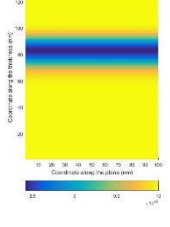
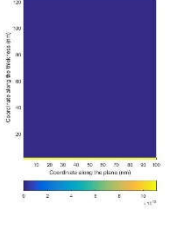
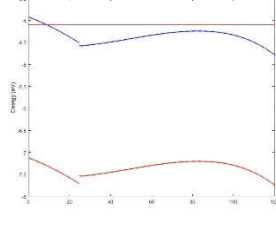
| BT          |   |  |   |   |
|-------------|---|--|---|---|
| Voltage (v) | Polarization along Z axis   | carries (Electron) map   | Ionized donors distribution map   | Energy band diagram   |
| 0           |    |    |    |    |
| -1          |   |   |   |   |
| +1          |  |  |  |  |

Table 5: Computational simulation results for BST50 in three different bias applied in top electrode.

| BST50       |   |  |   |   |
|-------------|---|--|---|---|
| Voltage (v) | Polarization along Z axis   | carries (Electron) map   | Ionized donors distribution map   | Energy band diagram   |
| 0           |    |    |    |    |
| -1          |    |    |    |    |
| +1          |  |  |  |  |

Here, only the results of BT and BST50 are presented. The BST70 experimental results were not satisfactory compared to BT and BST50. Hence, we weren't able to correlate a scientific explanation between computational and experimental studies.

The penetration of conduction band to Fermi level in BT (+1V bias) is much abrupt compared to the one in BST50. It is because of the fact that in BT the polarization switching is not fully satisfied (consider PZF) and band bending is much more significant. This significant band bending in BT means that it has more electron accumulation in the interface therefore we expect higher amount of leakage current. In this model, due to the polarization, the charge accumulation in BT is much more higher compared to the one in BST50 in which we have smoother band bending. This is consistent with the experimental results. It is worth to note that, the change in leakage current in the experimental study is not higher than one order of magnitude between BT and BST50. However, as mentioned earlier, this model is an ideal thermodynamic model which was only proposed to clarify some facts about ferroelectric polarization state and corresponding mechanism proposed in this thesis. In addition, this computational study confirms the experimental study results and explains the band bending, carrier accumulation and depletion which only semi qualitatively explains the proposed mechanism. The misfit in our computational study is 1% which is a well-accepted value for such systems which in real life might be higher value.

### 3.2.5 Resistive Switching

The Figure 3-26 is presented here as an example of resistive switching and in purpose of discussing the mechanism. The following I-V curve is obtained from hysteresis loop and is a dynamic measurement which whole measurement is done in 1s. However, in the regular I-V curve (Figure 3-27) with changing the DC bias the measurement is quasi static with 0.5s step size. In Figure 3-27a clear jump in current is observable near the polarization switching point.

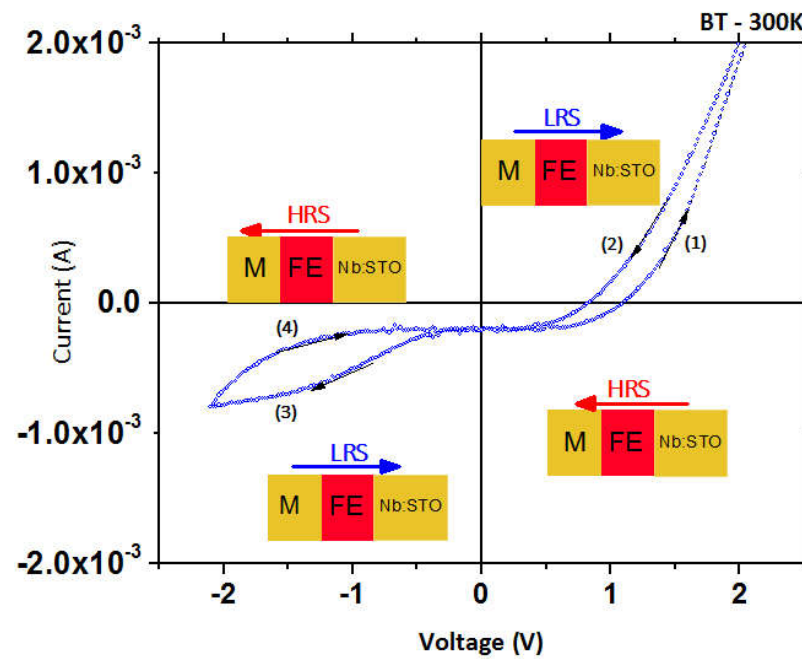


Figure 3-26: I-V curve corresponding to Pt-B<sub>x</sub>S<sub>1-x</sub>T-Nb:STO heterostructure indicating the direction of the polarization and resistive states.

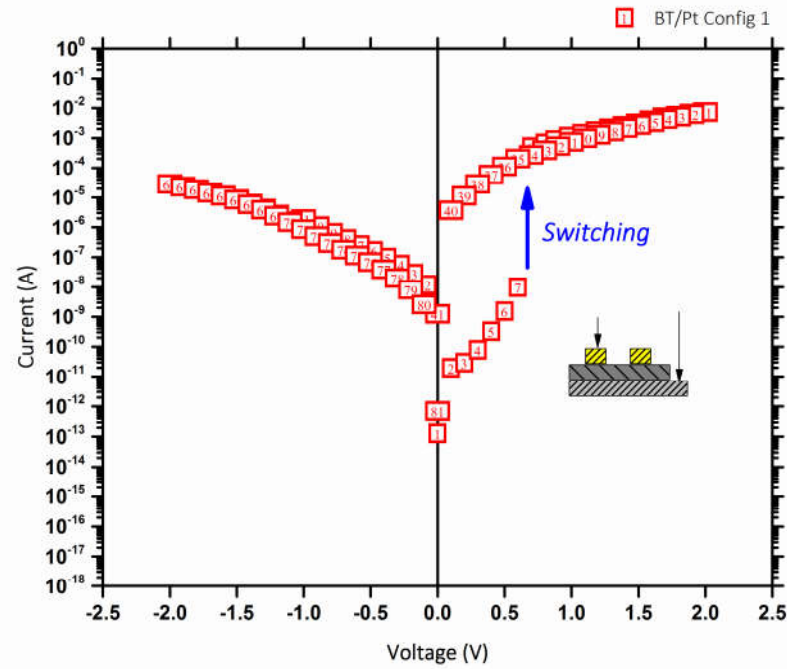


Figure 3-27: Regular I-V curve corresponding to Pt-B<sub>x</sub>S<sub>1-x</sub>T-Nb:STO heterostructure measured in configuration 1.

From Figure 3-26 it is noticeable that the resistive state of the Pt-B<sub>x</sub>S<sub>1-x</sub>T-Nb:STO heterostructure changes either with increasing positive bias or negative bias which is opposite to reported studies for ferroelectric tunnel junctions [95], [96]. It seems the ferroelectric interface junction is more dominant than ferroelectric tunneling effect which is reported for the Pt-B<sub>x</sub>S<sub>1-x</sub>T-Nb:STO heterostructure [97]. It seems the current in  $0 \rightarrow +V_{\max}$  (or  $-V_{\max} \rightarrow 0$ ) is lower than  $-V_{\max} \rightarrow 0$  (or  $0 \rightarrow +V_{\max}$ ) which may correspond to the high resistive and low resistive respectively. It can be correlated to the resistive switching in Pt-B<sub>x</sub>S<sub>1-x</sub>T-Nb:STO heterostructure [81], [98], [99]. In order to investigate the RS [100]–[102] it has to be taken into account that a Schottky barrier can form at the interface between the electrode and semiconducting ferroelectric oxide (in this case: Ba<sub>x</sub>Sr<sub>1-x</sub>TiO<sub>3</sub>). The profile of the Schottky barrier can be altered by reversing the polarization direction. Based on computational study results, the ferroelectric polarization could be the responsible for the different resistive states.

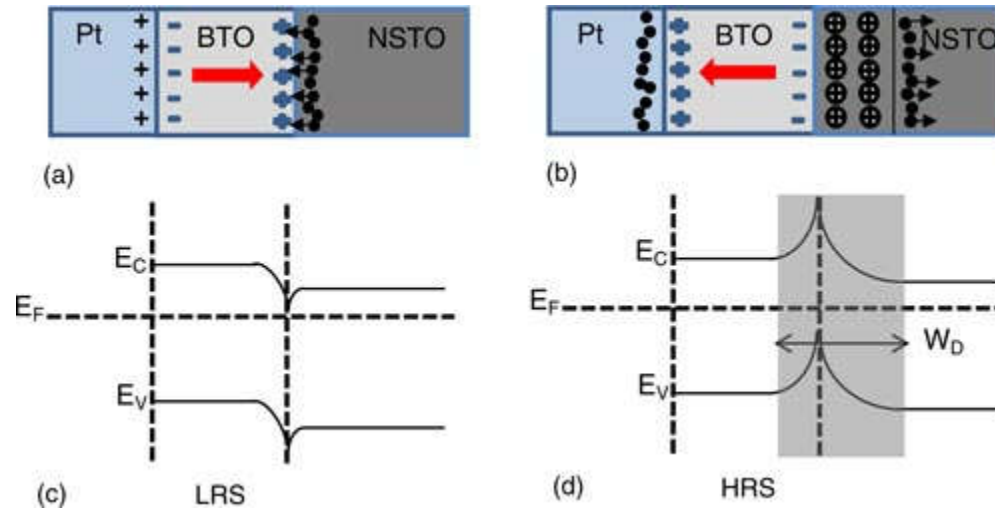


Figure 3-28: Schematic charge distribution and (c), (d) corresponding energy-band diagrams at LRS and HRS, respectively. In the BTO layer, the red arrows denote the polarization directions and the large 'plus' and 'minus' symbols represent positive and negative ferroelectric bound charges, respectively. The 'plus' and 'dot' symbols in the Pt and NSTO represent holes and electrons, respectively. The 'circled plus' symbols represent ionized donors [103].

As illustrated schematically in Figure 3-28, when the polarization is pointed to the semiconductor, positive bound charges accumulate at the  $\text{Ba}_x\text{Sr}_{1-x}\text{TiO}_3\text{-Nb:STO}$  interface and negative carriers (electrons) in Nb:STO (considered n-type SC) are attracted to the positive bound charges which makes the Nb:STO interface accumulated. In addition, the screening of negative bound charges is incomplete and a depolarizing field opposite to the polarization at the interface of the FE lowers the barrier height (BH) and hence leads to the band bending at the interface (Figure 3-28)[104]. This result is in agreement with our computational results presented in Figure 3-29 obtained by the thermodynamic simulations (For the methodology, see Section 1.4.4). Due to that band bending and lower BH at  $\text{Ba}_x\text{Sr}_{1-x}\text{TiO}_3\text{-Nb:STO}$ , the carriers can easily pass through the region which is under influence of the electric field. As a result, the current pass in low resistive state (LRS).

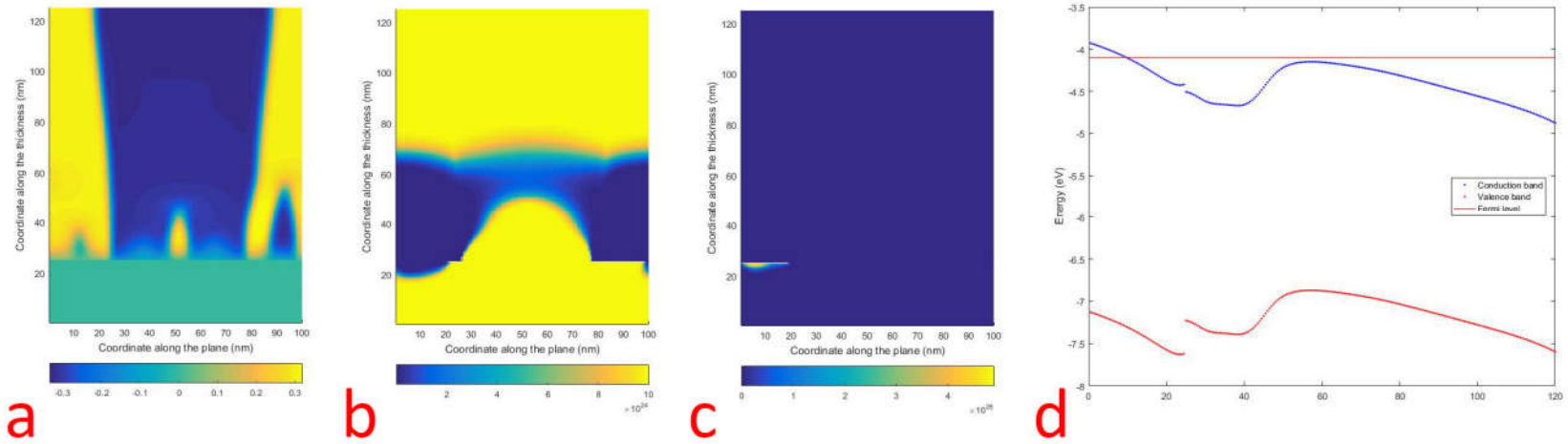


Figure 3-29: Result of the computational study in applying +1V bias to the top electrode BT a) Polarization along Z axis b) carriers (Electron) map c) Ionized donor distribution map d) energy band diagram in the midsection of the film along the thickness.

On the other hand, when the polarization is pointing to the metal electrode (Pt), the negative carriers (electrons) in Nb:STO (n-type SC) are repelled by the negative bound charges at  $Ba_xSr_{1-x}TiO_3$ -Nb:STO and immobile screening charges (Ionized donors) spread over a space charge region (depletion state) depending on the doping profile. Incomplete screening produces a depolarizing field and increases the BH (Figure 3-30). Consequently, the space charge region and BH will increase when increasing the polarization which leads to the high resistive state (HRS).

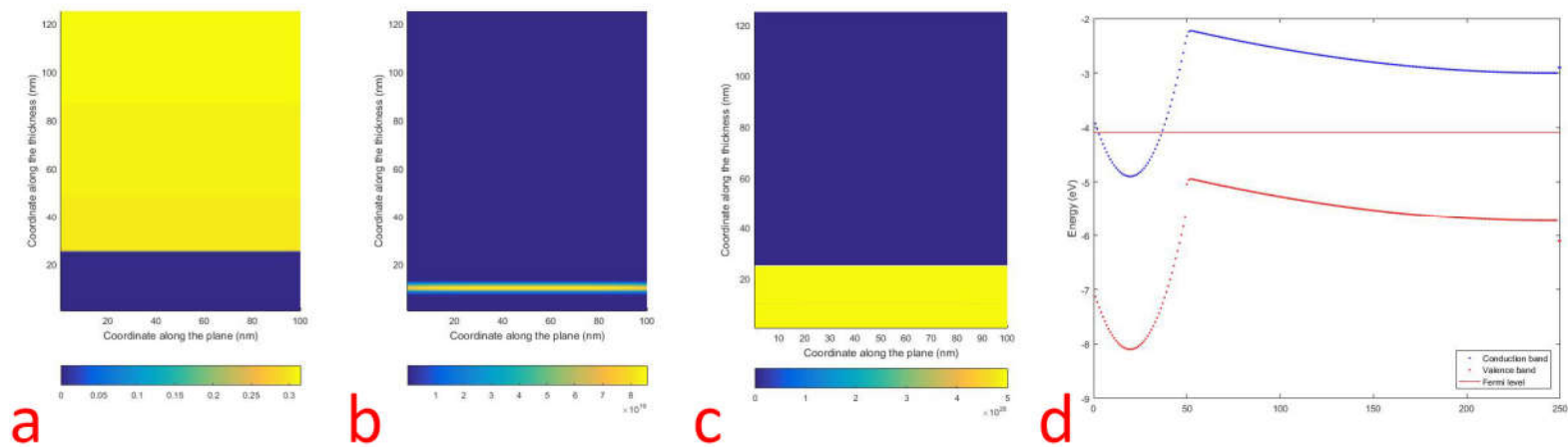


Figure 3-30: Result of the computational study in applying -1V bias to the top electrode a) Polarization along Z axis b) carriers (Electron) map c) Ionized donor distribution map d) energy band diagram in the midsection of the film along the thickness..

In theory, starting from 0 bias and moving either to  $+V_{max}$  or  $-V_{max}$  does not change the RS effect and in both cases one shall see the RS. In this thesis, all measurements are kept constant profile form  $0 \rightarrow +V_{max} \rightarrow 0 \rightarrow -V_{max} \rightarrow 0$ . The same mechanism is valid for the case of BST50 and correlation between computational studies and experimental is the same. However, the difference is the Sr content which

affects the polarization and thus the resistive switching, in which increasing the Sr content, decrease the polarization magnitude [105]. Based on the regular I-V results, the resistive switching magnitudes in BT and BST50 (Pt electrode, configuration 1) are very close to each other in which the magnitude in BST50 is one order of magnitude higher. The tricky point to interpret the computational data is that the applied voltage abruptly changes from +1V to -1V, and the assumption is that the system is in equilibrium in either applied biases. In other words, from +1V to -1V, system fully changes its polarization state. In such thermodynamical model,  $\pm 1V$  are the only boundary conditions to change the polarization and consequently change in the electron distribution and ionized donor states near the interface. By means of this, we correlate the computational results to the mechanism we proposed for the resistive switching which is the effect of the polarization change on the barrier height (BH) and consequently charge flow in the system.

## Chapter 4: CONCLUSION

Ferroelectricity is a property of materials that possess spontaneous electric polarization. It is due to the presence of electric dipoles and applying external electric field changes the polarization. Barium Strontium Titanate (BST) in different compositions ( $\text{Ba}_x\text{Sr}_{1-x}\text{TiO}_3$ ) compared to  $\text{BaTiO}_3$  which is a solid solution of Barium Titanate ( $\text{BaTiO}_3$ ) and Strontium Titanate ( $\text{SrTiO}_3$ ) and can be formed in an entire range of  $x$  ( $x=0,0.3,0.5$ ). The ferroelectric transition temperature is nearly a linear function of Ba/Sr ratio. Adding Sr into BTO structure causes the paraelectric to ferroelectric transition temperature  $T_c$  decrease linearly (30% of STO) and the transition happens near the room temperatures.

The topic of this thesis forms a part of TUBITAK 1001 COST project no 113M792. The main motivation of this project is to address the combined effect of strontium content and electrode type on electrical properties of  $\text{Ba}_x\text{Sr}_{1-x}\text{TiO}_3$  thin-films.

For preparing the barium strontium titanate ( $\text{Ba}_x\text{Sr}_{1-x}\text{TiO}_3$ ) solution, the sol-gel method and for depositing homogenous films, the spin coating technique were used. Parameters of the spin coating were optimized in order to get homogenous thin films. Heat treatment of the films required slow rate of heating in an oxygen rich environment. In order to inspect the thin films quality, SEM characterization is crucial. Here, some key parameters were optimized based on the SEM results.

The I-V measurement is an important technique to obtain valuable information about the electrical characteristics of the Metal-ferroelectric metal interfaces. This includes the leakage current. In this thesis, for measuring the I-V characteristics two probe configurations were used. Leakage current in configuration 2 for all compositions and electrode combinations were lower than that of configuration 1, because the contribution of the semiconductor bottom electrode was significantly eliminated as both of the electrodes were symmetrical in configuration 2. Furthermore, effect of the two metallic top electrodes was investigated. Considering the Pt electrode deposited samples (configuration 1 and 2) increasing the Sr content systematically decreased the leakage current, since Sr content decreased the polarization which led to lower leakage current. However, such noticeable trend was not observed in Cu electrode samples (configuration 1 and 2).

As we expected, C-V measurements were very useful tool to indicate the polarization. The butterfly shape in C-V measurements was found to be a sign of polarization. The samples with Pt as top electrode showed a higher capacitance compared to Cu deposited samples. For both Pt and Cu deposited samples, BST50 showed higher capacitance compared to BT. The reason for that was the addition of Sr decreasing the Curie point which led to an increase in dielectric constant and capacitance. However, the effect of Sr addition and increase in capacitance could not be explained for BST70.

Furthermore, we developed the thermodynamic theory for a given  $\text{Ba}_{1-x}\text{Sr}_x\text{TiO}_3$  composition using the phenomenological coefficients of  $\text{BaTiO}_3$  and  $\text{SrTiO}_3$ . By changing the boundary conditions, we showed a change in polarization states, carrier distribution, ionized donor states and band bending near the interface. In Chapter 3, only the results of BT and BST were presented. The BST70 experimental results

were not satisfactory compared to BT and BST50. Hence, we weren't able to correlate a scientific explanation between computational and experimental studies.

The penetration of conduction band in Fermi level indicates the electron accumulation state in the interface and hence the polarization state can be determined. Here we found a good agreement between the experimental study and the proposed computational model. We should note that, this model is an ideal thermodynamic model which was only proposed to clarify some facts about ferroelectric polarization state and corresponding mechanism proposed in this thesis. In addition, this computational study confirmed the experimental study results and explained the band bending, carrier accumulation and depletion which only semi qualitatively explained the proposed mechanism. The misfit in our computational study was 1% which is a well-accepted value for such systems which in real life might be higher values.

Based on the regular I-V results, the resistive switching magnitudes in BT and BST50 (Pt electrode, configuration 1) were very close to each other in which the magnitude in BST50 was one order of magnitude higher. The tricky point to interpret the computational data was that the applied voltage abruptly changed from +1V to -1V, and the assumption was that the system was in equilibrium in either applied biases. In this model,  $\pm 1V$  were the only boundary conditions to change the polarization and consequently change the electron distribution and ionized donor states near the interface.

By means of this, we correlated the computational results to the mechanism we proposed for the resistive switching which was the effect of the polarization change on the barrier height (BH) and consequently charge flow in the system. In this work, we focused on the experimental evidence for resistive switching in the light of thermodynamic theory of these systems and discussed the effect of Sr content on current-voltage characteristics of our samples.

## REFERENCES

- [1] K. Sreenivas, A. Mansingh, and M. Sayer, "Structural and electrical properties of rf-sputtered amorphous barium titanate thin films," *J. Appl. Phys.*, vol. 62, no. 11, p. 4475, 1987.
- [2] A. Kozyrev, A. Ivanov, T. Samoiloova, O. Soldatenkov, K. Astafiev, and L. C. Sengupta, "Nonlinear response and power handling capability of ferroelectric Ba<sub>x</sub>Sr<sub>1-x</sub>TiO<sub>3</sub> thin capacitors and tunable microwave devices," *J. Appl. Phys.*, 2000.
- [3] S. J. Fiedziuszko, I. C. Hunter, T. Itoh, Y. Kobayashi, T. Nishikawa, S. N. Stitzer, and K. Wakino, "Dielectric materials, devices, and circuits," *IEEE Trans. Microw. Theory Tech.*, vol. 50, no. 3, pp. 706–720, Mar. 2002.
- [4] W. Chang, S. W. Kirchoefer, J. M. Pond, J. S. Horwitz, and L. Sengupta, "Strain-relieved Ba<sub>0.6</sub>Sr<sub>0.4</sub>TiO<sub>3</sub> thin films for tunable microwave applications," *J. Appl. Phys.*, vol. 92, no. 3, p. 1528, 2002.
- [5] T. Ayguavives, A. Tombak, J.-P. Maria, G. T. Stauff, C. Ragaglia, J. Roeder, A. Mortazawi, and A. I. Kingon, "Physical properties of (Ba,Sr)TiO<sub>3</sub> thin films used for integrated capacitors in microwave applications," in *ISAF 2000. Proceedings of the 2000 12th IEEE International Symposium on Applications of Ferroelectrics (IEEE Cat. No.00CH37076)*, vol. 1, pp. 365–368.
- [6] B. H. Park and Q. Jia, "Enhanced Dielectric Properties of (Ba,Sr)TiO<sub>3</sub> Thin Films Applicable to Tunable Microwave Devices," *Jpn. J. Appl. Phys.*, vol. 41, no. Part 1, No. 11B, pp. 7222–7225, Nov. 2002.
- [7] M. Jain, S. B. Majumder, R. S. Katiyar, A. S. Bhalla, D. C. Agrawal, F. W. Van Keuls, F. A. Miranda, R. R. Romanofsky, and C. H. Mueller, "Improved Dielectric Properties of Heterostructured Ba<sub>0.5</sub>Sr<sub>0.5</sub>TiO<sub>3</sub> Thin Film Composites for Microwave Dielectric Devices," *MRS Proc.*, vol. 748, no. 1, p. U17.4, Jan. 2002.
- [8] H. Hu and S. B. Krupanidhi, "Enhanced electrical properties of ferroelectric Pb(Zr<sub>0.5</sub>, Ti<sub>0.5</sub>)O<sub>3</sub> thin films grown with low-energy oxygen ion assistance," *J. Appl. Phys.*, vol. 74, no. 5, p. 3373, 1993.
- [9] R. E. Jones, P. D. Maniar, J. O. Olowolafe, A. C. Campbell, and C. J. Mogab, "Electrical characteristics of paraelectric lead lanthanum zirconium titanate thin films for dynamic random access memory applications," *Appl. Phys. Lett.*, vol. 60, no. 8, p. 1022, 1992.
- [10] H. Katagiri, A. K. Lefor, T. Kubota, and K. Mizokami, "Barium appendicitis: A single institution review in Japan," *World J. Gastrointest. Surg.*, vol. 8, no. 9, p. 651, 2016.
- [11] H.-M. Li, L.-R. Yeh, Y.-K. Huang, C.-L. Lin, and C.-H. Kao, "The Association Between Barium Examination and Subsequent Appendicitis: A Nationwide Population-Based Study," *Am. J. Med.*, vol. 130, no. 1, p. 54–60.e5, Jan. 2017.
- [12] K. Shrivastava, P. Maji, and K. Dewangan, "Onsite-detection of barium and nickel from river, pond and tap water samples using gold nanoparticles as a chemical sensor," *Spectrochim. Acta Part A Mol. Biomol. Spectrosc.*, vol. 173, pp. 630–636, Feb. 2017.
- [13] M. W. Cole, E. Ngo, C. Hubbard, S. G. Hirsch, M. Ivill, W. L. Sarney, J. Zhang, and S. P. Alpay, "Enhanced dielectric properties from barium strontium titanate films with strontium titanate buffer layers," *J. Appl. Phys.*, vol. 114, no. 16, p. 164107, 2013.
- [14] X. Sun, Y. Yang, Q. Zhang, X. Zhou, Z. Hu, and C. Huang, "Enhanced dielectric and tunable properties of barium strontium titanate thin films through introducing Nd<sub>0.5</sub>(Zn<sub>1/2</sub>Ti<sub>1/2</sub>)O<sub>3</sub> and adjusting Ba/Sr," *J. Mater. Sci.*, vol. 49, no. 3, pp. 1058–1065, Feb. 2014.
- [15] M. Stengel, D. Vanderbilt, and N. A. Spaldin, "Enhancement of ferroelectricity at metal–oxide interfaces," *Nat. Mater.*, vol. 8, no. 5, pp. 392–397, May 2009.
- [16] L. D. Filip, L. Pintilie, W.-S. Tam, and C.-W. Kok, "Leakage current for thin film metal-ferroelectric-metal devices," in *2016 5th International Symposium on Next-Generation Electronics (ISNE)*, 2016, pp. 1–2.

- [17] A. Loidl, S. Krohns, J. Hemberger, and P. Lunkenheimer, "Bananas go paraelectric," *J. Phys. Condens. Matter*, vol. 20, no. 19, p. 191001, May 2008.
- [18] K. Uchino, *Ferroelectric devices*. CRC Press, 2010.
- [19] K. Aizu, "Possible Species of Ferroelectrics," *Phys. Rev.*, vol. 146, no. 2, pp. 423–429, Jun. 1966.
- [20] M. Stengel and N. A. Spaldin, "Origin of the dielectric dead layer in nanoscale capacitors," *Nature*, vol. 443, no. 7112, pp. 679–682, Oct. 2006.
- [21] J. Junquera and P. Ghosez, "Critical thickness for ferroelectricity in perovskite ultrathin films," *Nature*, vol. 422, no. 6931, pp. 506–509, Apr. 2003.
- [22] A. M. Bratkovsky and A. P. Levanyuk, "Bratkovsky and Levanyuk Reply:," *Phys. Rev. Lett.*, vol. 87, no. 17, p. 179703, Oct. 2001.
- [23] M. Stengel, C. J. Fennie, and P. Ghosez, "Electrical properties of improper ferroelectrics from first principles," *Phys. Rev. B*, vol. 86, no. 9, p. 94112, Sep. 2012.
- [24] N. Sai, C. J. Fennie, and A. A. Demkov, "Absence of Critical Thickness in an Ultrathin Improper Ferroelectric Film," *Phys. Rev. Lett.*, vol. 102, no. 10, p. 107601, Mar. 2009.
- [25] V. N. Shut, S. R. Syrtsov, and V. L. Trublovsky, "Polarization characteristics of graded thick  $\text{Ba}_{1-x}\text{Sr}_x\text{TiO}_3$  films," *Phys. Solid State*, vol. 53, no. 9, p. 1859, 2011.
- [26] R. E. Cohen, "Origin of ferroelectricity in perovskite oxides," *Nature*, vol. 358, no. 6382, pp. 136–138, Jul. 1992.
- [27] R. Blinc, *Soft modes in ferroelectrics and antiferroelectrics*. North-Holland, 1974.
- [28] N. Sai, B. Meyer, and D. Vanderbilt, "Compositional Inversion Symmetry Breaking in Ferroelectric Perovskites," *Phys. Rev. Lett.*, vol. 84, no. 24, pp. 5636–5639, Jun. 2000.
- [29] N. W. Schubring, J. V. Mantese, A. L. Micheli, A. B. Catalan, and R. J. Lopez, "Charge pumping and pseudopyroelectric effect in active ferroelectric relaxor-type films," *Phys. Rev. Lett.*, vol. 68, no. 11, pp. 1778–1781, Mar. 1992.
- [30] A. L. Roytburd, S. P. Alpay, V. Nagarajan, C. S. Ganpule, S. Aggarwal, E. D. Williams, and R. Ramesh, "Measurement of Internal Stresses via the Polarization in Epitaxial Ferroelectric Films," *Phys. Rev. Lett.*, vol. 85, no. 1, pp. 190–193, Jul. 2000.
- [31] T. Hu, H. Jantunen, A. Uusimäki, and S. Leppävuori, "BST powder with sol-gel process in tape casting and firing," *J. Eur. Ceram. Soc.*, vol. 24, no. 6, pp. 1111–1116, 2004.
- [32] C. Liu and P. Liu, "Microstructure and dielectric properties of BST ceramics derived from high-energy ball-milling," *J. Alloys Compd.*, vol. 584, pp. 114–118, 2014.
- [33] A. Kurniawan, D. Yosman, A. Arif, J. Juansah, and Irzaman, "Development and Application of  $\text{Ba}_{0.5}\text{Sr}_{0.5}\text{TiO}_3$  (BST) Thin Film as Temperature Sensor for Satellite Technology," *Procedia Environ. Sci.*, vol. 24, pp. 335–339, 2015.
- [34] F. Landolt–Bornstein, "Related Substances," *New Ser.*, vol. 16, 1981.
- [35] J. Guyonnet, "Ferroelectric Domain Walls," *Springer Thesis*, p. Chap. 2, 2014.
- [36] D. Damjanovic, "Ferroelectric, dielectric and piezoelectric properties of ferroelectric thin films and ceramics," *Reports Prog. Phys.*, vol. 61, no. 9, pp. 1267–1324, Sep. 1998.
- [37] P. M. Weaver, M. G. Cain, and M. Stewart, "Temperature dependence of high field electromechanical coupling in ferroelectric ceramics," *J. Phys. D. Appl. Phys.*, vol. 43, no. 16, p. 165404, Apr. 2010.

- [38] M. Stewart, M. G. Cain, and P. Weaver, "Electrical Measurement of Ferroelectric Properties," 2014, pp. 1–14.
- [39] I. B. Misirlioglu and S. P. Alpay, "Compositionally graded ferroelectrics as wide band gap semiconductors: Electrical domain structures and the origin of low dielectric loss," *Acta Mater.*, vol. 122, pp. 266–276, 2017.
- [40] I. B. Misirlioglu and M. Yildiz, "Dielectric response of fully and partially depleted ferroelectric thin films and inversion of the thickness effect," *J. Phys. D. Appl. Phys.*, vol. 46, no. 12, p. 125301, Mar. 2013.
- [41] I. B. Misirlioglu and M. Yildiz, "Very large dielectric response from ferroelectric nanocapacitor films due to collective surface and strain relaxation effects," *J. Appl. Phys.*, vol. 114, no. 19, p. 194101, Nov. 2013.
- [42] O. G. Vendik, S. P. Zubko, and N. Y. Medvedeva, "'Dead layer' characteristics based on a correlation of the ferroelectric polarization under relevant boundary conditions in a parallel plate capacitor," *J. Appl. Phys.*, vol. 105, no. 5, p. 53515, Mar. 2009.
- [43] Y. L. Li, S. Y. Hu, Z. K. Liu, and L. Q. Chen, "Effect of electrical boundary conditions on ferroelectric domain structures in thin films," *Appl. Phys. Lett.*, vol. 81, no. 3, pp. 427–429, Jul. 2002.
- [44] A. P. Levanyuk and I. B. Misirlioglu, "Phase transitions in ferroelectric-paraelectric superlattices," *J. Appl. Phys.*, vol. 110, no. 11, p. 114109, Dec. 2011.
- [45] H. (Hans) Lüth, *Solid Surfaces, Interfaces and Thin Films*. Springer Berlin Heidelberg, 2001.
- [46] L. Pintilie, "Charge Transport in Ferroelectric Thin Films," in *Ferroelectrics - Physical Effects*, InTech, 2011.
- [47] L. Pintilie, I. Boerasu, M. J. M. Gomes, T. Zhao, R. Ramesh, and M. Alexe, "Metal-ferroelectric-metal structures with Schottky contacts. II. Analysis of the experimental current-voltage and capacitance-voltage characteristics of Pb(Zr,Ti)O<sub>3</sub> thin films," *J. Appl. Phys.*, vol. 98, no. 12, p. 124104, Dec. 2005.
- [48] V. N. Shut, "Ferroelectrics with composition gradient: On the nature of hysteresis loop shift," *Phys. Solid State*, vol. 55, no. 7, pp. 1438–1441, Jul. 2013.
- [49] M. B. Okatan, A. L. Roytburd, V. Nagarajan, and S. P. Alpay, "Electrical domain morphologies in compositionally graded ferroelectric films," *J. Phys. Condens. Matter*, vol. 24, no. 2, p. 24215, Jan. 2012.
- [50] J. V. Mantese, N. W. Schubring, and A. L. Micheli, "Polarization-graded ferroelectrics: Transpacitor push-pull amplifier," *Appl. Phys. Lett.*, vol. 80, no. 8, pp. 1430–1431, Feb. 2002.
- [51] T. Qi, M. T. Curnan, S. Kim, J. W. Bennett, I. Grinberg, and A. M. Rappe, "First-principles study of band gap engineering via oxygen vacancy doping in perovskite  $A B B' O_3$  solid solutions," *Phys. Rev. B*, vol. 84, no. 24, p. 245206, Dec. 2011.
- [52] T. Qi, I. Grinberg, and A. M. Rappe, "Band-gap engineering via local environment in complex oxides," *Phys. Rev. B*, vol. 83, no. 22, p. 224108, Jun. 2011.
- [53] M. J. Haun, E. Furman, H. A. McKinstry, and L. E. Cross, "Thermodynamic theory of the lead zirconate-titanate solid solution system, part II: Tricritical behavior," *Ferroelectrics*, vol. 99, no. 1, pp. 27–44, Nov. 1989.
- [54] N. A. Pertsev, A. G. Zembilgotov, and A. K. Tagantsev, "Effect of Mechanical Boundary Conditions on Phase Diagrams of Epitaxial Ferroelectric Thin Films," *Phys. Rev. Lett.*, vol. 80, no. 9, pp. 1988–1991, Mar. 1998.
- [55] C. Basceri, S. K. Streiffner, A. I. Kingon, and R. Waser, "The dielectric response as a function of temperature and film thickness of fiber-textured (Ba,Sr)TiO<sub>3</sub> thin films grown by chemical vapor deposition," <http://dx.doi.org/10.1063/1.366062>, 1998.
- [56] C. H. Lin, P. A. Friddle, C. H. Ma, A. Daga, and H. Chen, "Effects of thickness on the electrical properties of metalorganic chemical

- vapor deposited Pb(Zr, Ti)O<sub>3</sub> (25–100 nm) thin films on LaNiO<sub>3</sub> buffered Si,” *J. Appl. Phys.*, vol. 90, no. 3, pp. 1509–1515, Aug. 2001.
- [57] D. Bolten, U. Böttger, and R. Waser, “Reversible and irreversible polarization processes in ferroelectric ceramics and thin films,” *J. Appl. Phys.*, vol. 93, no. 3, pp. 1735–1742, Feb. 2003.
- [58] J. F. M. Cillessen, M. W. J. Prins, and R. M. Wolf, “Thickness dependence of the switching voltage in all-oxide ferroelectric thin-film capacitors prepared by pulsed laser deposition,” <http://dx.doi.org/10.1063/1.363961>, 1998.
- [59] L. Pintilie, M. Lisca, and M. Alexe, “Polarization reversal and capacitance-voltage characteristic of epitaxial Pb(Zr,Ti)O<sub>3</sub> layers,” *Appl. Phys. Lett.*, vol. 86, no. 19, p. 192902, May 2005.
- [60] S.-W. Chen and J.-M. Wu, “Unipolar resistive switching behavior of BiFeO<sub>3</sub> thin films prepared by chemical solution deposition,” *Thin Solid Films*, vol. 519, no. 1, pp. 499–504, 2010.
- [61] R. Oligschlaeger, R. Waser, R. Meyer, S. Karthäuser, and R. Dittmann, “Resistive switching and data reliability of epitaxial (Ba,Sr)TiO<sub>3</sub> thin films,” *Appl. Phys. Lett.*, vol. 88, no. 4, p. 42901, Jan. 2006.
- [62] C. J. Kim and I.-W. Chen, “Effect of top electrode on resistance switching of (Pr, Ca)MnO<sub>3</sub> thin films,” *Thin Solid Films*, vol. 515, no. 4, pp. 2726–2729, 2006.
- [63] I. H. Inoue, S. Yasuda, H. Akinaga, and H. Takagi, “Nonpolar resistance switching of metal/binary-transition-metal oxides/metal sandwiches: Homogeneous/inhomogeneous transition of current distribution,” *Phys. Rev. B*, vol. 77, no. 3, p. 35105, Jan. 2008.
- [64] E. Mikheev, B. D. Hoskins, D. B. Strukov, and S. Stemmer, “Resistive switching and its suppression in Pt/Nb:SrTiO<sub>3</sub> junctions,” *Nat. Commun.*, vol. 5, pp. 28–36, Jun. 2014.
- [65] H. Kohlstedt, N. A. Pertsev, J. R. Contreras, and R. Waser, “Theoretical current-voltage characteristics of ferroelectric tunnel junctions,” Mar. 2005.
- [66] T. Fujii, M. Kawasaki, A. Sawa, H. Akoh, Y. Kawazoe, and Y. Tokura, “Hysteretic current–voltage characteristics and resistance switching at an epitaxial oxide Schottky junction SrRuO<sub>3</sub>/SrTi<sub>0.99</sub>Nb<sub>0.01</sub>O<sub>3</sub>,” *Appl. Phys. Lett.*, vol. 86, no. 1, p. 12107, Jan. 2005.
- [67] W. Shen, R. Dittmann, U. Breuer, and R. Waser, “Improved endurance behavior of resistive switching in (Ba,Sr)TiO<sub>3</sub> thin films with W top electrode,” *Appl. Phys. Lett.*, vol. 93, no. 22, p. 222102, Dec. 2008.
- [68] A. Sawa, “Resistive switching in transition metal oxides,” *Mater. Today*, vol. 11, no. 6, pp. 28–36, 2008.
- [69] V. Garcia and M. Bibes, “Ferroelectric tunnel junctions for information storage and processing,” *Nat. Commun.*, vol. 5, Jul. 2014.
- [70] M. Stengel, D. Vanderbilt, and N. A. Spaldin, “Enhancement of ferroelectricity at metal–oxide interfaces,” *Nat. Mater.*, vol. 8, no. 5, pp. 392–397, May 2009.
- [71] H. Kohlstedt, N. A. Pertsev, J. Rodríguez Contreras, and R. Waser, “Theoretical current-voltage characteristics of ferroelectric tunnel junctions,” *Phys. Rev. B*, vol. 72, no. 12, p. 125341, Sep. 2005.
- [72] K. Lefki and G. J. M. Dormans, “Measurement of piezoelectric coefficients of ferroelectric thin films,” *J. Appl. Phys.*, vol. 76, no. 3, pp. 1764–1767, Aug. 1994.
- [73] J. P. Velez, C.-G. Duan, J. D. Burton, A. Smogunov, M. K. Niranjan, E. Tosatti, S. S. Jaswal, and E. Y. Tsymbal, “Magnetic Tunnel Junctions with Ferroelectric Barriers: Prediction of Four Resistance States from First Principles,” *Nano Lett.*, vol. 9, no. 1, pp. 427–432, Jan. 2009.

- [74] V. Garcia and M. Bibes, "Ferroelectric tunnel junctions for information storage and processing," *Nat. Commun.*, vol. 5, pp. 954–959, Jul. 2014.
- [75] J. J. Yang, J. P. Strachan, F. Miao, M.-X. Zhang, M. D. Pickett, W. Yi, D. A. A. Ohlberg, G. Medeiros-Ribeiro, and R. S. Williams, "Metal/TiO<sub>2</sub> interfaces for memristive switches," *Appl. Phys. A*, vol. 102, no. 4, pp. 785–789, Mar. 2011.
- [76] A. M. Cowley and S. M. Sze, "Surface States and Barrier Height of Metal-Semiconductor Systems," *J. Appl. Phys.*, vol. 36, no. 10, pp. 3212–3220, Oct. 1965.
- [77] P. W. M. Blom, R. M. Wolf, J. F. M. Cillessen, and M. P. C. M. Krijn, "Ferroelectric Schottky Diode," *Phys. Rev. Lett.*, vol. 73, no. 15, pp. 2107–2110, Oct. 1994.
- [78] R. Meyer and H. Kohlstedt, "1-D simulation of a novel nonvolatile resistive random access memory device," *IEEE Trans. Ultrason. Ferroelectr. Freq. Control*, vol. 53, no. 12, pp. 2340–2348, Dec. 2006.
- [79] H. Kohlstedt, N. A. Pertsev, J. Rodríguez Contreras, and R. Waser, "Theoretical current-voltage characteristics of ferroelectric tunnel junctions," *Phys. Rev. B*, vol. 72, no. 12, p. 125341, Sep. 2005.
- [80] H. Kohlstedt, A. Petraru, K. Szot, A. Rüdiger, P. Meuffels, H. Haselier, R. Waser, and V. Nagarajan, "Method to distinguish ferroelectric from nonferroelectric origin in case of resistive switching in ferroelectric capacitors," *Appl. Phys. Lett.*, vol. 92, no. 6, p. 62907, Feb. 2008.
- [81] P. Maksymovych, S. Jesse, P. Yu, R. Ramesh, A. P. Baddorf, and S. V. Kalinin, "Polarization Control of Electron Tunneling into Ferroelectric Surfaces," *Science (80-. )*, vol. 324, no. 5933, 2009.
- [82] E. Mikheev, B. D. Hoskins, D. B. Strukov, and S. Stemmer, "Resistive switching and its suppression in Pt/Nb:SrTiO<sub>3</sub> junctions," *Nat. Commun.*, vol. 5, p. 3990, Jun. 2014.
- [83] Z. Wen, C. Li, D. Wu, A. Li, and N. Ming, "Ferroelectric-field-effect-enhanced electroresistance in metal/ferroelectric/semiconductor tunnel junctions," *Nat. Mater.*, vol. 12, no. 7, pp. 617–621, May 2013.
- [84] M. C. Gust, L. A. Momoda, N. D. Evans, and M. L. Mecartney, "Crystallization of Sol-Gel-Derived Barium Strontium Titanate Thin Films," *J. Am. Ceram. Soc.*, vol. 84, no. 5, pp. 1087–1092, May 2001.
- [85] J.-G. Cheng, X.-J. Meng, J. Tang, S.-L. Guo, and J.-H. Chu, "Fabrication and electrical properties of sol-gel-derived Ba<sub>0.8</sub>Sr<sub>0.2</sub>TiO<sub>3</sub> ferroelectric films from a 0.05-M spin-on solution," *Appl. Phys. A Mater. Sci. Process.*, vol. 70, no. 4, pp. 411–414, Apr. 2000.
- [86] D. Tahan, A. Safari, and L. C. Klein, "Sol-gel preparation of barium strontium titanate thin films," in *Proceedings of 1994 IEEE International Symposium on Applications of Ferroelectrics*, pp. 427–430.
- [87] E. Dien, R. Verweur, M. Lejeune, and A. Smith, "Preparation and properties of Ba<sub>1-x</sub>Sr<sub>x</sub>TiO<sub>3</sub> thin films deposited by the sol-gel technique," *Le J. Phys. IV*, vol. 8, no. PR9, p. Pr9-73-Pr9-77, Dec. 1998.
- [88] F. M. Pontes, E. R. Leite, D. S. L. Pontes, E. Longo, E. M. S. Santos, S. Mergulhão, P. S. Pizani, F. Lanciotti, T. M. Boschi, and J. A. Varela, "Ferroelectric and optical properties of Ferroelectric and optical properties of Ba<sub>0.8</sub>Sr<sub>0.2</sub>TiO<sub>3</sub>Ba<sub>0.8</sub>Sr<sub>0.2</sub>TiO<sub>3</sub> thin film Ba<sub>0.8</sub>Sr<sub>0.2</sub>TiO<sub>3</sub> thin film," *J. Appl. Phys.*, vol. 91, no. 9, p. 5972, 2002.
- [89] H.-Y. Tian, W.-G. Luo, X.-H. Pu, and A.-L. Ding, "Synthesis and microstructure of the acetate-based Sr-doped barium titanate thin films using a modified sol-gel technique," *J. Mater. Sci. Lett.*, vol. 19, no. 14, pp. 1211–1213, 2000.
- [90] G. Yi and M. SAYER, "Sol-gel processing of complex oxide films," *Am. Ceram. Soc. Bull.*, vol. 70, no. 7, pp. 1173–1179.
- [91] L. M. Hrib, A. G. Boni, C. Chirila, I. Pasuk, I. Pintilie, and L. Pintilie, "Electrode interface control of the Schottky diode-like

- behavior in epitaxial  $\text{Pb}(\text{Zr}_{0.2}\text{Ti}_{0.8})\text{O}_3$  thin films: A critical analysis," *J. Appl. Phys.*, vol. 113, no. 21, p. 214108, Jun. 2013.
- [92] N. Ortega, A. Kumar, O. Resto, O. A. Maslova, Y. I. Yuzyuk, J. F. Scott, and R. S. Katiyar, "Compositional engineering of  $\text{BaTiO}_3$  / $(\text{Ba,Sr})\text{TiO}_3$  ferroelectric superlattices," *J. Appl. Phys.*, vol. 114, no. 10, p. 104102, Sep. 2013.
- [93] P. M. Raj, S. Xiang, M. Kumar, I. R. Abothu, J.-H. Hwang, Y. Liu, H. Yamamoto, and R. Tummala, "Leakage current suppression in solution-deposited barium titanate films on copper foils," *J. Mater. Sci. Mater. Electron.*, vol. 23, no. 4, pp. 901–908, Apr. 2012.
- [94] L. Pintilie, V. Stancu, L. Trupina, and I. Pintilie, "Ferroelectric Schottky diode behavior from a  $\text{SrRuO}_3$ - $\text{Pb}(\text{Zr}_{0.2}\text{Ti}_{0.8})\text{O}_3$ - $\text{Ta}$  structure," *Phys. Rev. B*, vol. 82, no. 8, p. 85319, Aug. 2010.
- [95] A. Chanthbouala, A. Crassous, V. Garcia, K. Bouzehouane, S. Fusil, X. Moya, J. Allibe, B. Dlubak, J. Grollier, S. Xavier, C. Deranlot, A. Moshar, R. Proksch, N. D. Mathur, M. Bibes, and A. Barthélémy, "Solid-state memories based on ferroelectric tunnel junctions," *Nat. Nanotechnol.*, vol. 7, no. 2, pp. 101–104, Dec. 2011.
- [96] D. J. Kim, H. Lu, S. Ryu, C.-W. Bark, C.-B. Eom, E. Y. Tsymbal, and A. Gruverman, "Ferroelectric Tunnel Memristor," *Nano Lett.*, vol. 12, no. 11, pp. 5697–5702, Nov. 2012.
- [97] Z. Hu, Q. Li, M. Li, Q. Wang, Y. Zhu, X. Liu, X. Zhao, Y. Liu, and S. Dong, "Ferroelectric memristor based on  $\text{Pt}/\text{BiFeO}_3$  / $\text{Nb}$ -doped  $\text{SrTiO}_3$  heterostructure," *Appl. Phys. Lett.*, vol. 102, no. 10, p. 102901, Mar. 2013.
- [98] D. Lee, S. H. Baek, T. H. Kim, J.-G. Yoon, C. M. Folkman, C. B. Eom, and T. W. Noh, "Polarity control of carrier injection at ferroelectric/metal interfaces for electrically switchable diode and photovoltaic effects," *Phys. Rev. B*, vol. 84, no. 12, p. 125305, Sep. 2011.
- [99] H. Kohlstedt, A. Petraru, K. Szot, A. Rüdiger, P. Meuffels, H. Haselier, R. Waser, and V. Nagarajan, "Method to distinguish ferroelectric from nonferroelectric origin in case of resistive switching in ferroelectric capacitors," *Appl. Phys. Lett.*, vol. 92, no. 6, p. 62907, Feb. 2008.
- [100] R. MEYER, J. R. CONTRERAS, A. PETRARU, and H. KOHLSTEDT, "On a Novel Ferro Resistive Random Access Memory (FRRAM): Basic Model and First Experiments," *Integr. Ferroelectr.*, vol. 64, no. 1, pp. 77–88, Jan. 2004.
- [101] C. Wang, K. Jin, Z. Xu, L. Wang, C. Ge, H. Lu, H. Guo, M. He, and G. Yang, "Switchable diode effect and ferroelectric resistive switching in epitaxial  $\text{BiFeO}_3$  thin films," *Appl. Phys. Lett.*, vol. 98, no. 19, p. 192901, May 2011.
- [102] A. Q. Jiang, C. Wang, K. J. Jin, X. B. Liu, J. F. Scott, C. S. Hwang, T. A. Tang, H. Bin Lu, and G. Z. Yang, "A Resistive Memory in Semiconducting  $\text{BiFeO}_3$  Thin-Film Capacitors," *Adv. Mater.*, vol. 23, no. 10, pp. 1277–1281, Mar. 2011.
- [103] X. Chen, C. H. Jia, Y. H. Chen, G. Yang, and W. F. Zhang, "Ferroelectric memristive effect in  $\text{BaTiO}_3$  epitaxial thin films," *J. Phys. D: Appl. Phys.*, vol. 47, no. 36, p. 365102, Sep. 2014.
- [104] S. Sze and K. Ng, *Physics of semiconductor devices*. 2006.
- [105] S. Tinte, M. G. Stachiotti, S. R. Phillpot, M. Sepiarsky, D. Wolf, and R. L. Migoni, "Ferroelectric properties of  $\text{Ba}_x\text{Sr}_{1-x}\text{TiO}_3$  solid solutions obtained by molecular dynamics simulation," *J. Phys. Condens. Matter*, vol. 16, no. 20, pp. 3495–3506, May 2004.